

HB 7807

2133/96

DISSERTATION

The Silicon Ministrip Detector of the  
DELPHI Very Forward Tracker



ausgeführt zum Zweck der Erlangung des akademischen Grades  
eines Doktors der technischen Wissenschaften

eingereicht an der Technischen Universität Wien  
Technisch Naturwissenschaftliche Fakultät  
von

Dipl. Ing. Heinz Pernegger  
Giesshüblerstr. 122  
A-2344 Maria Enzersdorf  
Matr. Nr. 8525432  
geb. am 7. Oktober 1966 in Wels

*Heinz Pernegger*

unter Anleitung von Univ. Prof. Dr. M. Regler

Wien, im Februar 1996

Die Drucklegung unter der Bezeichnung „Dissertation“ ist nur mit Zustimmung der Fakultät gestattet!

Diese Dissertation haben begutachtet:

*W. G. ...*

# Preface

The subject of this work is the design, test and construction of a new silicon tracking detector for the extreme forward region of the DELPHI experiment at LEP. I joined the Very Forward Tracker (VFT) Ministrip group in 1993, at a time when the upgrade of the DELPHI tracking system was proposed. My first task was to participate in the design of the ministrip detector for the VFT. This included the optimisation of the detector layout in simulations and the study of prototype detectors in the testbeam. In 1994 I became responsible for the tests and assembly of the VFT ministrip detector at CERN. The main focus of my work was the study of the performance of a large variety of detectors in beam tests. This included the preparation of the test setup, the tests of different detectors and the analysis of the measurements. With these measurements it is possible to compare the advantages and disadvantages of various new layouts for large pitch silicon strip detectors. In particular the signal response and spatial resolution of the VFT ministrip detector was precisely measured and modelled. The results of this study form the central part of my thesis. During 1995, prior to the assembly of the VFT detector, my main task was the quality monitoring of the final VFT ministrip detectors in acceptance tests at CERN. The experience gained during these tests was subsequently used to optimise the control of the detector to assure reliable operation in DELPHI.

In the following I will give a brief overview of the contents of this thesis: In chapter 1 an overview of the DELPHI detector and its components, in particular the silicon tracking detector, is presented. Chapter 2 is dedicated to the design of the DELPHI Very Forward Tracker. The requirements for the VFT are given together with the considerations influencing the layout and capability of the detector. The chapter shows the complex environment in the extreme forward region of collider experiments. A new unconventional design with inclined detectors was necessary to optimise efficiency and acceptance area. The only way to cope with the tight space constraints in the forward region is to mount the readout electronics on top of the active detector surface. The advantages and technical problems of this solution are described.

Chapter 3 presents the results of testbeam studies carried out on different large pitch strip detectors. The signal response and spatial resolution of well known and newly developed detectors was precisely measured. This study allows the comparison of many different layouts concerning their track reconstruction capability and intrinsic problems like insufficient charge measurement. The study provides useful information for the VFT ministrip layout and demonstrates the influence of layout parameters. It also provides necessary information for the design of similar detectors to be used in the future LHC (Large Hadron Collider) experiments.

The tracking capability of the VFT ministrip detector is presented in chapter 4. As the tracks in DELPHI will be inclined with respect to the detector surface, dedicated measurements at different track angles were carried out with the VFT ministrip detector. The measured signal response and spatial resolution could be modelled in a simulation, which proves excellent agreement with measurement data. Chapter 4 is concluded by an evaluation of the effects influencing the spatial resolution.

In chapter 5 the production of the VFT ministrip detector is summarised. The chapter

presents test results from the acceptance test of the full VFT ministrip detector prior to the installation in DELPHI. Extensive tests with the final configuration helped us to optimise the operation parameters and insure reliable detector operation.

Throughout the last three years I have been given the possibility to report on my work for this thesis. The considerations and results of the detector design are summarised in Nucl.Phys.B(Proc.Supp.)44(1995)292-295, which I had the pleasure to present at the 4<sup>th</sup> Int. Conference on Advanced Technology and Particle Physics 1994. The predictions of the detector simulation for the final layout has been accomplished with testbeam measurements on VFT prototype detectors (NIM A349(1994)424-430, DELPHI internal note DELPHI 94-44 Track 78). I had also the pleasure to report the results of the testbeam analysis with different large pitch detectors to the CMS collaboration (CMS collaboration meeting, Feb. 1996). Write-ups of the results presented in chapter 3 and 4 are currently in preparation and will be submitted for publication.

I owe special thanks to Dr. M. Krammer, head of the semiconductor group of the Institute for High Energy Physics, for the motivating work in his group and the many hours of fruitful discussions. His attention, encouragement and knowledge was essential for this thesis. I would like to thank my thesis supervisor, Prof. M. Regler, for his constant support and interest over many years. His advise and guidance was important for the analysis presented in this thesis. I want to express my gratefulness to Prof. W. Majerotto, director of the Institute for High Energy Physics, for financial support during this work.

Furthermore I want to thank all my colleagues, in particular W. Adam, D. Rakoczy, N. Neufeld, V. Cindro, V. Rykalin and R. Turchetta. I also want to acknowledge the help of Prof. P. Weilhammer and Dr. W. Dulinski for their support during the testbeam measurements and the supply of many test detectors.

Finally I want to thank my beloved girl-friend Bruna for all her patience and encouragement throughout the years. I dedicate this thesis to Bruna.

February 1996

Heinz Pernegger

# Contents

<b>1</b>	<b>Introduction</b>	<b>5</b>
1.1	The DELPHI detector at LEP . . . . .	5
1.2	The new DELPHI Silicon Tracker . . . . .	8
<b>2</b>	<b>The Very Forward Tracker</b>	<b>13</b>
2.1	Physics motivation . . . . .	13
2.2	Layout of the VFT detector system . . . . .	14
2.3	Design of the Ministrip detector . . . . .	18
<b>3</b>	<b>Silicon strip detectors with large strip pitch</b>	<b>22</b>
3.1	Basic components of silicon strip detectors . . . . .	22
3.1.1	The p-n junction . . . . .	24
3.1.2	Layout of silicon strip detectors . . . . .	27
3.1.3	Readout electronics . . . . .	29
3.2	Charge division in large strip pitch detectors . . . . .	35
3.2.1	The role of intermediate strips . . . . .	35
3.2.2	Simulation of detector signals . . . . .	37
3.3	Treatment of raw data in the analysis program . . . . .	41
3.3.1	Definitions of terms . . . . .	41
3.3.2	Signal calculation . . . . .	43
3.4	Performance evaluation of different detector geometries . . . . .	47
3.4.1	Layout of evaluated detectors . . . . .	47
3.4.2	Testbeam setup . . . . .	49
3.4.3	Signal measurements with different detector geometries . . . . .	51
3.4.4	Enhanced interstrip capacitance to avoid charge loss . . . . .	58
3.4.5	Spatial resolution of different detectors . . . . .	60
3.4.6	Influence of signal to noise performance on the spatial resolution . . . . .	68
<b>4</b>	<b>Position reconstruction with the VFT detector at different track angles</b>	<b>74</b>
4.1	Detector signal and spatial resolution . . . . .	75
4.1.1	Signal measurements at different track angles . . . . .	75
4.1.2	Single strip signal correlation . . . . .	76
4.1.3	Position reconstruction at different track angles . . . . .	87
4.1.4	Spatial resolution at different track angles . . . . .	89
4.2	Contributions to the measured spatial resolution . . . . .	96
4.2.1	Spatial resolution as a function of the interstrip position . . . . .	97

4.2.2	Influence of signal loss . . . . .	99
4.2.3	Influence of $\delta$ -rays . . . . .	99
<b>5</b>	<b>Production and Test of the VFT ministrip detector</b>	<b>102</b>
5.1	Production of the VFT ministrip detector . . . . .	102
5.2	Test of silicon detector parameters . . . . .	106
5.2.1	Detector leakage current . . . . .	106
5.2.2	FOXFET dynamical resistance . . . . .	108
5.2.3	Backplane capacitance and depletion voltage . . . . .	110
5.2.4	Coupling capacitance and pinholes in the coupling oxide . . . . .	112
5.3	Final acceptance tests on the VFT ministrip modules . . . . .	112
5.3.1	Results of the signal calibration . . . . .	113
5.3.2	Results of the $^{90}\text{Sr}$ source test . . . . .	115
5.4	Test beam studies with VFT ministrip modules . . . . .	117
5.5	Stability test of VFT ministrip crowns . . . . .	120
<b>6</b>	<b>Summary and Prospects</b>	<b>123</b>

# Chapter 1

## Introduction

### 1.1 The DELPHI detector at LEP

The Standard Model (SM) of electroweak interactions has been tested at the Large-Electron-Positron collider (LEP) at CERN with unprecedented accuracy. Since the start-up of the accelerator in 1989 the four LEP experiments ALEPH, DELPHI, L3 and OPAL have registered over 15 million  $Z^0$  decays and measured the mass and width of the  $Z^0$  with a precision of  $10^{-4}$ .  $m_Z$  reached the prestigious status of being the third fundamental constant of the Standard Model, that, with the fine structure constant  $\alpha$  and the weak coupling constant  $G_\mu$ , constitute the basic input to the calculation of other Standard Model observables. A summary of recent electroweak measurements at LEP can be found in reference [1].

The main objective of the research program at LEP for the forthcoming years is to study  $e^+e^-$  collisions at centre of mass energies close to 200 GeV (LEP200). This physics domain has never been explored before in  $e^+e^-$  collisions. It will allow to search for the yet undiscovered SM Higgs boson up to a mass of 90 GeV/ $c^2$ , to precisely determine the mass of the  $W$  boson and to perform the first direct measurement of triple boson couplings. Furthermore, tests of other theories, among which the Minimal Supersymmetric Standard Model (MSSM) is very promising, will be possible.

To allow the study of  $e^+e^-$  collisions at centre of mass energies up to 200 GeV the existing LEP collider, known as LEP 1, has to be upgraded. It is well known that circular electron machines are limited in energy by the rapid growth of synchrotron radiation (SR) emission. The emitted SR power  $P$  per turn at given curvature radius  $R$  is proportional to the 4th power of the electron energy

$$P = \frac{4\pi E_0 r_e I}{3eR} \left( \frac{E}{E_0} \right)^4 \quad (1.1)$$

$E$  and  $E_0$  denote the particle energy and energy at rest,  $r_e$  the classical electron radius and  $I$  the electron current. While at LEP1 at a beam energy of 46 GeV the particles energy loss per turn is moderate 130 MeV, it will become 2.3 GeV at a beam energy of 95 GeV, which is 2.5% of the particle energy [2].

This energy loss has to be restored by radiofrequency cavities. In case of conventional there is an additional ohmic loss in the rf cavities. The ohmic power loss is proportional

# DELPHI

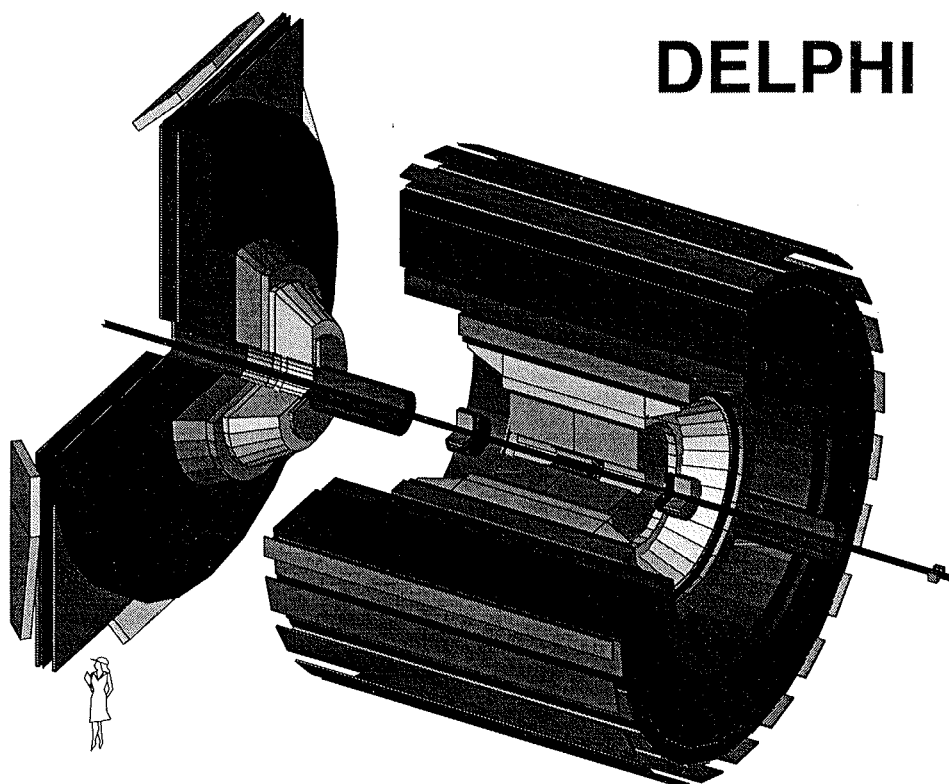


Figure 1.1: The DELPHI detector (only one of the two endcaps is shown)

to  $P^2/eZ_s$ , with  $Z_s$  being the shunt impedance of the accelerating structure, and therefore increases with  $\gamma^8$  [3]. Furthermore only about 10% of the consumed power in the cavities can be transferred to the particle beam. Already at LEP1 the ohmic power loss exceeds the synchrotron power loss.

The conventional copper cavities used for LEP1 will be totally insufficient for an envisaged centre of mass energy of 192 GeV. To cope with the enormous energy loss the former cavities will be replaced by 272 superconducting cavities until the end of 1996. By using superconducting cavities the ohmic power loss is highly suppressed. (Ultimately also superconducting accelerators are limited by cryogeny.) The first set of ??? cavities has already been installed and a centre of mass energy of 140 GeV was reached during November 1995. This is the highest energy ever reached by an electron collider. During this first run the four LEP experiments recorded an integrated luminosity of  $24 \text{ pb}^{-1}$ . The run was characterised by excellent stable beam conditions and low background, which proved the major success of the LEP upgrade.

The DELPHI detector (DEtector with Lepton, Photon and Hadron Identification) [4][5] is designed to provide particle identification, track and energy reconstruction in the full  $4\pi$  solid angle. Figure 1.1 shows a sketch of the DELPHI detector consisting of a barrel part and two endcaps, of which only one is illustrated in the figure. The detector is made up of five different parts: the tracking system next to the beam pipe and the particle identification detectors enclosed in the solenoid, the superconducting solenoid, the electromagnetical and hadron calorimeters, and the muon detectors. The detector surrounds the beam pipe which has an outer radius of 5.5 cm in the interaction region. The use of beryllium for the central part of the beam pipe limits multiple scattering of the particles close to the interaction region. For further reference the radius of a space point from the beam axis shall be denoted as  $R$ , its azimuthal and polar angle as  $\phi$  and  $\theta$ . The coordinate along the beam is called  $z$ . The horizontal coordinate  $x$  is perpendicular to  $z$  and points towards the centre of LEP, the vertical coordinate is perpendicular to the  $xz$  plane.

The superconducting solenoid provides a highly uniform magnetic field of 1.2T along the beam axis. This allows the reconstruction of the particle momentum with the tracking system using the track curvature.

The innermost tracking detector is the silicon microvertex detector (VD), consisting of three cylindrical layers of silicon strip detectors at radii of 6.3, 9.0, and 10.9 cm. The innermost and outermost cylinders are equipped with double-sided silicon detectors to allow two-dimensional track reconstruction with high precision. This detector is currently being upgraded to a new vertex detector which will be reviewed later. The new microvertex detector will be installed together with the DELPHI Very Forward Tracker (VFT), covering the forward region with silicon detectors, in May 1996. This detector part is among the most important ones for physics studies at LEP 200.

The Inner Detector (ID) surrounds the VD. The current inner detector has a central jet-chamber geometry that provides  $R\phi$  measurement of the tracks. The jet part is surrounded by straw tubes used in the trigger system. The ID covers a polar angular range  $15^\circ < \theta < 165^\circ$ .

The Time Projection Chamber (TPC) has the largest volume inside the tracking system of DELPHI. It is divided into two equal volumes by a high voltage plane at  $z = 0$  and two endcaps. The primary ionisation clusters produced by the traversing particle in the gas volume are drifted along the  $z$ -axis. The drift time of the ionisation clusters is measured together with their impact point on the endcap. The impact point is measured on 16 cathode pad rows. From the signal on the individual pads the cluster position is extracted. This results in a 3 dimensional measurement of the trajectories with up to 16 space points. The polar angle covered by the TPC is  $20^\circ < \theta < 160^\circ$ . The single point resolution is  $250\mu\text{m}$  in the  $R\phi$  plane at the longest drift distance and  $880\mu\text{m}$  in  $z$  direction. Transversal diffusion during the drift is suppressed by the magnetic field, being parallel to the direction of drift. The TPC provides energy loss information used for particle identification and a precise measurement of the particle momentum.

The tracking system in the forward region mainly relies on the TPC and on the Forward Chambers A and B (FCA, FCB). Both are circular-shaped drift chambers located at  $|z| = 160\text{cm}$  (FCA) and  $|z| = 275\text{cm}$  (FCB). They cover a polar angular range on each side of DELPHI of  $12^\circ < \theta < 32^\circ$  (FCA) and  $11^\circ < \theta < 36^\circ$  (FCB) with respect to the



beam axis. The FCA reconstructs track elements in the  $xy$  plane with a precision of  $290\mu\text{m}$  and a resolution for polar and azimuthal angle of  $8.5\text{ mrad}$  and  $24\text{ mrad}$  respectively. The corresponding values for the FCB are  $\sigma(x, y) = 150\mu\text{m}$ ,  $\sigma(\theta) = 3.5\text{mrad}$  and  $\sigma(\phi) = 4.0/\sin\theta\text{mrad}$ .

The DELPHI Very Forward Tracker will be a very important extension of the tracking system in the forward region close to the interaction point. It will dramatically improve the track reconstruction efficiency in a polar angular range of  $10^\circ < \theta < 25^\circ$  with respect to the beam axis on each side of the barrel micro vertex. As it is the subject of this work, it will be reviewed in detail in the following chapter.

The electron and photon identification is provided by the High Density Projection chamber (HPC) covering the barrel region, and by the Forward Electromagnetic Calorimeter (FEMC) and the Small angle Tile Calorimeter (STIC) in the endcap region. The STIC is used for electron and photon reconstruction in the extreme forward region. This calorimeter is used during LEP1 mainly to provide a luminosity measurement needed to normalise measured decay rates but at LEP200 will greatly contribute to the physics analysis by measuring electrons and photons in the extreme forward region between  $1.7^\circ < \theta < 10.6^\circ$  in each endcap.

The iron return yoke of the magnet is instrumented with limited streamer mode detectors forming the hadron calorimeter (HAC). Muon identification is achieved by combining the signals from minimum ionising particles in the calorimeters with the extrapolated hits in the Barrel, Forward and Surrounding Muon chambers (MUB, MUF, MUS).

A unique detector within all four LEP experiments is the DELPHI Ring Imaging Cherenkov detector (RICH). DELPHI is the only LEP experiment using this detector technique for particle identification. The RICH provides particle identification in the barrel (BRICH) and the forward (FRICH) region of DELPHI. Both BRICH and FRICH combine liquid and gaseous radiator media to identify particles over most of the considered momentum range.

A cylinder made of drift tubes around the RICH, the Outer Detector (OD), supports the tracking and trigger system in the barrel region.

The STIC, MUS and the new ID are, along with the upgraded microvertex detector, the result of an extensive upgrade program of the DELPHI detector [6] [7]. Tremendous effort has been put into the construction and implementation of these new detector parts to optimize the DELPHI detector for the challenging physics topics at LEP200.

## 1.2 The new DELPHI Silicon Tracker

The microvertex detector is the essential tool to reconstruct charged particle tracks with the highest possible precision close to the interaction point. This allows the reconstruction of secondary vertices coming from decays of “long” living particles like  $B$  mesons, where the lifetime is in the order of pico seconds. From the distance between the beam interaction point (the primary vertex) and their decay point the particle lifetime can be evaluated with suitable assumptions on the momentum spectrum of the individual decay channels [8]. A reconstructed  $Z \rightarrow b\bar{b}$  event as measured with the present vertex detector is displayed in figure 1.2. The top plots show the three layers of silicon detectors of the microvertex detector in  $xy$  and  $Rz$  view with the reconstructed tracks, the lower plots zoom to the

	closer module	inner layer module	outer layer module
total number of modules	24	20	24
number of silicon detectors/module	4 double-sided	4 double sided + 4 single-sided	$R\phi$ : 8, $Rz$ : 8
producer	Sintef	Hamamatsu	$R\phi$ : Hamamatsu $Rz$ : Sintef
type	n-type	n-type	n-type
readout pitch ( $\mu\text{m}$ )	$R\phi$ 50 $Rz$ 49.5,99,150	$R\phi$ 50 $Rz$ 42, 84	$R\phi$ 50 $Rz$ 44, 88, 176
intermediate strips	$R\phi$ 1 $Rz$ 0	$R\phi$ 1 $Rz$ 0	$R\phi$ 1 $Rz$ 0,1
biasing	polysilicon	single-sided: FOXFET double-sided: polysilicon	$R\phi$ FOXFET $Rz$ polysilicon
number of readout channels/module	1536	2560	2560
readout chip	MX6	MX6	Triplex

Table 1.1: Module layout of the DELPHI Si-Tracker barrel detector

interaction region showing the reconstructed vertices. The tagging and reconstruction of  $b$  quarks is of great interest for LEP 200. This specially applies to the search for new supersymmetric particles and the SM Higgs boson. As the coupling of the Higgs to fermions is proportional to the fermion mass, the Higgs, considered in the mass range covered by LEP200, preferably decays into  $b\bar{b}$ . To extend the b-tagging capability of the barrel microvertex detector, the cylindrical part of the silicon detector is prolonged to cover a polar angular range of  $25^\circ < \theta < 155^\circ$ .

Figure 1.3 shows a line drawing of the new DELPHI Silicon Tracker with the prolonged barrel part and the Very Forward Tracker mounted on both ends. The barrel detector consists of three layers at average radii of 6.5 cm (“closer layer”), 9.1 cm (“inner layer”) and 10.5 cm (“outer layer”). Each layer is formed by individual modules partially overlapping each other. Technical details of the layout of the modules can be found in table 1.1. The modules are made by chaining single-sided or double-sided detectors together to form a ladder of appropriate length. The closer and the outer layer modules have strips along the beam axis measuring  $R\phi$  coordinates of hits and strips perpendicular to the beam axis measuring the  $Rz$  coordinate.

The outer layer module consists of a ladder of single-sided detectors measuring the  $R\phi$  coordinate. The ladder is glued to another ladder of single-sided detectors measuring the  $Rz$  coordinate. To route the lines from the  $Rz$  detectors to the end of the modules and to the readout chips, the single-sided detectors have readout lines perpendicular to the strip implant on top of an insulation layer. This readout scheme is commonly referred to as a double metal layer readout scheme because the detector has one metallisation on the strip implant along the implant which is connected to a readout line, that runs perpendicular to the metal above the implant, via a small pinhole in the insulation layer [9].

The inner layer consists of four single-sided  $R\phi$  detectors in the centre of the modules

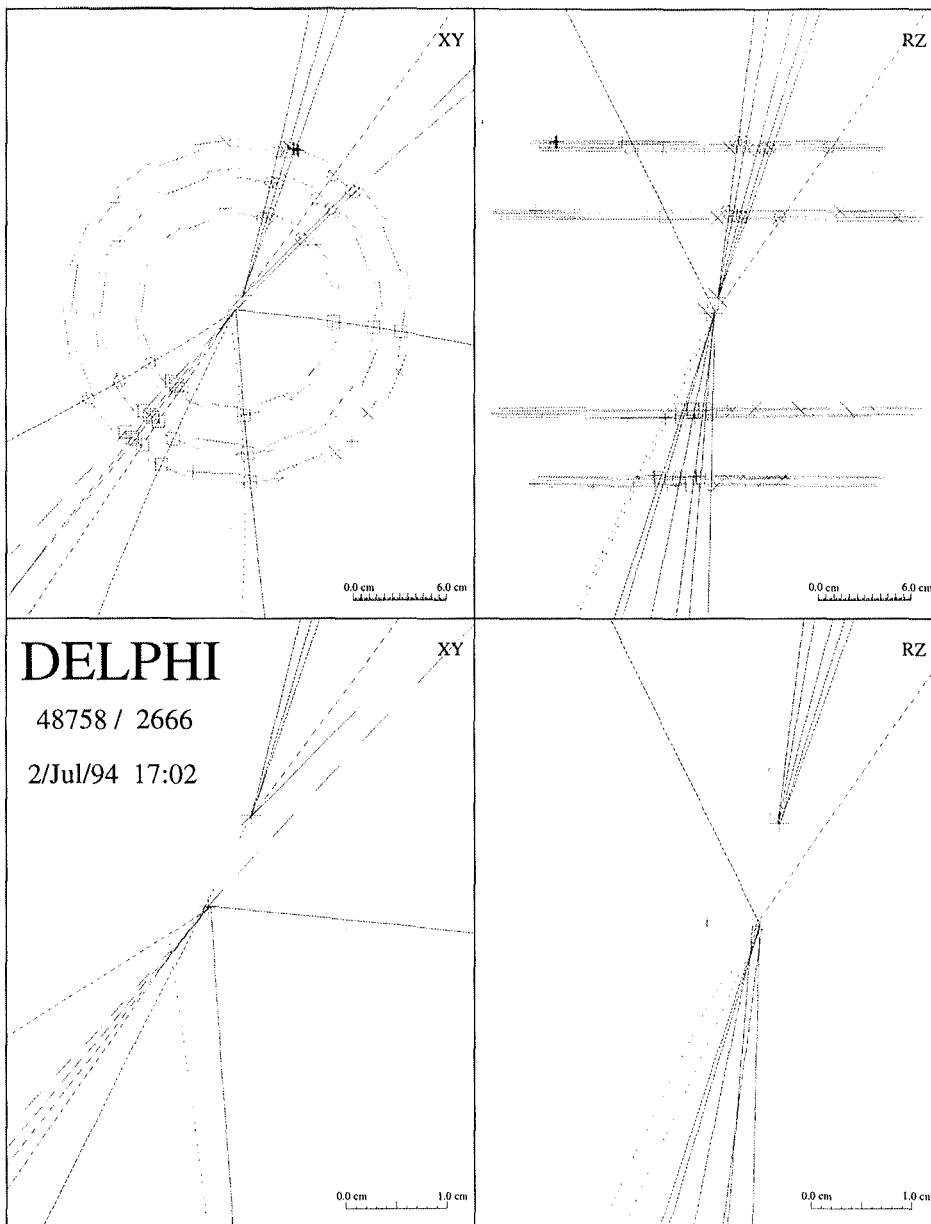


Figure 1.2: A  $Z \rightarrow b\bar{b}$  event reconstructed with the microvertex detector before the upgrade [9]

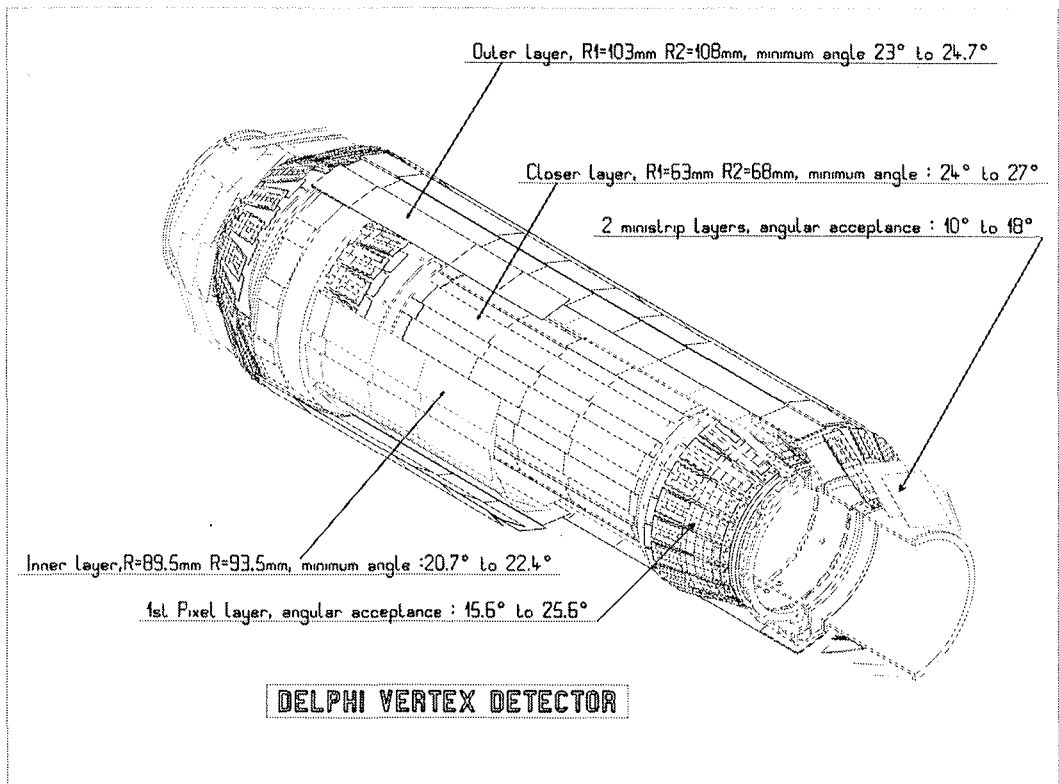


Figure 1.3: Line drawing of the new DELPHI Silicon Tracker with the cylindrical barrel part and the Very Forward Tracker mounted on the ends

and two double-sided silicon detectors measuring  $R\phi$  and  $Rz$  on both ends. The closer layer consists of double-sided detectors, where both  $R\phi$  and  $Rz$  strips are manufactured on the same wafer to minimise multiple scattering. All detectors on the closer and inner layer are readout by MX6 VLSI readout chips [10], which are also used for the VFT ministrip detector and are described in chapter 3. The modules have readout chips on both ends, that serve half of the module each. The entire detector is electrically spilt in its centre. The outer layer is read out by the TRIPLEX VLSI readout chip, which is similar to the MX6 chips but has an additional fast OR trigger output used for triggering purposes.

Before the prolongation the detector reconstructed the particle hits in the  $R\phi$  coordinate with a precision of  $7.6\mu\text{m}$  and with 9 to  $30\mu\text{m}$  in the  $Rz$  coordinate depending on the  $z$ -position[5]. A similar performance is expected for the new detector.

Further details about the DELPHI barrel microvertex detector can be found in references [11] and [12].

# Chapter 2

## The Very Forward Tracker

### 2.1 Physics motivation

One of the most exciting physics topics at LEP200 will be the search for the yet undiscovered Higgs boson. Extending this search to high mass regions is the highest priority for the four LEP experiments. The production of a higgs boson at LEP energies occurs through the production of a virtual  $Z$ , which couples to a final state  $Z$  and  $H$  as illustrated in figure 2.1. The Higgs discovery potential depends crucially on the centre-of-mass energy available and, as a rule of thumb, is given by

$$m_H \approx \sqrt{s} - 100\text{GeV} \quad [2] \quad (2.1)$$

After the bremsstrahlung process  $Z$  and  $H$  appear on their mass shell. As the coupling of the Higgs to fermions is proportional to the fermion mass, the decay of  $H \rightarrow b\bar{b}$  appears as the dominant decay channel for the Higgs. The different decay channels will be characterized by the decay products of the  $Z$ .

The main experimental signature of this process will thus be a two jet event accompanied by the decay products of the  $Z$ . The dominant decay channel into four jets requires good reconstruction of tracks in jets over the full solid angle.

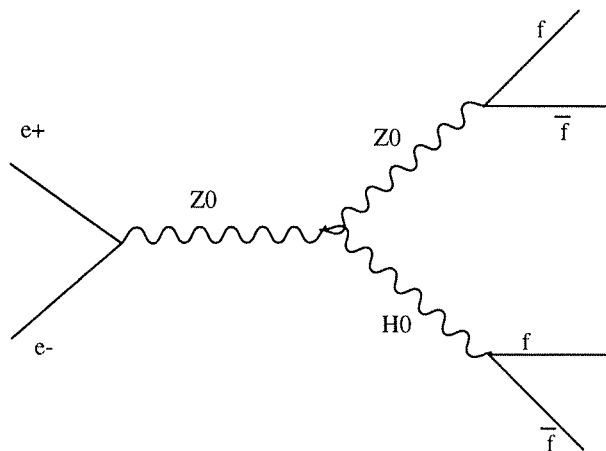


Figure 2.1: Feynman diagram for the Higgs production and decay

The most difficult among the decay channels is the channel with  $Z \rightarrow \nu\nu$ . To explore this decay mode characterised by missing energy an extremely tight hermeticity of the detector concerning the reconstruction of photons and charged tracks is required. Since the energy balance is a crucial factor in the background rejection good mass resolution is essential as well. The same experimental signature is given by events  $e^+e^- \rightarrow q\bar{q}\gamma$ , where the photon is lost and the forward pointing jet is badly reconstructed by the tracking system. Events of this type result in fake Higgs candidates and have to be suppressed by means of good photon and track reconstruction.

Another important source of background in the search for  $jj\nu\nu$  Higgs candidates, where  $j$  denotes the decay jet of the Higgs, is given by the events, where a pair of  $W$ s is produced which decays into the  $jjl\nu$  final state. If the lepton is not or badly reconstructed in the forward region, Higgs candidates are fake.

Both examples point out the importance of an hermetically closed tracking system in the forward region. By improving the tracking capability in the forward region with the VFT - an angular coverage of  $10^\circ < \theta < 25^\circ$  is considered - the signal efficiency in the Higgs search in the  $jj\nu\nu$  channel can be improved by 16% and the background events can be reduced by 32% [7].

LEP200 will also allow the search for supersymmetric particles. One interesting topic is the search for charginos, which are the mass eigenstates of the supersymmetric partners of  $W^+$  and  $W^-$  bosons. The chargino decays into a neutralino, the lightest supersymmetric particle, and a  $W$  boson as  $\chi^+ \rightarrow \chi^0 W^+$ . The neutralino will remain undetected, whereas the pair of  $W$  decays into four jets, two jets plus one lepton and one neutrino, or into two lepton and two neutrinos. The chargino events are characterized by a low visible mass and a high missing mass since the two lost neutralinos might be heavy. The background to this channel basically remains the same as in the Higgs search for  $jj\nu\nu$  signatures. The detection of charginos thus also requires excellent hermeticity of the tracking system. By upgrading the tracking system with the Very Forward Tracker, the background in the chargino detection can be reduced in the forward region by 55%. Consequently the sensitivity of DELPHI to this process at a given cross section is largely increased by the VFT. The sensitivity is defined as integrated luminosity needed to detect this process with a signal over background ratio greater than 5.

## 2.2 Layout of the VFT detector system

As pointed out in the previous section, precise and efficient tracking in the forward region of DELPHI is essential to successfully explore the physics topics at LEP200. The track reconstruction efficiency of DELPHI decreases below a polar angle of  $25^\circ$  and cannot cope with the requirements for LEP200. At small angles the forward chambers FCA and FCB have no supporting tracking detector and only rely on each other. Furthermore, the amount of material in front of them significantly worsens the tracking efficiency for particles in jets and for electrons. It is thus vital to provide a tracking detector in front of scattering material which can initiate the pattern recognition and support the track fitting.

In the foreseen angular acceptance region, Colomb scattering in the beam pipe dominates the track reconstruction precision towards the interaction point. Since, for this

reason no ultimate precision, necessary for  $b$ -tagging, can be achieved, the required intrinsic spatial resolution can be less than the one of the barrel microvertex detector.

The new tracking detector will also largely support the forward RICH detector. The FRICH requires extrapolation accuracies in the order of 1mrad and a few mm in space to efficiently perform particle identification.

The DELPHI Very Forward Tracker will provide

- efficient track reconstruction in a polar angular range of  $10^\circ < \theta < 25^\circ$  on each side of DELPHI, which allows track extrapolation to the other tracking detectors with an angular precision of 1-2mrad. The intrinsic spatial resolution in the detector plane is required to be  $70\mu\text{m}$ .
- The detector will provide stand-alone pattern recognition capability in front of scattering material with high efficiency and low number of ambiguous hits. This is particularly important for the reconstruction of events with high track multiplicity in the forward region.

The layout is constrained by severe limitations in the space available for active detector material as well as electronic and support systems.

The VFT detector extends the angular coverage of the microvertex detector by being added to the barrel in form of two end-cap-like segments. Each side consists of two planes of “macro” pixel detectors followed by two planes of “mini” strip detectors as illustrated in figure 2.2. One 360 degree cone of detectors is regarded as a plane. Each plane consists of two half rings, referred to as “crown”. Thus each crown covers approximately  $180^\circ$  in  $\phi$ .

The choice of large sized pixels ( $330 \times 330 \mu\text{m}^2$ ) in the “macro” pixel detector and large strip distance ( $200\mu\text{m}$ ) in the “mini” strip detector is motivated by the moderate spatial resolution required and substantially reduces the construction costs.

By developing a strip detector with large strip pitch, the number of readout channels is significantly reduced. This decreases the costs of the electronic system, the power consumption of the detector system and improves the reliability of the detector.

All planes are required to provide a two dimensional measurement of the trajectory. With this layout each track will be measured with at least 3 space points. A detailed simulation of this detector was carried out to optimize the layout regarding number and arrangement of planes [7]. Figure 2.4 illustrates the expected improvement in tracking efficiency for tracks in jets in two different momentum ranges versus the polar angle. For this simulation the present detector with and without VFT has been assumed. The plot drastically shows the improvement of the tracking efficiency with the VFT at angles below  $20^\circ$  degrees. The efficiency gain is nearly 50% and reaches a value of 80-90%.

The pixel detector helps to restrict the number of ambiguous hits to less than 10%. A further reduction to 6% is achieved by forming a “stereo angle” of four degrees between the strip orientation in the two strip planes. The pixel detector plane consists of 38 individual modules. Each modules incorporates 10 readout chips. Details about the pixel detector can be found in references [7][14].

The VFT is limited by a minimal inner radius of 6.5cm and a maximal outer radius of 11cm. The space used in  $z$  direction to accommodate the second pixel plane and the two ministrip planes is only 8.4cm on either sides of the barrel detector. These three planes



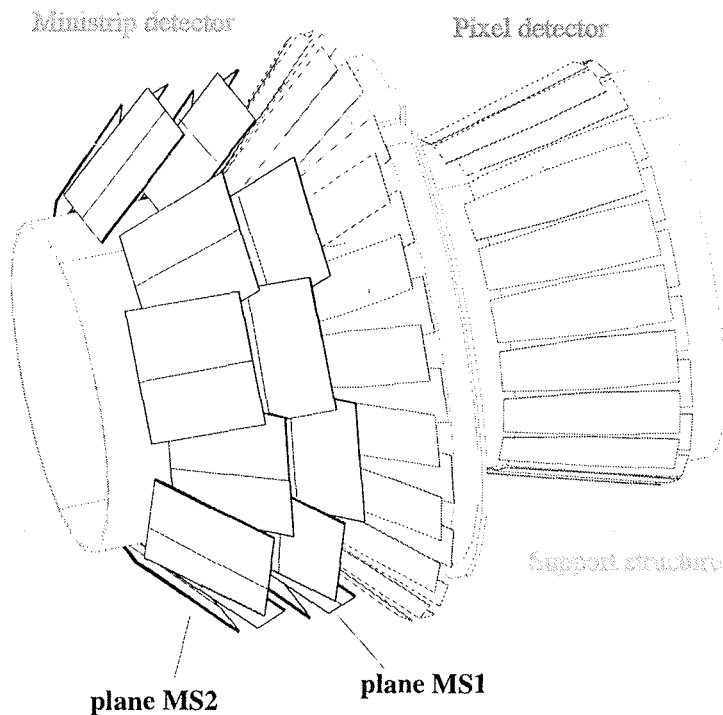


Figure 2.2: Planes of the DELPHI Very Forward Tracker

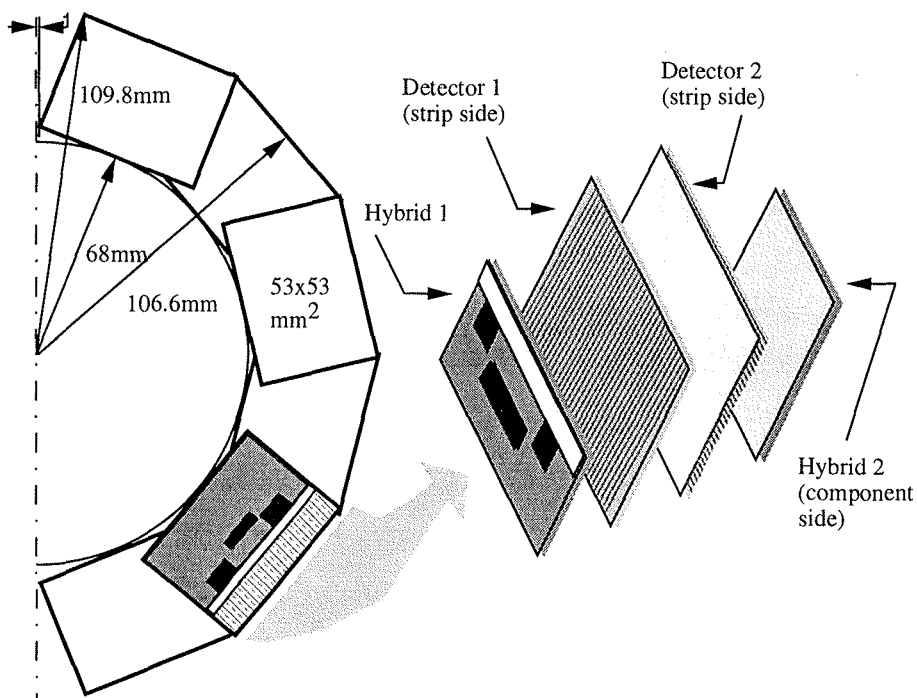


Figure 2.3: Schematic illustration of a ministrip crown with a blow-up view of a detector module.

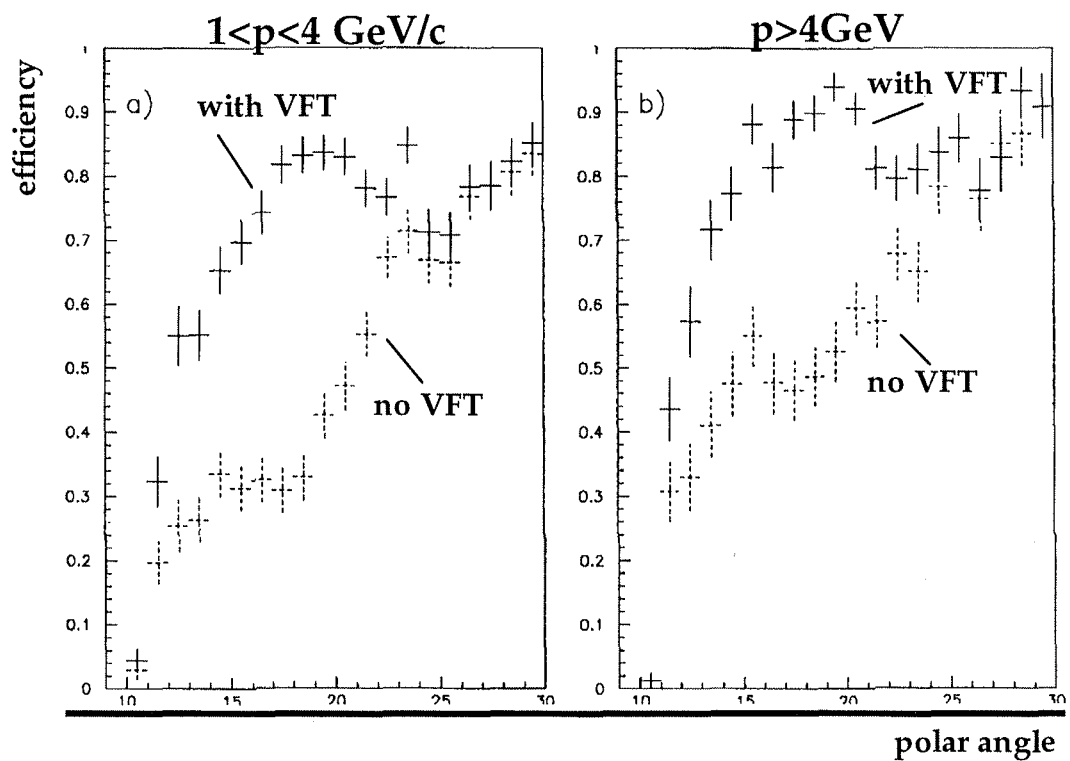


Figure 2.4: Track reconstruction efficiency for two different momentum ranges with and without VFT in the forward region. The efficiency is plotted versus the polar angle in degrees.

are supported in form of half cones on a half-cylinder mounted to the barrel. The regions with increased radiation length correspond to the end ring supporting the barrel ladders.

## 2.3 Design of the Ministrip detector

The aim in the design of the VFT ministrip detector was to provide a layout with the maximal possible angular acceptance in the tight space available and to achieve the required spatial resolution with the lowest possible number of readout channels to limit the detector costs. Extensive studies were carried out to optimize both the layout of the overall system [13][14] and the layout of the silicon detector [15][16][17].

The ministrip detector consists of 2 planes of detector modules on either side of the barrel. Each plane is made of 12 VFT modules surrounding the beam pipe. The modules are inclined with respect to the beam axis by  $50^\circ$  and measure the tracks in two orthogonal coordinates. Each plane consists of two half rings, called crowns, each of them supporting 6 modules.

The crowns are the basic elements of the ministrip and pixel detectors. The second pixel crown and the first and second strip crowns are supported on a thin aluminium half-cylinder on the inner radius. This scheme of independent crowns is vital to allow independent preparation and testing of the pixel and ministrip detector planes. The arrangement of the detector modules is shown in figure 2.3 in a projection along the beam axis. A cooling pipe is glued to the aluminium crown which supports the detector.

The VFT detector module consists of two single-sided strip detector, referred to as TOP and BOTTOM, glued together back to back. Since one of the biggest limitation in the construction of the VFT is space, the electronic hybrid is glued directly on the active detector area as illustrated in figure 2.3. The basic features of a VFT ministrip module are:

- The silicon detectors have  $200\mu\text{m}$  readout pitch with one intermediate strip that is not directly connected to an amplifier channel. The charge deposited on the intermediate strip is capacitively coupled to the adjacent strips (“readout strip”) which are connected to the amplifier. The DC ohmic coupling is small as the resistance between strip is high. This scheme allows to keep the total number of electronic channels low and, as will be shown later, fulfils the requirements concerning spatial resolution.
- The shape of the detector is quadratic. This allows to use a single layout for all required silicon detectors. The two dimensional measurement is achieved by rotating one detector with respect to the other by  $90^\circ$ . The single design for the entire detector system results in substantial savings and the highest possible flexibility during the production of the whole system.
- If a single modules is traversed by  $n$  tracks, the combination of hit position between the two sides of the detector results in  $n$  combinations reflecting the real hits and  $n(n - 1)$  fake hit combinations. To suppress the fake hit combinations the hit positions between two planes can be correlated. The strip implants have an angle of  $\pm 2^\circ$  with respect to the detector edges. The modules are mounted on the crowns

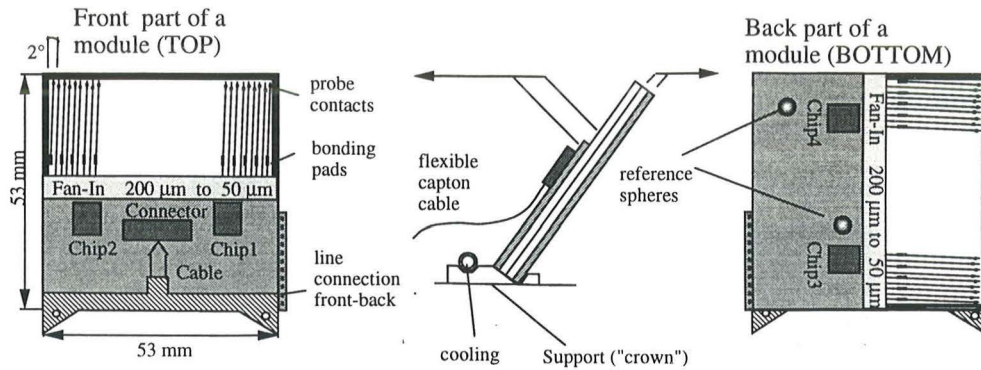


Figure 2.5: Components of a VFT ministrip module.

in a way that the strips pointing to the beam axis in the first ministrip plane will face the same strips in the second ministrip plane. Thus, a total stereo angle of  $4^\circ$  is created between the strips of the two planes. The stereo angle significantly reduces the number of ambiguities for jet events where several tracks pass a single module, as already stated.

- The overlap of the modules in a plane corresponds to nearly 20% of the covered area. This overlap allows an alignment of the modules with respect to each other with tracks and increases the average number of measurements per track.

The layout of a single VFT ministrip module is illustrated in figure 2.5. The module shown corresponds to a module in the MS 1 plane. The modules in the MS 2 plane are flipped around their vertical axis, i.e. TOP and BOTTOM side are reversed. The modules in plane MS1 and MS2 are identical, only the side facing the vertex is flipped in the mounting on the crowns.

The two single-sided silicon detectors are glued together back to back with a thin aluminium wire running in-between to provide the backplane connection. The readout strips are bonded to a fan-in which is used to match the readout pitch of  $200\mu\text{m}$  to the chip channel distance of  $50\mu\text{m}$ . The fan-in is manufactured separately, as the thin lines require a smooth surface. The fan-in connects the readout lines to two MX6 readout chips which are placed on Beryllium Oxide ceramic hybrids. The hybrids are directly glued to the junction side of the silicon detector. BeO is chosen for its high radiation length and for its excellent thermal conductivity - the main heat source being the chip above the detector. Only one hybrid (TOP detector) carries a connector, the second hybrid (BOTTOM detector) is connected to the TOP side along a row of contact holes on the side of the hybrid. The connection is made by thin wire connections hole to hole. The four MX6 chips on one module are read out in series.

The silicon detectors<sup>1</sup>, as illustrated in figure 2.6, have a dimension of  $53 \times 53\text{mm}^2$  with 511  $\text{p}^+$  implant lines with a pitch of  $100\mu\text{m}$ . The width of the implant is  $60\mu\text{m}$ . Every second implant is covered by a metal layer readout line is separated from the implant by  $200\text{nm SiO}_2$ . The readout lines have the same width as the implant and have three bond pads in the middle of the line for the connection to the fan-in. For test purposes,

<sup>1</sup>produced by Micron Semiconductor Ltd., Lancing, UK

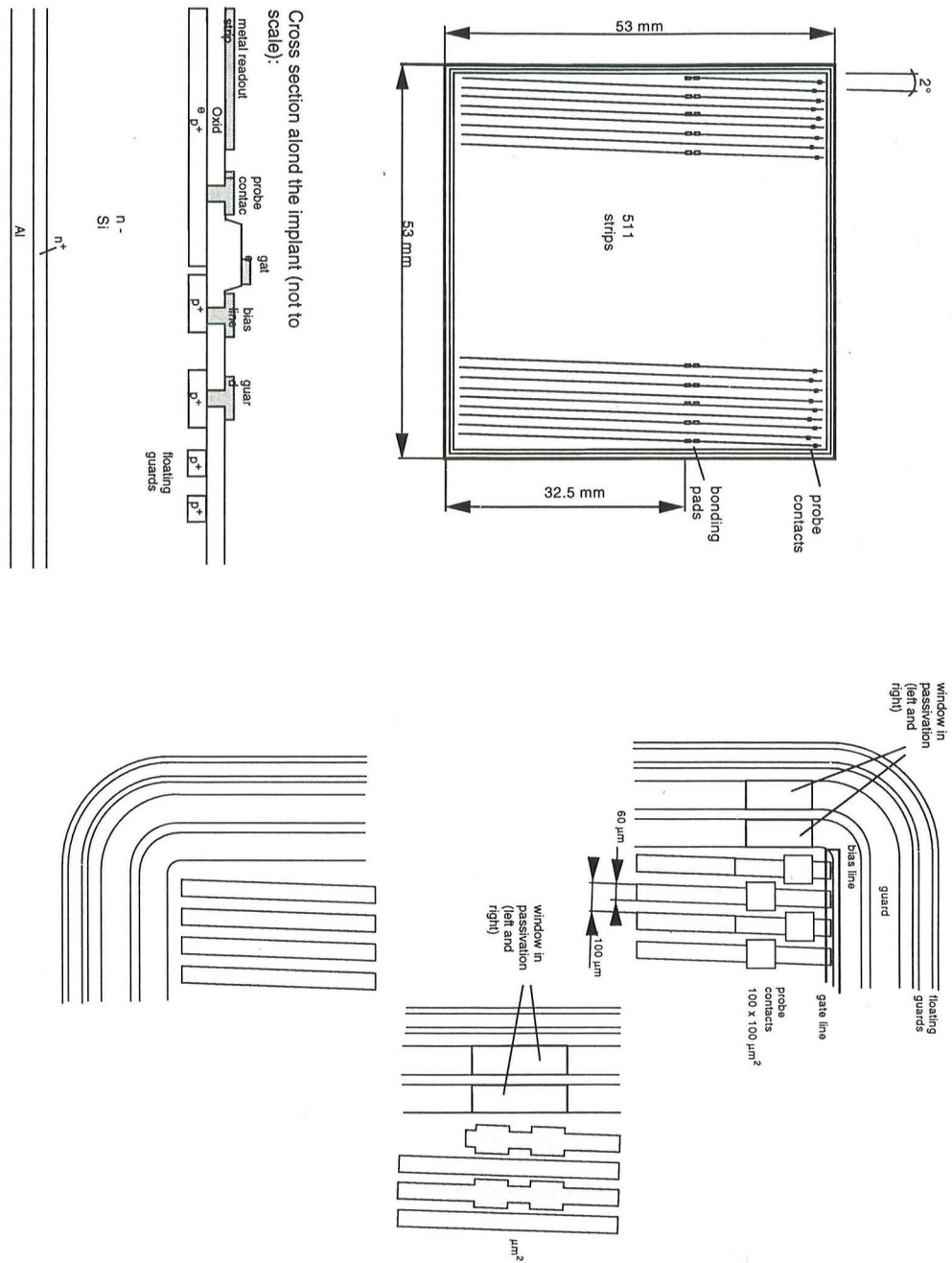


Figure 2.6: Components of a VFT ministrip module.

each implant has probe pad on one end of the strip. The strip implant is connected to the common bias line through a high resistor, formed by the channel resistance of a field effect transistor, usually referred to as FOXFET structure<sup>2</sup>.

The modules on each crown are connected to the so-called repeater board, which provides the control signals to the detector and amplify the analog output of the MX6 chips. The repeater connects via 25m long cables the detector system to the front end electronics and power supplies in the counting room, where the digitization of the analog output is done. The repeater boards have a half-disk shape and are mounted directly behind the MS 2 detector plane surrounding the beam pipe. A schematic overview of the readout electronics is shown in figure 5.8.

---

<sup>2</sup>see chapter 3 and 5 for reference

# Chapter 3

## Silicon strip detectors with large strip pitch

After a brief review of the properties of silicon strip detectors, the main considerations leading to the final layout of the VFT ministrip detector plaquette shall be presented. The influence of geometrical parameters on the detector main figures, such as signal to noise performance, spatial resolution and charge collection shall be discussed. The main part of the chapter is dedicated to tests of detector prototypes and final detectors in several beamtests.

Also for future experiments at the Large Hadron Collider LHC large pitch silicon detectors are of special interest as large areas have to be covered [32][33]. The enormous number of electronic channels for the LHC silicon detectors lead to severe problems concerning costs, readout electronics and thermal management. The development of large strip pitch detectors can help to overcome these difficulties. In total 11 different, known as well as newly developed, detectors are tested to understand the influence of various layout parameters on the detector performance. The signal measurement and spatial resolution strongly depend on the strip pitch, distance of readout strips, implant width and detector capacitances. In the presented measurements these parameters are varied over a large range, to demonstrate the capabilities and limitations of particular detector designs.

### 3.1 Basic components of silicon strip detectors

Silicon is mainly used in a single crystal formation, typically (111), for applications like semiconductor particle detectors. The silicon atoms are arranged in a diamond-like face centred cubic lattice. Each silicon atom is surrounded by four other silicon atoms in a tetrahedral configuration. Each atom shares its four valence electrons with neighbouring atoms to form covalent bonds. At low temperatures, all valence electrons participate in the covalent bonding and no electrons are available for electrical conduction. At room temperature thermal vibration leads to the destruction of covalent bonds and electrons enter the conduction band which causes an electrical conductivity of the semiconductor. At the same time, electron vacancies (holes) in the covalent bond can be refilled by neighbouring electrons. This displacement of holes can be interpreted as hole current which additionally contributes to the electrical conductivity.

The electrical conductivity of semiconductor material is also sensitive to externally triggered processes such as illumination in the UV range and ionisation. These processes cause a temporary increase in the conductivity by creating free electron-hole pairs. The capability of silicon to collect this created charge allows its use as particle detector. The energy gap between the conduction and valence band can be used to distinguish between conducting, semiconducting and insulating material. For insulators, the transition probability for electrons to enter the conduction band from the valence band is almost zero as the band gap is large. Contrary to the insulator, the conduction and valence bands are overlapping in a conducting material, leading to filled energy levels in both bands. An intermediate configuration is found in semiconductor materials. An energy gap of 1.11 eV separates these bands in silicon. The density of free electrons and holes being available for conduction in pure intrinsic silicon  $n_e = n_h = n_i$  is described by Fermi-Dirac statistics as

$$n_e = N_c \exp -\frac{E_c - E_f}{kT} \quad (3.1)$$

$$n_h = N_v \exp -\frac{E_f - E_v}{kT} \quad (3.2)$$

$$n_i = \sqrt{N_c N_v} \exp -\frac{E_g}{2kT} = AT^{\frac{3}{2}} \exp -\frac{E_g}{2kT} \quad (3.3)$$

where  $N_c(T)$  and  $N_v(T)$  denote the effective densities of occupied states at the conduction and valence band edges.  $n_e$  and  $n_h$  stand for the electron and hole density.  $E_f$  denotes the Fermi energy, i.e the energy at which 50% of the possible energy states are filled. At room temperature, the intrinsic charge carrier concentration  $n_i$  is  $1.45 \cdot 10^{10} \text{ cm}^{-3}$ . The resistivity  $\rho$ , as the inverse of the conductivity  $\gamma$ , can be evaluated knowing charge carrier densities and their mobility  $\mu_{e,h}$

$$\rho = \gamma^{-1} = \frac{1}{q(\mu_e n_e + \mu_h n_h)} \quad (3.4)$$

For pure silicon the mobility at room temperature is  $1350 \text{ cm}^2/\text{V}$  for electrons and  $480 \text{ cm}^2/\text{V}$  for holes. This yields a resistivity of intrinsic silicon of  $235 \text{ k}\Omega\text{cm}$ . The linear correlation between drift velocity and electric field strength  $v = \mu E$  at a constant mobility holds only for low fields. At fields higher than 5 to 10 kV/cm the mobility decreases. This results in a slow saturation of the drift velocity. Impurities in the silicon bulk can introduce additional energy levels in the band gap which changes the effective number of free charge carriers. The resistivity can vary from a few  $\Omega\text{cm}$ , typically used for integrated circuit manufacturing, to few  $\text{k}\Omega\text{cm}$ , necessary for particle detector fabrication. A desired resistivity between  $2 \text{ k}\Omega\text{cm}$  and  $10 \text{ k}\Omega\text{cm}$  limits the effective number of allowed impurities to  $4 \cdot 10^{11} - 2 \cdot 10^{12} \text{ cm}^{-3}$ . This has to be compared to  $5 \cdot 10^{22} \text{ silicon atoms/cm}^3$  and illustrates the extraordinary requirements to the cleanness of the production and handling of modern silicon particle detectors.

In order to use silicon as a particle detector, nearly all free charge carriers have to be removed from the silicon bulk. This shall be illustrated by the following consideration: A  $1 \text{ cm}^2$  large and  $300 \mu\text{m}$  thick continuous counter made of pure intrinsic silicon contains in total  $4.4 \cdot 10^8$  free electron-hole pairs, a strip like counter with  $5 \text{ cm}$  length and  $100 \mu\text{m}$



width contains  $2.2 \cdot 10^7$ . These numbers are further increased by the unavoidable presence of impurities. A traversing minimum ionising particle loses on average 116 keV of its energy in such a detector, which results together with an ionisation energy of 3.66 eV/e-h pair, in a total signal of 32000 e-h pairs. For the strip-like counter the signal is thus three orders of magnitude lower than the number of free carrier pairs. This faint signal would completely be covered by the fluctuations of the detector current. The most probable energy loss corresponds to 24000 electrons.

One method to remove free charge carriers from the silicon bulk is to form a Schottky diode by evaporating a thin metal layer on pure silicon. As a consequence of the different energy levels in the metal and the silicon bulk, a narrow depletion region, i.e. a region free of mobile charge carrier, is created below the metal which acts as the detection volume. Although it has been shown that Schottky diodes are capable of detecting particles [18],[19],[20] their application in high energy physics experiments is limited by difficult handling, high leakage current and small signal. Modern silicon particle detectors are commonly based on a p-n diode structure offering superior performance.

### 3.1.1 The p-n junction

When the intrinsic silicon bulk is doped with impurity atoms, those are accommodated in the tetrahedral lattice structure. If the impurity atom has five valence electrons, like phosphorus or other elements of the fifth column of the element periodic table, four are used to form covalent bonds with the neighbouring silicon atoms. The fifth electron is loosely bound and contributes to the conductivity. Impurities with more valence electrons than silicon are called "donor" atoms and the doped silicon is referred to as n-type material. The energy level introduced by the dopant lies only a few hundredths of an eV below the conduction band and therefore allows the electrons to enter it. The Fermi energy is shifted upwards just below the conduction band as illustrated in figure 3.1.

In case the impurity atom has only three valence electrons, e.g. Boron, one electron is missing in a covalent bond, resulting in a free hole which is then responsible for additional conductivity. The Fermi energy for silicon being doped with "acceptor" atoms is shifted downwards next to the valence band. The semiconductors of this type are said to be p-type. Typical doping concentrations in the order of  $10^{12} \text{cm}^{-3}$  are used in the device fabrication for particle detection. Higher doping concentration ( $10^{20} \text{cm}^{-3}$ ) applied to the surface results in a low resistivity, necessary for good ohmic contacts to the external world. Highly acceptor or donor doped materials are usually indicated by "p<sup>+</sup>" and "n<sup>+</sup>".

When p-type and n-type silicon is joined together to form a p-n junction, the different free charge carrier concentrations for electrons and holes lead to a diffusion current across the junction. Electrons, the majority carriers in the n-type material, will diffuse to the p-side and recombine with holes. Fixed positive donor ions are left behind in the n-type region of the junction. The same is true for holes in the opposite direction. The remaining positive and negative space charges in the junction region lead to an electric field that counteracts the diffusion current. As in equilibrium the Fermi energy levels are required to be the same in n-type and p-type material, it causes a bend in the conduction and valence band as illustrated in figure 3.1. A "built-in" potential difference  $V_{bi}$  establishes itself between the n-type and p-type layer. For an abrupt junction Poisson's equation

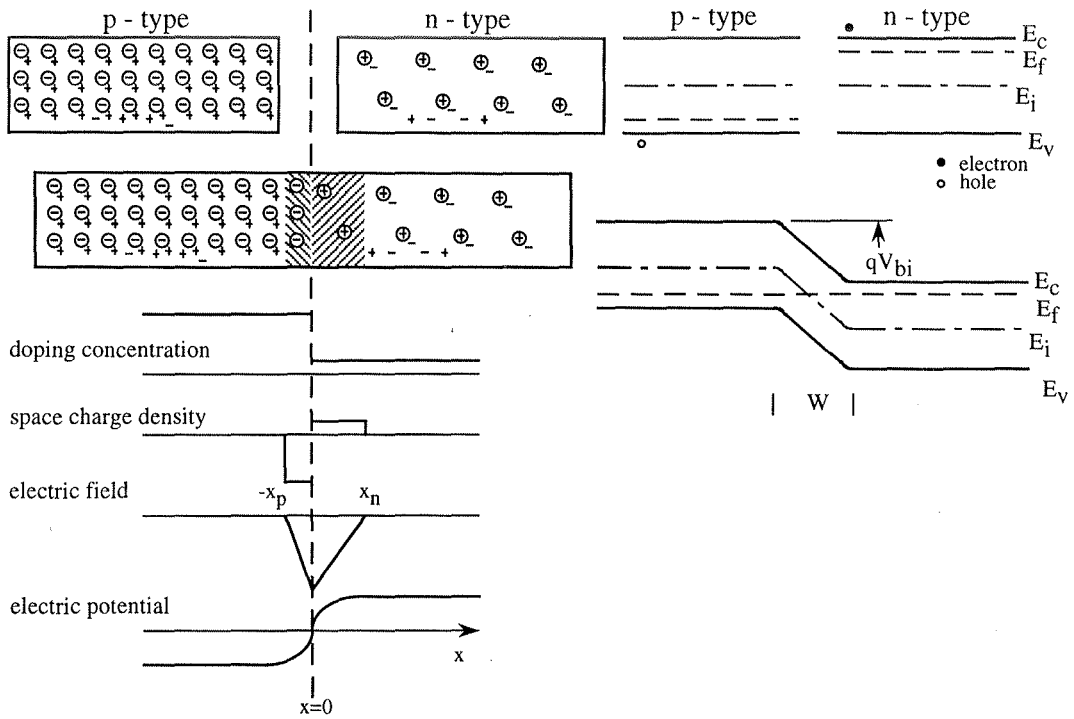


Figure 3.1: Schematic illustration of the charge densities and energy levels in the p - n junction.

yields the following correlation between acceptor ion density  $N_a$ , donor ion density  $N_d$  and the width of the depleted region  $W = x_p + x_n$ .

$$-\frac{\partial^2 V}{\partial x^2} = \frac{q}{\epsilon} [n_h(x) - n_e(x) + N_d(x) - N_a(x)] \quad (3.5)$$

Neglecting tails of the majority carrier concentration in the depleted region and assuming a constant ion density in the depleted region the above equation simplifies to

$$-\frac{\partial^2 V}{\partial x^2} \approx \frac{q}{\epsilon} N_d \quad \text{for } 0 < x \leq x_n \quad (3.6)$$

$$\frac{\partial^2 V}{\partial x^2} \approx \frac{q}{\epsilon} N_a \quad \text{for } -x_p \leq x < 0 \quad \text{and} \quad (3.7)$$

$$E(x) = \frac{qN_d}{\epsilon} (x - x_n) \quad \text{for } 0 < x \leq x_n \quad (3.8)$$

$$E(x) = -\frac{qN_a}{\epsilon} (x_p + x) \quad \text{for } -x_p \leq x < 0 \quad (3.9)$$

Integrating above equations to obtain the potential distribution gives for the built-in voltage

$$V_{bi} = \frac{1}{2} E(x=0) [x_p + x_n] \quad \text{with} \quad (3.10)$$

$$E(x=0) = \frac{qN_d x_n}{\epsilon} = \frac{qN_a x_p}{\epsilon} \quad (3.11)$$

Equation (3.11) simply reflects the charge neutrality demanded for the entire p-n diode. The extension of the depletion region into the p-type and n-type material results from the combination of the last equations as

$$x_p = \sqrt{\frac{2\epsilon V_{bi}}{qN_a(1 + \frac{N_a}{N_d})}} \quad (3.12)$$

$$x_n = \sqrt{\frac{2\epsilon V_{bi}}{qN_d(1 + \frac{N_d}{N_a})}} \quad (3.13)$$

In practice, the p-n diode for detector manufacturing is based on a high resistivity, low donor concentration ( $N_d \approx 10^{12} \text{cm}^{-3}$ ) n-type bulk on which a highly doped p<sup>+</sup> layer is implanted ( $N_a \approx 10^{15} \text{cm}^{-3}$ ). This leads to a deep depletion region on the n-side being the active detector volume but a very shallow one on the p-side. For detectors, the shallow p<sup>+</sup> implant represents the measuring electrode and is required for the depletion of the n-bulk material, which acts as the active particle detection volume.

When a positive voltage is applied on the p-side and a negative on the n-side the depletion region will shrink and the current between the terminals grows exponentially. This corresponds to the forward biased operation of the diode. With reverse biasing applied to the diode, i.e. a negative voltage on the p-side and a positive one on the n-side, the depletion region will grow with the square root of the applied voltage  $V_B$ , which is described by equation (3.13). Using the resistivity of n-type material, respecting  $N_d \gg N_a$  in the n-type bulk and replacing  $V_{bi}$  by  $V_{bi} + V_B$ , the depletion depth is given by

$$W = \sqrt{2\epsilon\rho\mu_e(V_B + V_{bi})} \quad \text{with} \quad (3.14)$$

$$\rho = \frac{1}{q\mu_e N_d} \quad (3.15)$$

A schematic representation of the diode current versus applied voltage for forward and reverse biasing operation is shown in figure 3.2.

From the above equation the voltage  $V_{fd}$ , necessary to extend the depletion region over the entire detector, can be derived.  $V_{fd}$  is referred to as full depletion voltage.

$$V_{fd} = \frac{T^2}{2\epsilon\rho\mu_e} \quad (3.16)$$

It depends on the detector thickness  $T$  and the resistivity on the silicon wafer used for the detector.

The diode leakage current in reverse biased operation is due to thermal generation of minority carriers in the depletion region. Additional energy levels in the band gap due to impurities or radiation damage can strongly enhance the leakage current.

A pn-junction diode provides an efficient way of achieving an active detection volume where a very low level of constant current can be maintained. The low number of free charge carriers allows the measurement of the small charge deposited by an ionising particle. In the reverse biased pn-junction the deposited signal from a traversing particle is much bigger than the fluctuations of the leakage current hence allowing a clear detection of traversing particle.

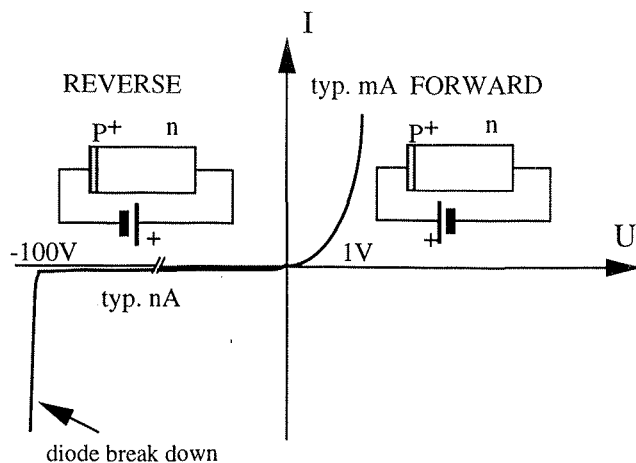


Figure 3.2: Current-voltage characteristics of a diode under forward and reverse biasing.

### 3.1.2 Layout of silicon strip detectors

Position sensitivity of a silicon detector is obtained by dividing the p-n diode into smaller segments that act as individual independent electrodes. The use of planar technology for the construction of the p-n diode allows a precise manufacturing of these electrodes in nearly any kind of shape and in sizes ranging from  $10\ \mu\text{m}$  to several cm. For silicon strip detectors the detector surface is segmented in very fine parallel diode strips. Figure 3.3 shows a schematic cross-section through the strip detector. When a traversing particle ionises the silicon bulk, the generated electrons and holes drift towards the  $n^+$  and  $p^+$  sides in the presence of the electric field caused by the depletion voltage. So doing they induce a signal on the electrodes. Every strip or every second one is individually read out by an amplifier, thus the position of the traversing particle results primarily from the strip position where the signal is detected. There is no sensitivity along the strip. The illustrated configuration gives only the position coordinate perpendicular to the strip orientation in the detector plane.

A brief summary of the role of the detector components shall be given: The  $p^+$  implant is responsible for depleting the n-bulk and acts as the measuring electrode. The n-type material is the detection volume and the  $n^+$  implantation serves as an ohmic contact to the high resistivity n-bulk.

An aluminium metal layer above the  $p^+$  implant provides the contact to the amplifier input. This type of contact is commonly referred as DC coupling contact. When the metal line is in direct ohmic contact to the strip implant, not only the signal current but also the constant detector leakage current flow into the amplifier input. Unless special precautions are taken in the amplifier design, this can result in severe operation problems once the leakage current reaches a level where it saturates the charge amplifier.

One way to avoid this problem is to block the leakage current by an insulating silicon dioxide layer between the implant and the aluminium readout line. The (high frequency) signal current is still induced in the readout line via the capacitance formed by the strip implant, the silicon oxide and the metal readout line and therefore measured by the amplifier. The capacitance between strip implant and readout line is commonly referred

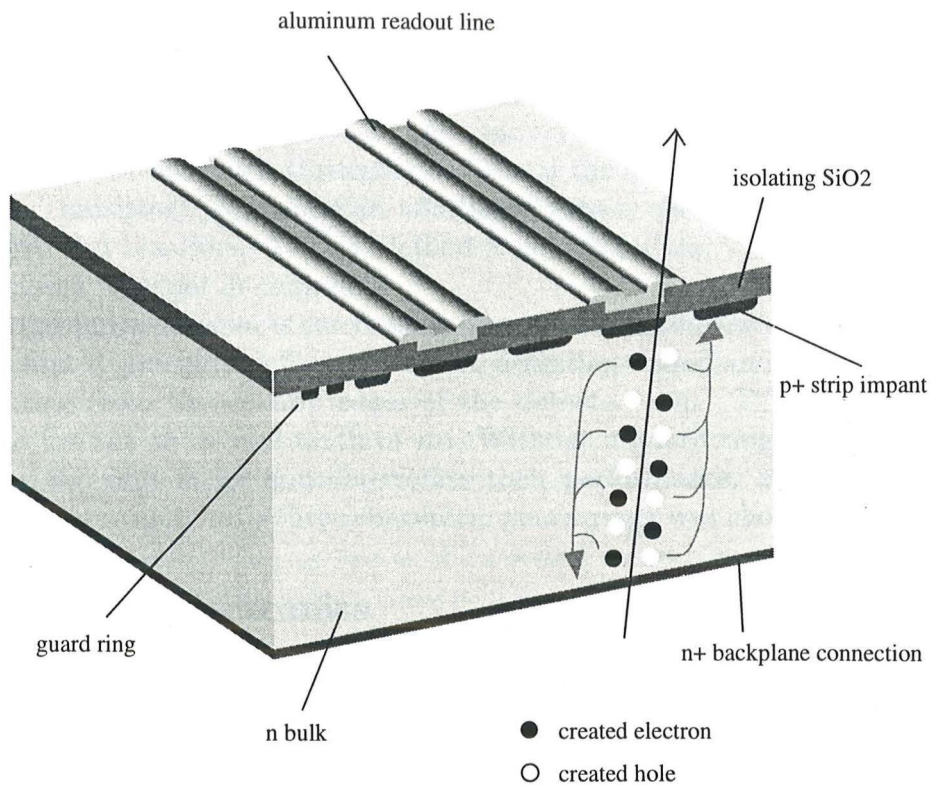


Figure 3.3: Schematic layout of a silicon strip detector.

as “coupling capacitance”. A thin layer of  $\text{SiO}_2$  is created during the detector production by thermal oxidation and therefore widely used although other materials like silicon nitride can serve the same purpose [21]. Another possibility to achieve this AC coupling between strip and amplifier is to use external capacitances, an approach which was originally chosen by the ALEPH collaboration at LEP.

Using the AC coupled readout scheme leaves another problem: In the AC coupling scheme the implants are isolated from the amplifiers. A common so called bias line running along the detector edge connects the strips through individual resistors to a fixed potential. The value of this bias resistors has to be sufficiently high to isolate the strips from each other and to keep the noise down. In the presence of higher strip leakage current the uniformity of the resistors is of importance as big variations in the resistor values lead to variations in the applied strip depletion voltage. Different techniques have been explored to manufacture such resistors with values of several  $\text{M}\Omega$  on the little space available at the end of the strip. The choice of technique used is mainly determined by external constraints like necessity of radiation hardness, uniformity and space available. Polysilicon layers are commonly used for producing resistors in MOS (metal-oxide-semiconductor) electronic technology. Thin polysilicon lines, on which the sheet resistance is controlled by ion implantation, connect the strip implant to the biasline. Values in the order of 10-20  $\text{M}\Omega$  have been achieved [22][23].

Another possibility to bias the strips is based on a  $\text{p}^+\text{np}^+$  junction, where the first  $\text{p}^+$  is the strip implant and the second the bias line implant [24]. When a negative voltage

is applied to the bias line a depletion region will form towards the strip implant. At a certain voltage it reaches the strip. Further increase of the voltage also increases the potential on the strip and starts biasing it. This method is called reach-through biasing. In this case the bias resistor is given by the channel resistance of the  $p^+np^+$  structure. A refined technique of the reach-through structure is the so called FOXFET (Field OXide Field Effect Transistor) [25] where an additional gate is used to steer the offset voltage between strip and bias line. As this method is chosen for the VFT ministrip detector it will be reviewed in detail in chapter 5.

Finally the entire detector is surrounded by a guard ring on the  $p^+$  side, which purpose is twofold: first it precisely defines the active detection region and second it absorbs the leakage current from the cutting edges of the detector chip. This leakage current can vary from a few nA to several tenth of  $\mu A$ . Without a guard ring the current would be absorbed by the edge strips and deteriorate their performance. For the VFT ministrip detector a configuration with three concentric guard rings was chosen.

### 3.1.3 Readout electronics

The depletion voltage between  $p^+$  strip and  $n^+$  backplane, applied to create a reverse biased junction, leads to an electric field between the two detector side. After a particle traversed the detector, the created holes and electrons drift towards the electrodes on the top and reverse side of the detector. This drift induces a current signal on the electrodes. The total induced charge and the signal shape depend on the deposited charge, the drift path, velocity of electrons and holes and the geometry of the detector. The signal shape is furthermore influenced by the connected electronics.

This induced signal can serve two purposes. As its total charge is proportional to the created ionisation charge it can be used to measure the energy loss of the absorbed or traversing particle. If signals are measured on few strips, like in detectors with small strip pitch, the signals of different strips can be used to measure the charge sharing between them which is important for applications where highest spatial resolution is desired. Secondly the position of the traversing particle can be obtained from the position where the induced charge is measured.

For the application with vertex detectors in collider experiments the readout electronics has to fulfil various requirements:

To measure the deposited charge the diode strips are connected to individual charge amplifiers integrating the signal current for each strip on their feedback capacitor. The voltage output signal of the charge amplifier is as a measure of the deposited charge. A brief summary of the properties of charge amplifiers can be found in the appendix. Afterwards the preamplifier signal of each channel is passed through a filter and shaping stage and is finally stored in capacitors for later readout.

Each strip requires its own charge amplifier. "Very Large Scale Integration" (VLSI) electronics is necessary to cope with the high channel density. Furthermore, low noise performance is desired for a precise measurement of the deposited charge. To achieve low noise, special care is necessary in the design of the preamplifier stage as it mainly determines the noise performance of the detector/electronic system. Impedance mismatch between detector and input transistor or sensitivity to the transient of control signals can

significantly deteriorate the performance of the system .

Due to the high channel density in vertex detectors the readout electronics has to be as compact as possible and hence requires the integration of many components in single chips. As multiple scattering of particles has to be limited for precise track reconstruction a minimum amount of material like cables, printed circuit boards or support structure is desired. With the availability of VLSI technology most of the readout electronics can be packed in few and small chips. This allows to mount it directly on the side or on top of the detector.

With the large number of channels also power consumption of the electronics and consequently the thermal management of the system is of crucial importance. The power consumption of each channel cannot exceed a few mW in order to limit the total dissipated heat and guarantee the stability of the system. The production of the readout chips in MOS (Metal-Oxide-Silicon) technology offers several advantages. It allows the integration of both the analog and digital control part of the electronics on a single chip. The power consumed by each chip is low. Moreover MOS technology allows to build small, high gain amplifiers as well as accurate capacitors and transistors, important for the uniformity of the electronics.

Nowadays many different VLSI readout chips optimized for their application in high energy physics experiments are available. Two different designs shall be reviewed here as they are used for the testing and final readout of the VFT ministrip detector: The VIKING and VA2 [26], [27] readout chips were used for tests of ministrip prototypes and the evaluation of different detector layouts. The Microplex readout chip MX6 [10] is reviewed as it is used for the new silicon tracker readout.

### The VIKING readout chip

The VIKING and VA2 readout chips have been developed at CERN for the readout of silicon strip detectors at LEP experiments. Each chip contains 128 charge sensitive preamplifiers. Figure 3.4 shows a schematic diagram of the analog part for one channel with preamplifier, shaper and hold circuit. The preamplifiers are followed by CR-RC shapers together with a sample and hold circuit where the analog information of each channel is stored. A common digital part controls the readout of the analog signals of all channels. During the readout phase the analog information for 128 channels is time multiplexed to a single analog output node for each chip. A maximum readout clock frequency of 10 MHz can be obtained. For the tests presented here a readout frequency of 1 MHz was chosen. Typical values of the individual components are given in the diagram.

The feedback capacitor of the charge sensitive preamplifier integrates the signal current coming for the detector and a voltage step of  $Q/C_{fb}$  appears on its output. For a high gain of the charge amplifier  $C_{fb}$  has to be sufficiently low. The output signal resets itself to the quiescent level with a time constant of  $R_{fb}C_{fb}$ . The resistor  $R_{fb}$ , realised as a FET, has to be small enough to avoid signal pile-up for subsequent hits on the same strip and large enough to minimise noise as it acts as a parallel resistor on the charge amplifier input (see below). The voltage output signal of the preamplifier is passed through the following CR-RC shaper formed by the capacitor  $C_c$  and the feedback network of the shaping amplifier. For our tests a shaping time of  $1.8\mu\text{s}$  is chosen. The shaper output reaches its maximum

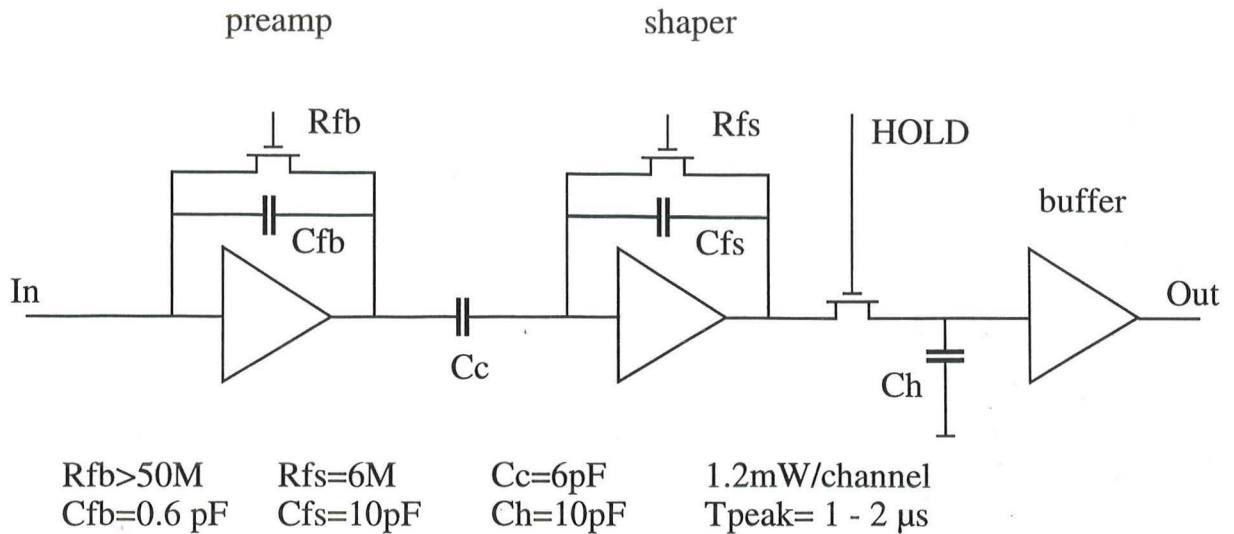


Figure 3.4: Schematic diagram of the analog part for one VIKING channel.

at a constant time after a particle has traversed the detector. The voltage presented to the hold capacitor  $C_h$  follows the output of shaper as long as the “HOLD” FET is in its conducting state. This HOLD switch is used to trigger the storage of the shaper output signal on  $C_h$ . This maximum is proportional to the deposited charge. As the maximum of the shaper appears delayed by the shaping time on the “HOLD” capacitor, there is sufficient time to generate an external trigger for this event. The external trigger is used to switch the “HOLD” FET off when the shaper signal has reached its maximum. The capacitor  $C_h$  is then charged up to a voltage proportional to the detector signal and holds it until it is read out.

### The Microplex chip MX6

The Microplex chip MX6, designed at the Rutherford Appleton Laboratory, also contains the analog and digital part for the readout of 128 channels in a single chip. This chip too has been optimized for its application in LEP experiments. This design follows a different strategy for measuring the output of the charge amplifier, known as “correlated double sampling” of the signal. Figure 3.5 presents a schematic overview of the circuit for one of the 128 channels, together with the timing of control signals used during the data capture cycle.

The aim of the correlated double sampling is to measure the preamplifier output first before the particle traversed the detector and a second time after its passage. Subtracting the two measurements ideally yields a signal independent of baseline shifts.

Before the data capture cycle, i.e. before a particle will traverse the detector, a reset signal is applied to the reset transistor in the charge amplifier feedback loop. The reset transistor is in its conduction state, and thus the feedback capacitance is shorted and the amplifier is brought back to its quiescent point. During the data capture cycle the reset transistor is off and represents a high resistor in the feedback. After the reset transistor is switched off the two pass transistors  $S_1$  and  $S_2$  still remain on. The two capacitances  $C_1$



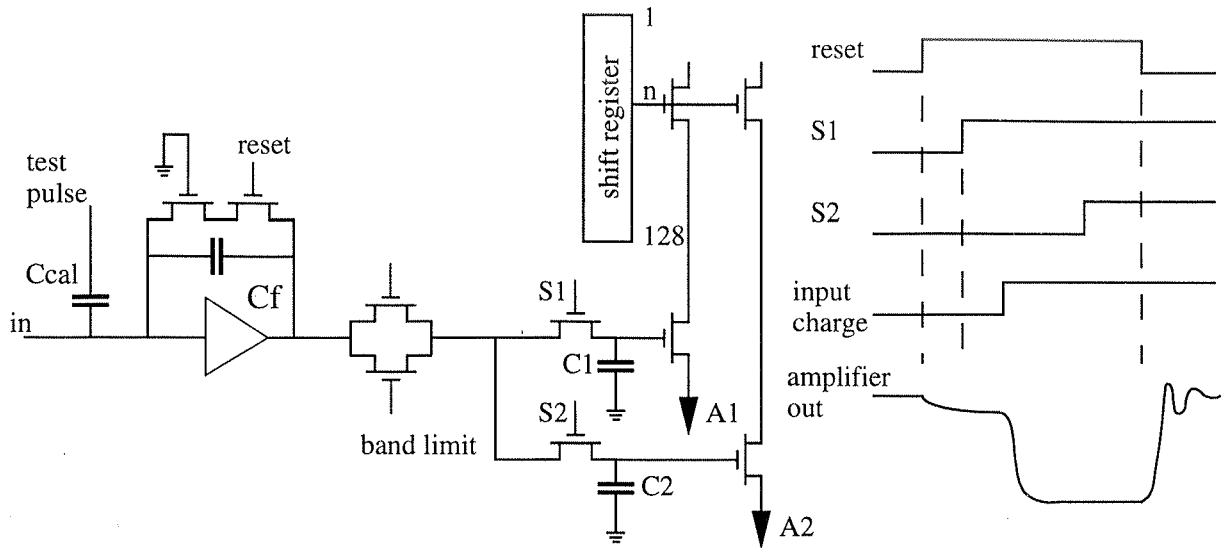


Figure 3.5: Schematic diagram of the analog part for one MX6 channel together with the timing of control signals during the data capture cycle.

and  $C_2$  sample the amplifier output signal simultaneously during this phase. During the time when  $S_1$  is off and  $S_2$  is on, the detector signal is stored only on capacitance  $C_2$ . The signal peaking time on  $C_1$  and  $C_2$  in response to a detector signal is about  $1.8\mu\text{s}$  in our application. It is determined by the rise time of the amplifier output in conjunction with the time constant given by the resistance of the transistors  $S_i$  and the sample capacitor  $C_i$ . Finally  $S_2$  is switched off too at the end the data capture cycle. Therefore  $C_1$  contains the signal before the particle passage and  $C_2$  afterwards. By subtracting the voltages on  $C_1$  and  $C_2$  one yields a voltage proportional to the input charge during the  $S_1$ - $S_2$  interval. Any low frequency noise and level shifts, e.g. from control signals on the chip like the reset, are removed by this double sampling method.

Two important differences to the VIKING design have to be pointed out: firstly the precise time when an interaction happens has to be known in advance in order to start the data capture cycle before the particle traverses the detector. This is no problem at LEP as the precise time of the LEP bunch crossing is known and the cycle can be started prior to the crossing. For other applications where it is impossible to obtain a trigger signal several  $\mu\text{s}$  before particle reach the detector, for example in beam test or in test with sources, this presents a significant problem. Because of this difficulty the VIKING chip was chosen for the tests presented in this chapter. Secondly, the time interval between  $S_1$  and  $S_2$  has to be chosen carefully so as not to lose parts of the signal. During the  $S_1$ - $S_2$  measurement interval the result can be spoiled by high shot noise and transients of the reset signal as they are sampled only on the  $C_2$  capacitor.

After the data capture cycle has ended the voltages stored on the capacitors are time multiplexed to two single output terminals  $A_1$  and  $A_2$  via the control of a shift register. Voltage subtraction  $A_2 - A_1$  is performed later before the resulting voltage is digitised by an ADC, which is in our case a fastbus SIROCCO IV module [28].

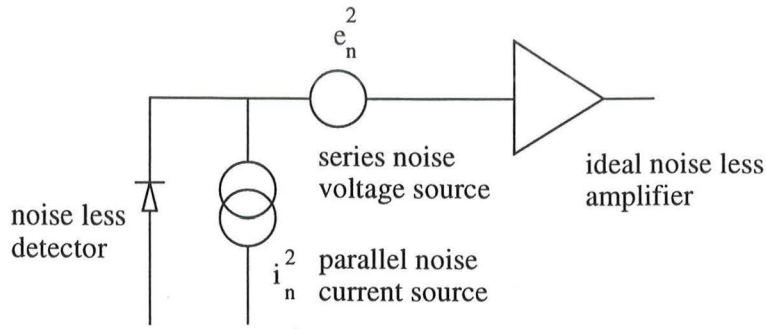


Figure 3.6: Parallel and serial noise sources at the input of an ideal noiseless amplifier.

### Noise in the system detector / electronics

The noise performance of a system is characterized by a quantity referred to as the “Equivalent Noise Charge” (ENC). It is defined as a signal which would generate an output signal of the same amplitude as the r.m.s. noise in the system. It is commonly given in units of electrons as it refers to an input charge. The noise of an amplifier system can be expressed by considering an ideal, noiseless amplifier together with a series voltage noise source and a parallel current noise source on the amplifier input (figure 3.6).

The series noise source originates in the input Field Effect Transistor (MOSFET). Contributing factors to the ENC from the amplifier are the thermal fluctuations of current flowing in the conducting channel of the FET and the bulk resistance, which are inversely proportional to the square root of transconductance and peaking time. They represent white noise sources. The total noise figure depends linearly on the total capacitive load at the input. The total capacity consists of the detector capacitance as well as of the gate capacitance of the transistor as well. Separating gate from detector capacitance yields an amplifier related ENC with a constant term plus a term depending linearly on the detector capacitance.

The parallel noise present at the amplifier input is mainly detector related. Detector leakage current contributes as shot noise, which is sampled on the feedback capacitance just as the signal current, to the parallel noise. Thus, very low levels of leakage current are required for optimum noise performance, demanding good control of the detector production process. Leakage currents in the order of few nA/cm<sup>2</sup> are achieved with modern processes. Another source of parallel noise is the thermal noise from parallel resistors at the input. The resistors through which the detector strips are biased and the feedback resistors are the dominant resistors causing noise, and should be as high as possible. The total system noise is the quadratic sum of all individual contributions given by

$$ENC_{\text{preamplifier}} = a + bC_{\text{det}}[\text{pF}] \quad (3.17)$$

$$ENC_{\text{leakage current}} = \frac{e}{q} \sqrt{\frac{qI_{\text{dl}}T_p}{4}} \quad (3.18)$$

$$\text{ENC}_{\text{parallel resistor}} = \frac{e}{q} \sqrt{\frac{kTT_p}{2R_p}} \quad (3.19)$$

$$\text{ENC}_{\text{total}} = \sqrt{\text{ENC}_{\text{preamp}}^2 + \text{ENC}_{\text{lc}}^2 + \text{ENC}_{\text{pr}}^2} \quad [\text{r.m.s. } e^-] \quad (3.20)$$

where  $C_{det}$  denotes the total detector capacitance present on the amplifier input,  $e$  is 2.718,  $q$  the electron charge,  $I_{dl}$  the detector leakage current for one channel,  $T_p$  the peaking time ( $1.8\mu\text{s}$  in our case),  $k$  the Boltzmann constant,  $T$  the absolute temperature in Kelvin and  $R_p$  the parallel resistance given by the bias resistor and the feedback resistor. For our application with a peaking time of  $1.8\mu\text{s}$  the individual contributions of the ENC in electrons can be estimated to be

$$\text{ENC}_{\text{pa}} = 136 + 12C_{det}[\text{pF}] \quad \text{for the VIKING chip [26]} \quad (3.21)$$

$$\text{ENC}_{\text{pa}} = 325 + 23C_{det}[\text{pF}] \quad \text{for the MX6 chip [29]} \quad (3.22)$$

$$\text{ENC}_{\text{lc}} = 144\sqrt{I_{dl}[\text{nA}]} \quad (3.23)$$

$$\text{ENC}_{\text{pr}} = \frac{1024}{\sqrt{R_p[\text{M}\Omega]}} \quad (3.24)$$

For experiments like DELPHI other sources of noise have to be taken into account additionally. The analog signals pass through several additional voltage amplifiers with their own individual power supplies and 30m of cables until they are finally digitised. Proper shielding and grounding, as well as the choice of power supplies and amplifiers in the signal transfer are essential to reach this theoretical limit.

The choice of MX6 readout electronics for the VFT is strongly influenced by the requirement of compatibility to the existing microvertex electronics. The VFT ministrip system and the barrel detector system are regarded, concerning their readout, as a single detector system.

## 3.2 Charge division in large strip pitch detectors

Silicon strip detectors are commonly used for their excellent position resolution. Still for some applications of silicon detectors in collider experiments no ultimate spatial resolution is required and other items like the total number of electronic channels and construction costs are of high importance. This is the case for detectors at large radius from the beam axis where a big surface has to be covered. In the extreme forward region of collider experiments multiple scattering of the particles in the beam pipe and support structures limits the track reconstruction precision towards the detector and therefore detectors with moderate spatial resolution are sufficient.

One logical solution to reduce the number of readout channels is to increase the strip spacing to few hundredths of micrometers. When a particle traverses such a detector perpendicularly the deposited charge is collected on one strip only. As without prior knowledge the tracks are uniformly distributed across one strip acceptance, i.e. approximately the strip pitch, and the only information available is the position of the strip centre, the position resolution is given by the strip pitch divided by  $\sqrt{12}$ . Only a small fraction of the tracks cross the detector in the mid between two strips where the charge is shared among them and thus charge interpolation can be used for a better position estimate. The following considerations shall illustrate how the position resolution can be improved for a large readout pitch.

### 3.2.1 The role of intermediate strips

To improve the spatial resolution, charge division between strips and analog readout of the signals are desired. The analog signals measured on several strips are used for (offline) position interpolation. Charge division can occur for several reasons:

- diffusion during the charge collection
- inclined tracks where the charge is deposited on several strips
- capacitive (or resistive) charge coupling from strips in between the readout strips.

While the first two effects produce a continuous spectrum of signals on different strips, the latter one may yield constant fractions of strip signals. Measurements carried out in testbeams for this work shall be used to demonstrate the influence of diffusion, capacitive charge division and track inclination on the spatial resolution (sections 3.4 and 4).

While diffusion is present in any detector and track inclination depends on the detector arrangement, the third effect requires a special design of the detector. For detectors with capacitive or resistive charge sharing, additional strip implants are placed between the readout strip implants, leading to a strip pitch smaller than the actual distance between adjacent readout strips. In any further discussion the distance between readout strip centres is referred to as the “readout pitch” and the distance between any two adjacent strips as the “strip pitch”. The so-called “intermediate” strips between readout strips are equally spaced so that a detector with a readout pitch of  $200\mu\text{m}$  and one intermediate strip has a strip pitch of  $100\mu\text{m}$ .

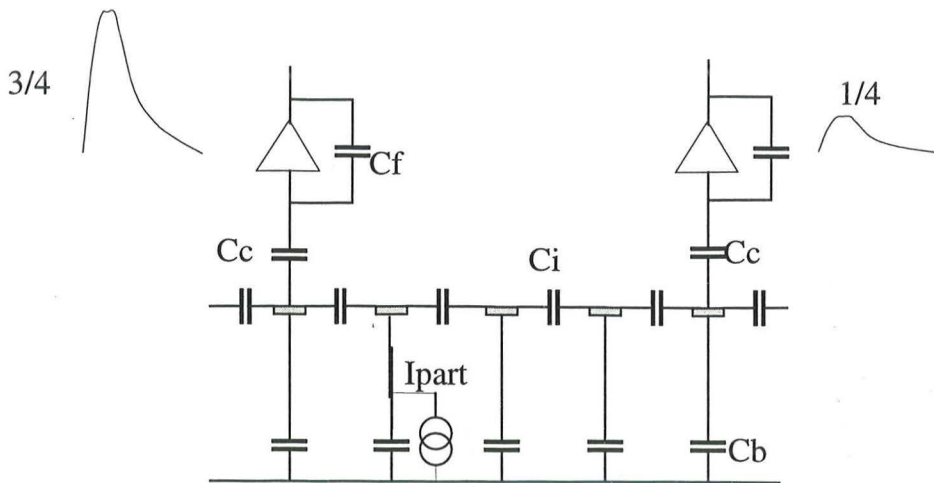


Figure 3.7: Schematic layout of a detector making use of capacitive charge division. The current source represents a particle traversing the detector below an intermediate strip.

In principle two techniques can be used to couple readout and intermediate strips. For a resistive coupling a large resistor has to be implemented between adjacent strips. This is possible but might require additional production steps and space on the silicon detector. Furthermore, this resistor presents a parallel noise source on the charge amplifier input. A capacitive coupling requires no additional technology as it uses the intrinsic capacitance between the strip implants commonly called the "interstrip capacitance".

The idea of capacitive charge division is illustrated in figure 3.7. It shows a sketch of a detector based on capacitive charge division with three intermediate strips. If a particle crosses the detector perpendicular to an intermediate strip, indicated by the current source, the charge is collected on this strip. Image charges with the ratio 3/4 and 1/4 are induced on readout strip 1 and 2 respectively. The ratio of the signals measured on the readout strips depends on the detector geometry as long as the capacitive charge division is the main source of charge sharing. The correlation of the two signals can thus be used to interpolate the hit position between the strips. The signal ratio as a function of the detector layout will be discussed in more detail in section 3.4.

Although capacitive charge division with intermediate strips can improve the resolution, it might lead to incomplete signal collection. Capacitive charge division relies on the fact that the capacitance between strips is an order of magnitude higher than their capacitance to the backplane. This is typically the case for detectors with  $25\mu\text{m}$  strip pitch and a readout pitch of  $50\mu\text{m}$ , commonly used in vertex detectors. To ensure that the full current signal is transferred to the feedback capacitance of the preamplifier one requires a high capacitance, and therefore low impedance, between the strip implant and the amplifier input, as well as a comparably low capacitance to neighbouring strips and backplane. If the signal is deposited below the readout strip the capacitance to the amplifier is given by the coupling capacitance which is much larger than the total capacitance to the backplane and neighbouring strips. Thus the signal is mainly transferred to the feedback capacitance. Differently for hits on intermediate strips: in this case the effective coupling capacitance between implant and amplifier is given by the series connection of

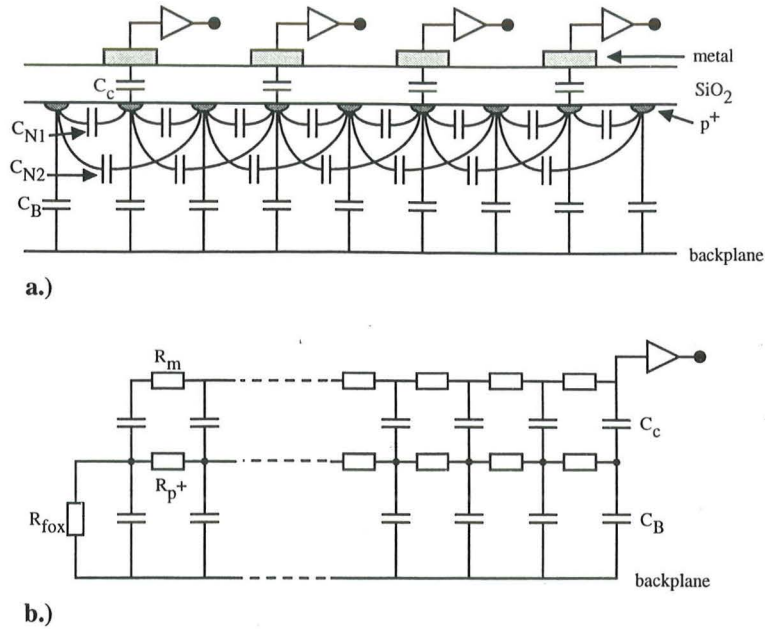


Figure 3.8: Equivalent circuit of the detector used for the SPICE simulation. The top plot shows the model perpendicular to the strips, the central plot represents the model network along the strip. The definition of later measured interstrip and backplane capacitance is given in the bottom plot.

interstrip capacitance and coupling capacitance. As the interstrip capacitance is small and of about the same order of magnitude as the capacitance to the backplane, only a fraction of the signal is transferred to the amplifiers and the other part is lost to the backplane.

This signal loss highly depends on the effective values of interstrip, coupling and backplane capacitance, their ratios and therefore on layout parameters like number of intermediate strips, implant width, strip pitch and readout pitch. With the help of capacitive charge division it is possible to achieve significantly better spatial resolution compared to a detector of the same layout without intermediate strips. The gain of spatial resolution with the use of intermediate strips has to be carefully weighted against the loss of signal to ensure reliable operation of the detector.

### 3.2.2 Simulation of detector signals

In order to understand and estimate the signal loss for hits on intermediate strips a SPICE simulation of the detector/preamplifier system was carried out. The detector is modelled as a lumped network of C and R components for interstrip, backplane and coupling capacitances as well as implant and readout line resistance. The individual components are shown in figure 3.8 across the strips (top) and along the strips (bottom). A detector layout as finally chosen for the VFT ministrip detector with one intermediate strip is simulated. A system with 9 strips is simulated where each 5.2 cm long strip is divided in 126 equal cells. The frontend electronic is modelled by an equivalent network corresponding to the VIKING amplifier.

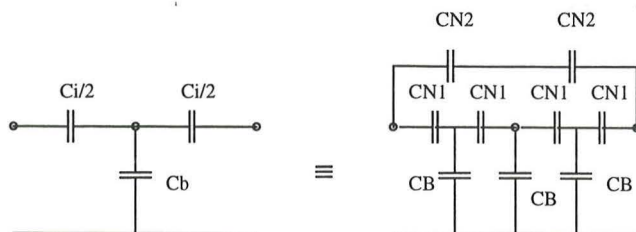


Figure 3.9: Definition of measured interstrip and backplane capacitances  $C_i$  and  $C_b$  in terms of  $C_{N1}$ ,  $C_{N2}$ ,  $C_B$ .

In the simulation  $C_c$  represents the coupling capacitance,  $C_{N1}$  the capacitance to the nearest neighbouring strip,  $C_{N2}$  to the second neighbouring strip,  $C_B$  the capacitance on one strip to the backplane,  $R_p$  the implant resistance,  $R_m$  the metal readout line resistance and  $R_{fox}$  the resistance of the FOXFET strip bias resistor.

The definition of the later measured interstrip capacitance  $C_i$  and backplane capacitance  $C_b$  is given in figure 3.9.  $C_i$  is defined as  $C_i = C_{n1} + 2C_{n2}$ . The backplane capacitance  $C_b$  is given by the capacitance of one readout strip to the backplane. To figure 3.8 it compares approximately like  $C_b \approx 2C_B$  if  $C_{n1}$  is larger than  $C_B$ .

The values chosen for the simulation are taken from measurements on VFT ministrip prototype detectors produced by TESLA Roznov[15]. The detectors are  $5.2 \times 5.2 \text{ cm}^2$  large and feature 504 implant lines at a pitch of  $100 \mu\text{m}$ , one half of them with a width of  $20 \mu\text{m}$  and the other half with  $40 \mu\text{m}$  implant width. Input values for a detector with  $60 \mu\text{m}$  implant width are derived from an extrapolation of the values measured on the 20 and  $40 \mu\text{m}$  configuration. Various models for estimating capacitances from geometrical parameters can be found in the literature [41][40][42].

The aim of the simulation is to study the influence of the ratio implant width to strip pitch on the measurement of the detector signal. Furthermore the layout shall be optimized with respect to the signal to noise performance. Keeping the number of intermediate strips constant, the ratio of implant width to strip pitch can be used to tune the interstrip capacitance to the optimum value. The interstrip capacitance depends roughly linearly on this ratio as can be seen in figure 3.10 [30]. Variations in the offset may occur due to different production processes used by different manufactures. Our measurements for the TESLA VFT prototypes are superimposed as solid markers.

In the simulation the response of a detector with a ratio of 0.2, 0.4 and 0.6 is studied. The amount of lost signal is estimated by considering two different cases: in the first case a current signal, corresponding in size and time behaviour to a minimum ionising

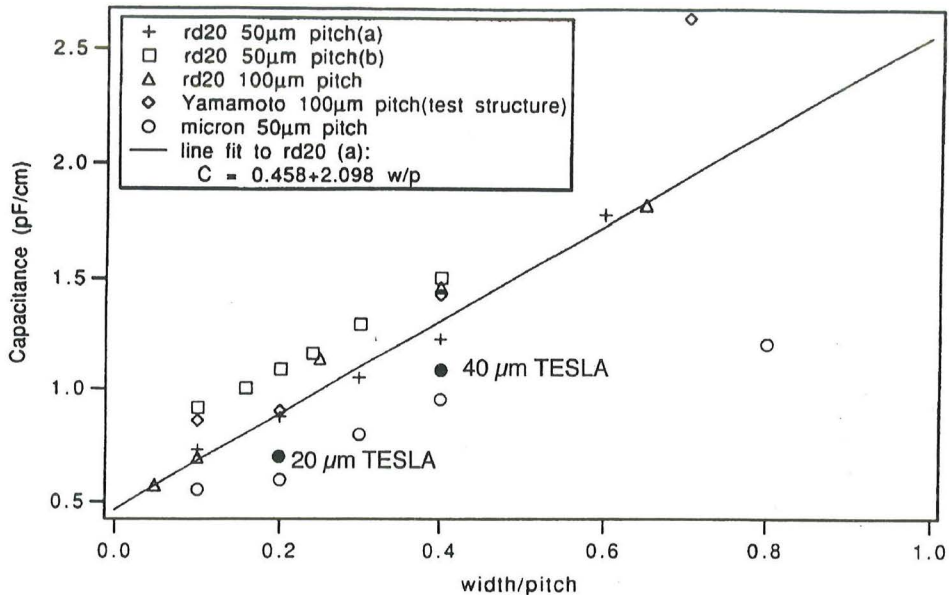


Figure 3.10: Correlation between interstrip capacitance and ratio implant width to pitch from measurements on different structures [30]. The full markers give the values measured for the TESLA VFT prototypes with 20 and 40µm implant width.

Implant width	20µm	40µm	60µm
simulation	0.64	0.72	0.75
testbeam	0.58	0.64	0.76

Table 3.1: The ratio of simulated total signal for hits on intermediate strip to hits on readout strips in comparison to testbeam measurements of the three configuration. For the testbeam value the ratio of the most probable value of the two distributions is given

particle, is placed below a readout strip. The maximum voltage output of the simulated shaper is taken as a measure of the expected signal. In the second case, where the same current signal is placed below an intermediate strip, the shaper output on the two adjacent readout strips is observed. In the latter case the sum of the two shaper outputs gives the signal expected for hits below the intermediate strips. Figure 3.11a shows the output of one shaper as measured for the two cases, figure 3.11b presents the same quantity for hits on the intermediate strip as it is expected for the three different configurations. It clearly indicates the decreasing loss with wider strips. At wider strips, the signal transfer to the amplifier is improved by the increased interstrip capacitance at constant backplane capacitance.

Extensive tests were carried out on TESLA VFT prototypes to cross check the simulation results and study the layout of the VFT detector. A summary of the test results on prototype detectors can be found in reference [16].

The total cluster signal simulated is compared to testbeam measurements in table 3.1, which gives the ratio of the most probable cluster signals for intermediate strip hits to



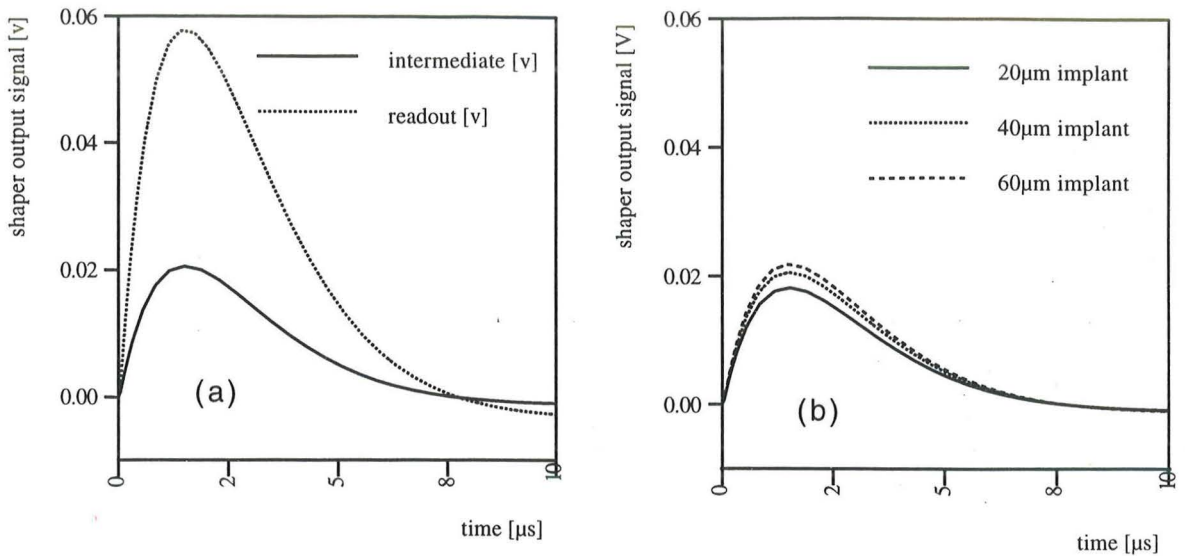


Figure 3.11: Simulated output of one shaper for hits on the readout strip and on the intermediate strip in the  $40\mu\text{m}$  configuration (a) and a comparison of the single shaper output for hits on the intermediate strip in the 20, 40 and  $60\mu\text{m}$  configuration (b). For hits on the intermediate the total signal is twice the signal shown here.

readout strip hits in the three configurations. The testbeam data are taken from TESLA VFT prototypes in the 20 and  $40\mu\text{m}$  layout and from the final MICRON VFT detector in the case of  $60\mu\text{m}$ . In the  $60\mu\text{m}$  configuration a signal ratio of 76% can be expected for hits on the intermediate strip compared to hits on the readout strip <sup>1</sup>.

The higher interstrip capacitance improves the signal measurement but also increases the noise due to the higher capacitive load on the amplifier input. It is possible to evaluate the noise performance of the configuration by using a full equivalent network for the detector which takes into account effects like capacitive load on the amplifier and thermal noise generated by the resistance of implant, metal line and bias resistor. Both, the better signal collection and signal to noise performance on intermediate strip hits favours the  $60\mu\text{m}$  layout, which was later chosen for the final detector.

<sup>1</sup>the test results for the VFT detector will be presented in chapter 4

### 3.3 Treatment of raw data in the analysis program

In this section an overview of the analysis program shall be given. This program was used for the analysis of the testbeam data and the corresponding algorithm is now a permanent part of the DELPHI analysis program DELANA. It focuses on the signal calculation starting from the raw data. A definition of terms used in the analysis like signal, noise and cluster shall be given here.

#### 3.3.1 Definitions of terms

As "raw data" is considered the voltage output of the frontend chip for each channel as it is digitised by the ADC for each event. During the readout cycle the voltages of all channels are consecutively digitised as they appear on the single analog output node of each chip. If several chips are read out, their readout is chained together, i.e. the first channel of the second chip follows the last channel of the first chip. The digitization has to be completed for all chips before the next event can be recorded. The ADC value of each channel is stored temporarily in an on-board memory of the readout electronics and later gathered into a file or processed by a digital signal processor (DSP). Figure 3.12a presents the raw data for one event. The horizontal axis gives the channel number, the vertical axis displays the ADC value measured for each channel. The measured ADC value is a convolute of several contributions: It contains the actual signal from a particle traversing, a DC voltage offset of the channel, referred to as "pedestal", the channel noise and a random shift of all voltages on one chip called "common mode shift" (CMS). In the following discussion index  $i$  denotes the strip number and  $k$  the event.

$$ADC_i(k) = S_i^{part}(k) + S_i^{noise}(k) + P_i + CMS(k) \quad (3.25)$$

$S_i^{part}$  stands for the Landau distributed particle signal.  $S_i^{noise}$  is the random noise contribution for each channel. It is gaussian distributed with mean zero. Its variance corresponds to the ENC<sup>2</sup> described before.  $S_i^{noise}$  is roughly independent of the neighbouring channel noise, uncorrelated between events and cannot be deconvoluted from the particle signal. Its frequency spectrum is not uniform, i.e. it is no white noise, as it is the output of band pass filters. In the analysis the r.m.s.  $N_i$  of its distribution is calculated for each channel and later used for finding particle hits.  $N_i$  is in general rather uniform within one chip, but some channels still can have a higher noise due to defect channels in the frontend chip or detector faults.

The pedestal  $P_i$  corresponds to a DC offset of the channel output voltage. It has contributions from the chip, where channel to channel variations can occur, and from the detector in case any DC current flows into the amplifier. Pickup on amplifier inputs, that may for example come from transients of control signals, can alter the pedestal. This offset has to be calculated for each channel as large deviations between the channels can occur. It might also vary slowly with time as a result of temperature changes or changes of power supply voltages. For correct signal calculation this time variation is monitored and has to be taken into account.

In addition to signal and noise, all channel voltages of one chip can be shifted by a positive or negative amplitude. This amplitude is equal for all channels of one chip and

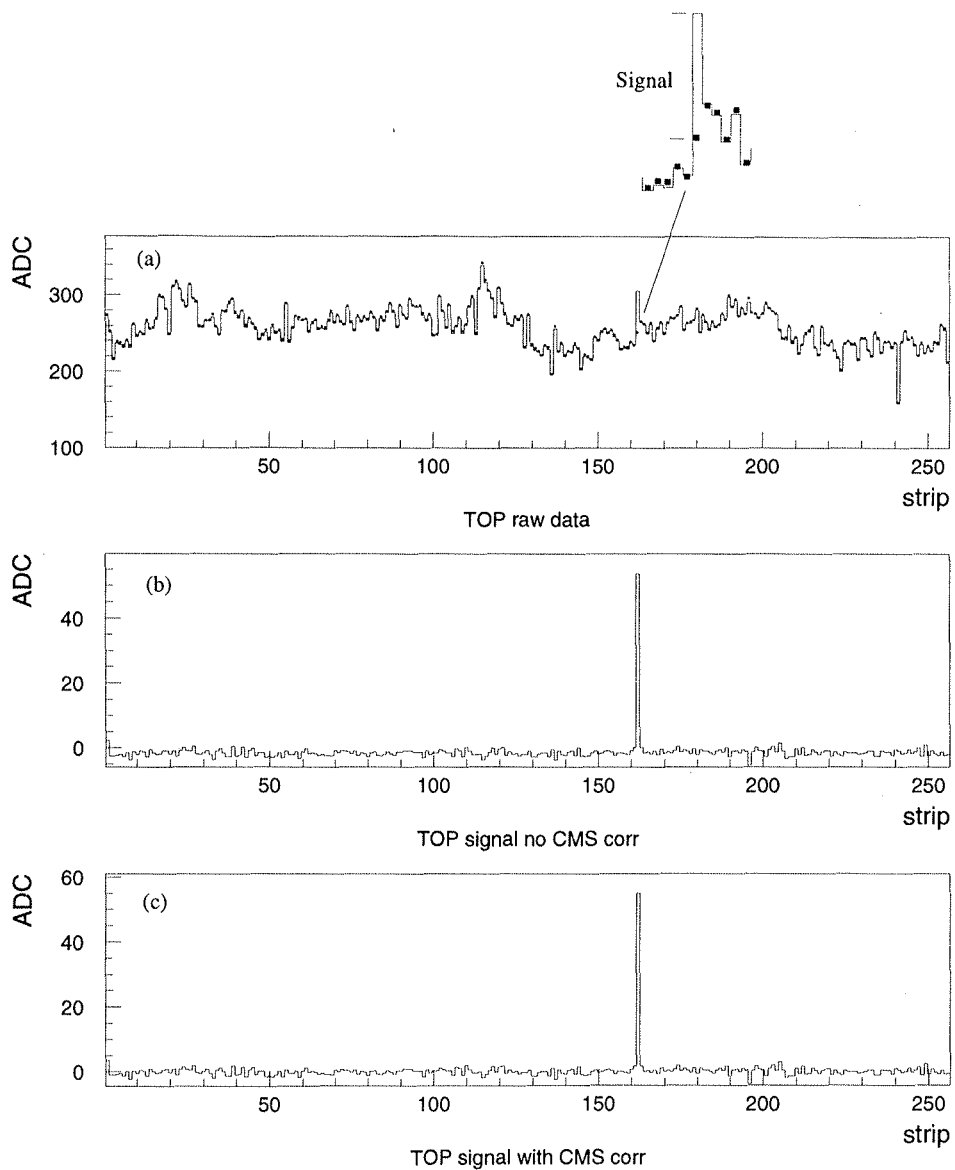


Figure 3.12: Figure (a) displays the raw data (line) for 256 strip for one event taken with a final VFT detector module. The calculated pedestal is superimposed as markers. Figure (b) and (c) show the raw data corrected for the pedestal and the final signal for all channels after CMS correction.

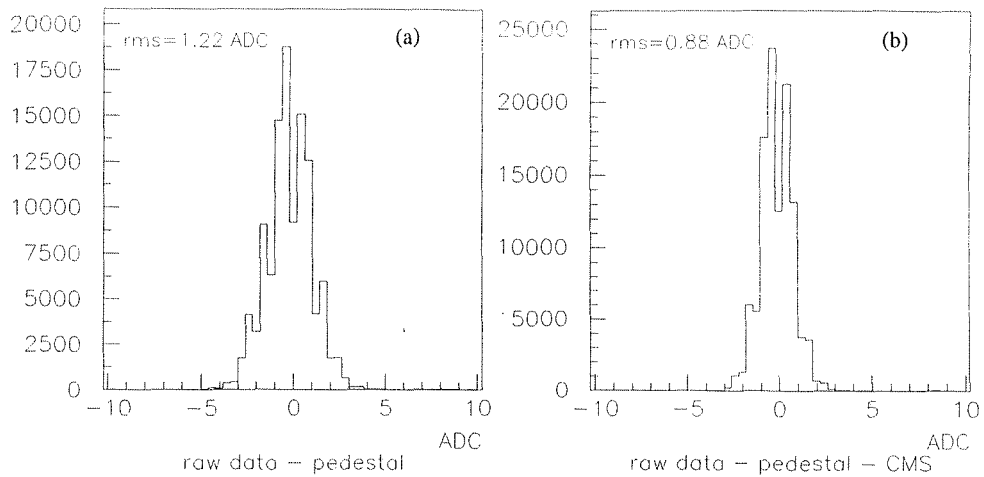


Figure 3.13: The noise distribution before CMS correction is displayed in figure (a), while figure (b) shows the same distribution after CMS correction. The signal calculation on the DSP is done with a precision of 0.25 ADC, which is responsible for the binning effect.

therefore can easily be calculated and corrected for. The CMS is uncorrelated between events and obeys in our case a gaussian distribution. The r.m.s. of the CMS distribution adds quadratically to the channel noise  $N_i$ . Figure 3.12b shows the raw data after pedestal correction but before the CMS is corrected for this particular event, a slight shift of the baseline is visible. In figure 3.12c the CMS is also subtracted. This results in a sequence of signals where the particle hit can easily be identified. The data for these histograms are taken from testbeam measurements with final VFT ministrip detector modules. Figure 3.13 shows the noise distribution before CMS correction, i.e. the distribution of  $S_i^{noise}(k) + CMS(k)$ , and after CMS correction. The change in the distributions r.m.s. points out the relevance of this correction.

Figure 3.14 presents the logical sequence of the signal calculation as a flow chart.

### 3.3.2 Signal calculation

#### The initialisation

To obtain starting values of pedestal  $P_i$  and noise  $N_i$  an initialisation is performed at the beginning of each data-taking period. The first  $n$  events collected, typically 10 to 100 are used for the pedestal initialisation. The ADC values are histogrammed for each channel over  $n$  events; the most probable ADC value, i.e. the value where the resulting distribution peaks, gives for each channel the desired starting value for the pedestal. As particle hits can be present in the sample, taking the peak value gives a better estimate of the pedestal than simply taking the average ADC value. A second sequence of  $n$  events is used for calculating the noise for each channel. The raw data of all channels are corrected for their pedestals  $A_i(k) = ADC_i(k) - P_i$ , with  $k$  denoting the event number. The resulting values are averaged for each chip. Saturated or dead channels are excluded from the average. Furthermore, all channels with  $A_i > 3\bar{N}$  are excluded from the average.

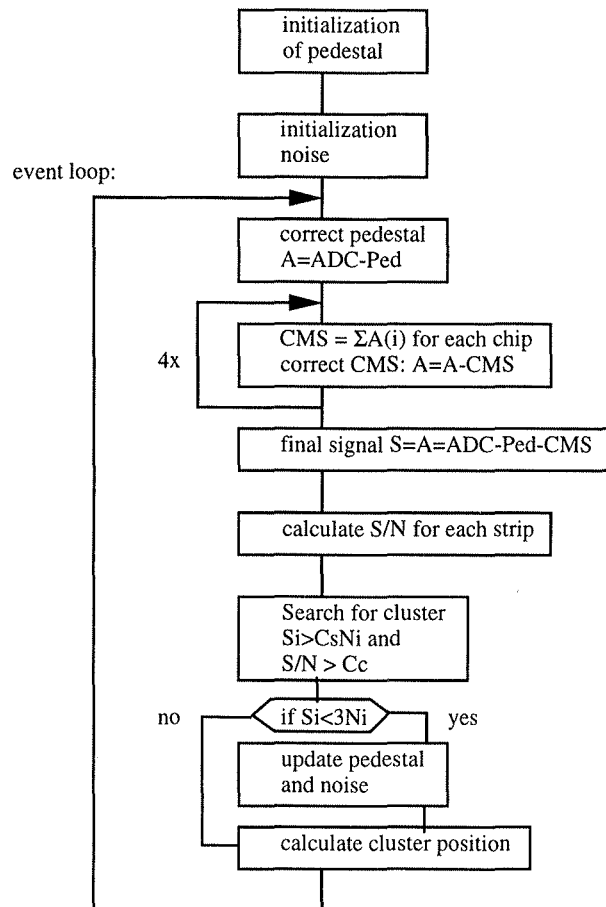


Figure 3.14: Flow chart illustrating the signal calculation (see text).

$\bar{N}$  is the average chip noise, defined as the r.m.s. of the signals  $S_i$  of one chip.

$$\bar{A}(k) = \frac{1}{128} \sum_{i=1}^{128} A_i(k)$$

$$\bar{N} = \sqrt{\frac{1}{128} \sum_{i=1}^{128} (A_i(k) - \bar{A}(k))^2} \quad (3.26)$$

The average over  $A_i$  is a measure for the CMS, which is corrected on all strip signals as  $S_i(k) = A_i(k) - CMS(k)$ . After the completion of this sequence for  $n$  events the noise is calculated as the r.m.s of the signal recorded for each strip with

$$N_i = \sqrt{\frac{1}{n-1} \sum_{k=n+1}^{2n} S_i^2(k)} \quad (3.27)$$

$N_i$  is stored for each channel and later used in the cluster finding.

### The event loop

The event loop follows basically the same strategy as the initialisation though the CMS correction is done in iterations. For each strip the raw data are corrected by the pedestal value  $A_i(k) = ADC_i(k) - P_i$ . Then, the average signal for each chip is calculated yielding the CMS correction.

$$CMS(k) = \frac{1}{128} \sum_{i=1}^{128} A_i(k) \quad (3.28)$$

Dead or saturated strips as well as strips with  $A_i > 3N_i$  are excluded from the average calculation. After all signals have been updated by  $S_i(k) = A_i(k) - CMS(k)$  the procedure is repeated, as illustrated in figure 3.14, with replacing  $A_i$  in equation (3.28) by  $S_i$ . Two iterations are typically needed to achieve a precise value for the CMS correction. In case the signal calculation is carried out by a DSP the maximum precision is 1/4 ADC count in our case as no additional precision is needed. This is also the reason for the binning effect in figure 3.13.

Two thresholds are used to identify clusters: The threshold  $C_s$  on the single strip signal ( $S_i > C_s N_i$ ), and a threshold on the total cluster signal  $C_c$ .  $C_s$  and  $C_c$  are multiple of the single strip r.m.s. noise. Thus the identification of clusters not only depends on the signal but rather on the signal to noise ratio.

In order to search for clusters on the detector, the single strip signal to noise ratio  $S_i/N_i$  is calculated for each strip and compared to a constant threshold  $C_s$ . The cluster is defined as a series of adjacent readout strips whose signal to noise ratio  $S_i/N_i$  exceeds this threshold. For later analysis each cluster is described by different parameters. The "cluster signal to noise ratio" is defined as the sum of the single strip signal to noise ratios for all the strips exceeding the threshold.

$$S/N = \sum_i S_i/N_i \quad \text{if } S_i/N_i > C_s \quad (3.29)$$

The "cluster width" corresponds to the number of strips in the cluster, while the cluster signal is the sum of the single strip signals.

$$S = \sum_i S_i \quad \text{if } S_i/N_i > C_s \quad (3.30)$$

Using the single strip signals the hit position can be estimated. To be accepted for further analysis the cluster has to fulfil additional requirements:

- it must not contain noisy strips, i.e. strip with a noise  $N_i > 5\bar{N}$
- the cluster signal to noise ratio  $S/N$  has to be higher than the cluster threshold  $C_c$

Finally the signal calculation is concluded by an update for the strip pedestal and noise. The aim of the pedestal update is to trace slow changes of the channels DC level, that would otherwise lead to "ghost" clusters. A sudden change of noise levels on individual strips would lead also to spurious clusters. These pedestal changes have to be traced for efficient cluster search. The updating of noise and pedestal is done on an event by event basis for all the strips not contained in clusters,

$$P_i(k) = P_i(k-1) + \frac{S_i(k)}{w_1} \quad (3.31)$$

$$N_i(k) = N_i(k-1) + \frac{S_i^2(k)}{w_2} \quad (3.32)$$

The updating actually corresponds to a digital low pass filtering that responds to low frequency motions of pedestal and noise. Particle signals are not influenced by the algorithm, as strips with  $S_i > 3N_i$  are not updated. Small drift of the pedestal are traced by updating the pedestal with a fraction of the signal. The parameters  $w_1$  and  $w_2$  determine the number of events needed to react on shifts.

As stated above, the cluster search is based on the application of two thresholds  $C_s$  and  $C_c$ .  $C_s$  determines the cluster width and will cut on signal tails, thus reducing the signal, if chosen too high. The cluster threshold  $C_c$  influences the efficiency and number of "ghost" hits. If its value is too high it will cut off the lower edge of the signal distribution and therefore lead to inefficiency. On the contrary, if an extremely low value is chosen, noise fluctuations can be recognised as a cluster leading to fake clusters. Both parameters have to be optimized in the final detector system for maximum efficiency at a minimum number of ghosts.

Finally the track position on the detector can be calculated from the single strip signals contained in the cluster by a simple centre of gravity method as

$$x = \frac{\sum_i S_i x_i}{\sum_i S_i} \quad (3.33)$$

where  $x_i$  are the positions of the strip centres on the detector. The algorithm chosen for the position reconstruction will change with the application and layout of the detector. The algorithm used may depend on parameters as readout pitch and track inclination. A comparison of different algorithms can be found in reference [31]. A more refined method giving better results in the testbeam measurements shall be discussed in detail in the following sections.

## 3.4 Performance evaluation of different detector geometries

In this section the results of a performance evaluation of different detector geometries shall be given. The influence of layout parameters like number of intermediate strips and implant width on the signal measurement, noise performance and spatial resolution is studied. This study is meant as a guide line for choosing the optimal layout of the DELPHI VFT ministrip detector.

Furthermore the results obtained during these tests may prove useful in the design of large strip pitch silicon detectors at the future LHC experiments. In both experiments, ATLAS and CMS, large areas in barrel and forward region have to be covered with silicon detectors. As many problems like construction costs, power dissipation and thermal management scale directly with the number of channels, a detector with large readout pitch may help in solving these problems.

### 3.4.1 Layout of evaluated detectors

The detectors under test follow the layout requirement for the VFT ministrip detector, i.e. they are single-sided strip detectors with a readout pitch of  $200\mu\text{m}$ . The detectors were fabricated by MICRON Semiconductor Ltd., CSEM Neuchatel and TESLA Roznow. All detectors under test are AC coupled single-sided test structures using the FOXFET technique to bias the strips. The bias voltage of 60V was chosen to exceed the full depletion voltage by 5V during the tests.

The tested detectors are described in figure 3.15. The CSEM detector has 10mm long strips and features seven different layouts (see table 3.2). Each layout group has 11 readout strips. The TESLA detector has an active area of  $50\times 50\text{mm}^2$  carrying 504 strip implants, each 50mm long, at a pitch of  $100\mu\text{m}$ . The detector is separated in two areas: one with a strip implant width of  $20\mu\text{m}$ , the other with a strip implant width of  $40\mu\text{m}$ . The MICRON detector is 20mm long and has in total 48 readout strips.

In total 11 different layouts are tested which are reviewed in table 3.2. Logically they can be split in 4 groups:

1. In the first two groups, CSEM nool 1 and 2<sup>2</sup> with their measured interstrip and backplane capacitance (see text)) no intermediate strip is present. The implant width is 100 and  $150\mu\text{m}$  respectively.
2. In the second group (CSEM nool 3 and 4, Tesla 1 and 2, MIC nool) all detectors have one intermediate strip between the readout strips. The implant width is varied as 20, 40, 50, 60 and  $70\mu\text{m}$ .
3. The detector in the third group (CSEM nool 5) has three intermediate strips at a strip pitch of  $50\mu\text{m}$ .
4. The fourth group contains detector where the interstrip capacitance is enhanced by a metal layer on top of the implants. The MIC wiol detector is an exact copy

---

<sup>2</sup>nool ... no overlapping metal; wiol ... with overlapping metal



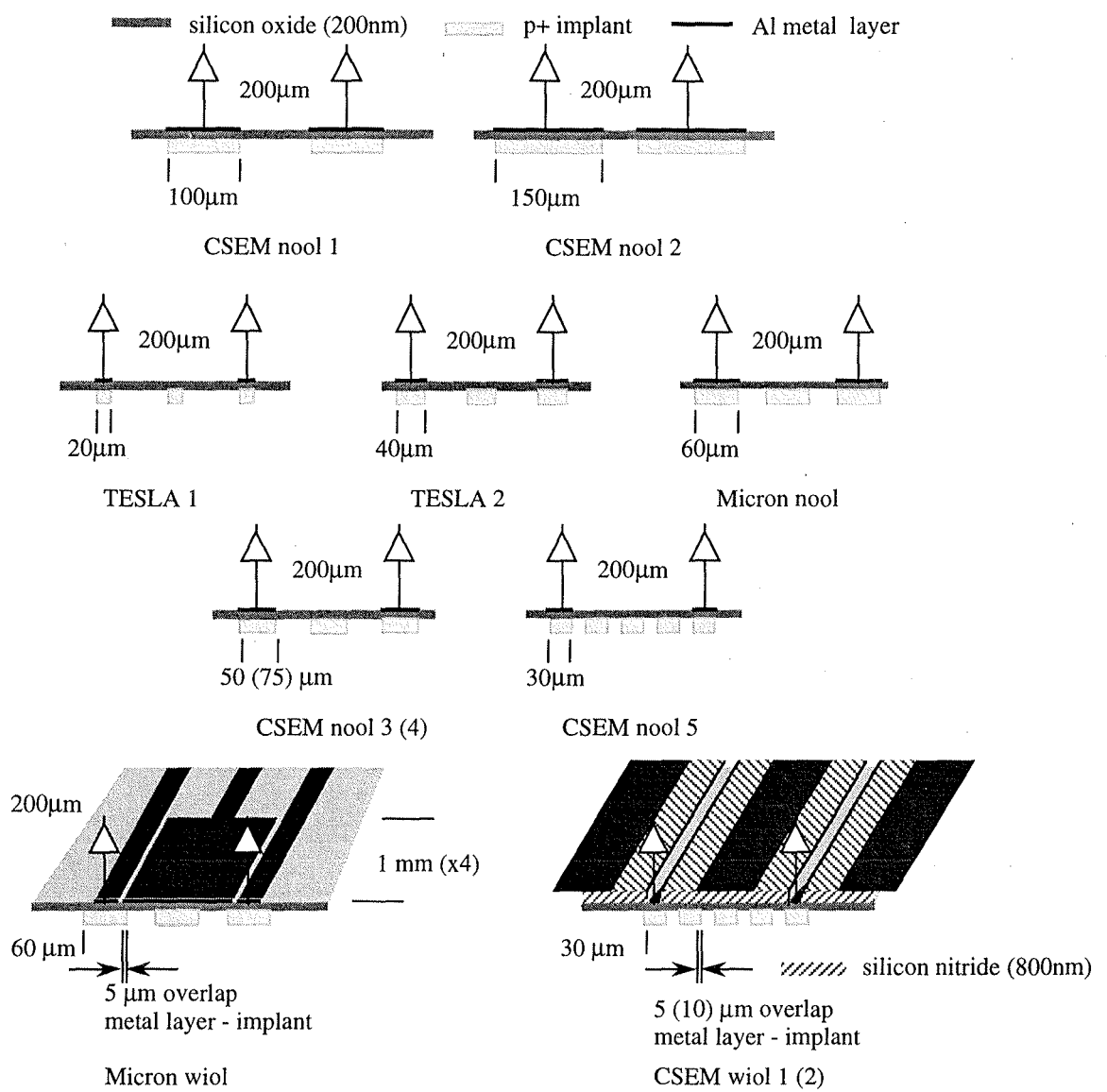


Figure 3.15: Schematic layout of the detectors used for the tests.

of the MIC nool detector apart from the fact, that a metal layer is deposited on top of the intermediate strip. This metal layer overlaps the implant of the readout line by  $5\mu\text{m}$  in width over a length of 1mm. The overlap is repeated 4 times over the strip length of 2cm. The metal layer is separated from the implant by 200nm of silicon dioxide. The CSEM detectors CSEM wiol 1 and 2 also feature a metal layer over the intermediate strips. The latter detectors are copies of CSEM nool 5, i.e. they incorporate 3 intermediate strips. The metal layer overlaps the central intermediate strip entirely and the implant of the neighbouring implants by  $5\mu\text{m}$  ( $10\mu\text{m}$ ) in width. The overlapping metal covers the entire implant length of 10mm, it is separated from the implant by one layer of 200nm silicon dioxide and 800nm of silicon nitride.

The configuration “MIC nool” was later chosen as the final configuration for the VFT ministrip detector.

Table 3.2 presents the measure values of interstrip ( $C_i$ ) and backplane capacitance ( $C_b$ ) according to the definitions in figure 3.8. The interstrip capacitance is given as measured between one readout strip and its two adjacent readout strips. The second neighbouring readout strips are grounded during the measurement of the interstrip capacitance. On the right side the backplane capacitance as measured between one readout strip and the backplane is listed. The adjacent readout lines are kept on ground. The total load capacitance present on the amplifier input is the sum of  $C_b$  and  $C_i$ , as the next connection to ground seen by the amplifier are the two adjacent amplifiers and the backplane. Furthermore the coupling capacitance as measured across the coupling oxide is given.

The measurement of backplane and interstrip capacitance [34] was carried out with a LCR Meter HP4285A sourcing and probing a 100kHz signal at an amplitude of 0.1V on the metal readout lines. During the measurement the backplane was kept on fixed potential corresponding to the full depletion voltage. The coupling capacitance is measured with a Keithley Quasistatic CV meter K595.

### 3.4.2 Testbeam setup

For this study dedicate beam tests are carried out at the CERN SPS accelerator. The detectors are exposed to 80 GeV/c pions traversing the test detector perpendicular to the detector plane. To allow precise determination of the particle impact point on the test detectors, the track is measured by a reference system of silicon detectors. The reference system consists of four high resolution silicon planes, each with  $20\times 20\text{mm}^2$  [35]. Each plane measures two orthogonal coordinates, called  $x$  and  $y$  reference planes, by means of two single-sided strip detectors mounted close to each other with perpendicular strip orientation. The single-sided AC coupled strip detector has a readout pitch of  $50\mu\text{m}$  with one intermediate strip, strip biasing is done using the FOXFET technique. Each single-sided detector carries three VIKING chips for analog signal readout. The readout of the reference and test detectors is done by a VME system based on SIROCCO modules. For the detector tests two reference planes were placed beam upstream and two others beam downstream of the test detectors as illustrated in figure 3.16. The distance between reference plane 1 and 2, as well as 3 and 4 is 8.4mm, reference plane 3 is separated from reference plane 1 by 300mm. The test detectors are placed at  $z = 170\text{mm}$  and  $z = 180\text{mm}$ .

Acronym	$w$ [ $\mu\text{m}$ ]	$n$	$o$ [ $\mu\text{m}$ ]	$l/t$ [ $10^4$ ]	$C_i$ [pF/cm]	$C_b$ [pF/cm]	$C_c$ [pF/cm]
CSEM nool 1	100	0	-	-	1.34	0.72	115
CSEM nool 2	150	0	-	-	1.92	0.76	176
Tesla 1	20	1	-	-	0.40	0.68	30
Tesla 2	40	1	-	-	0.58	0.68	54
CSEM nool 3	50	1	-	-	0.75	0.70	60
MIC nool	60	1	-	-	0.77	0.69	77
CSEM nool 4	75	1	-	-	0.92	0.72	87
CSEM nool 5	30	3	-	-	0.51	0.86	36
MIC wiol	60	1	5	1.	1.79	0.70	44
CSEM wiol 1	30	3	5	1.	1.78	0.94	50
CSEM wiol 2	30	3	10	1.	2.72	0.96	53

Table 3.2: Layout parameters of the detectors under test. The readout pitch is constant with  $200\mu\text{m}$  for all detectors.  $w$  denotes the implant width,  $n$  the number of intermediate strips between two readout strips. In case there is an additional metal layer on the intermediate strips the width of the overlap is denoted by  $o$ , while  $l/t$  describes the ratio of overlap length per cm strip length to insulation thickness

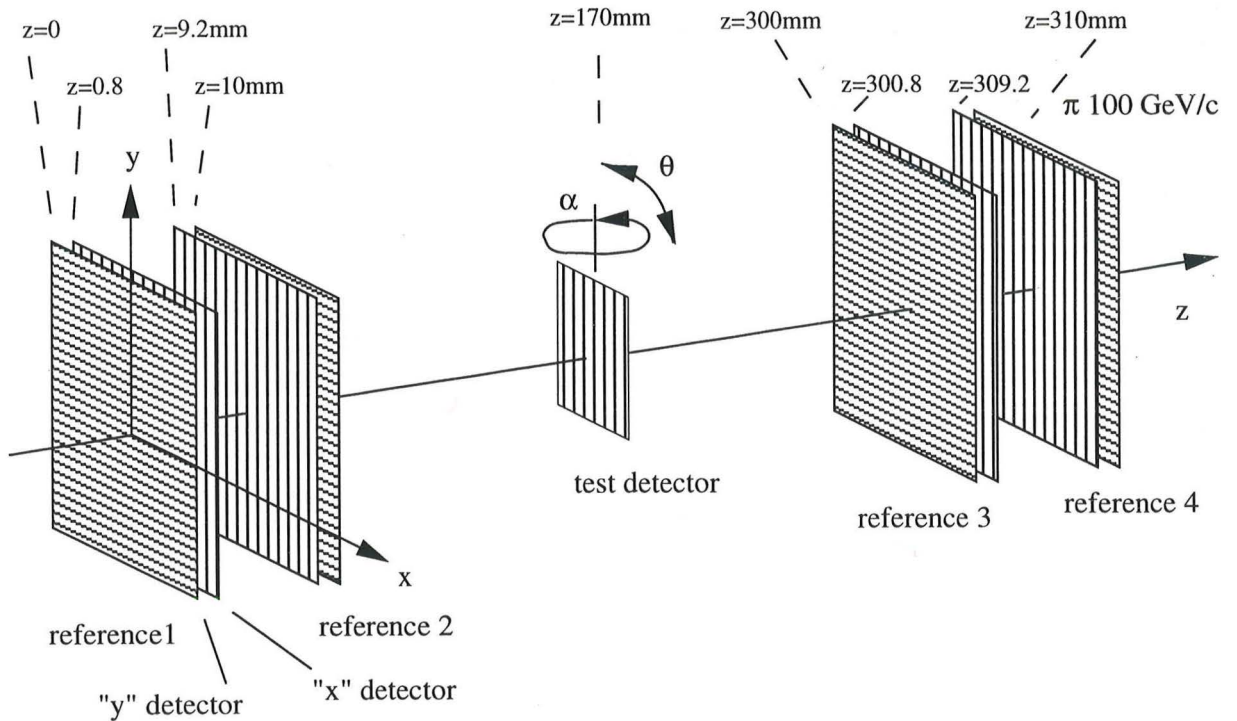


Figure 3.16: Schematic layout of the reference system used for track reconstruction and detector tests.

At the beginning of the analysis, events allowing full track reconstruction both in the  $xz$  and  $yz$  plane are selected, by requiring exactly one hit in both coordinates of each reference plane. This requirement excludes events with more than one track from the analysis. Using these four measurements of  $x(z)$  and  $y(z)$  the track is reconstructed as a straight line by a least square fit. Each single-sided detector of reference plane 2,3 and 4 is aligned with respect to its corresponding detector in reference plane 1. Shifts of the detectors along the measured coordinate as well as rotation of the detector around the beam axis and rotation around their strip axis are corrected.

Due to the precise mechanical construction and the special emphasis on low noise performance the telescope achieves excellent performance in terms of S/N and spatial resolution. As figure 3.17 illustrates a most probable signal to noise ratio greater than 100 can be achieved. The intrinsic spatial resolution of each plane can simply be estimated by plotting the difference of the measured coordinates  $x_2 - x_1$  or  $x_4 - x_3$ . In the reference detector with a strip pitch of  $25\mu\text{m}$  the charge division between strips is dominated by diffusion. Therefore charge interpolation can yield better resolution than the statistical resolution of  $25\mu/\sqrt{12}$ . The measurements of the track in the four planes are uncorrelated, so no covariance terms between  $x_1$  and  $x_2$  is present in the error propagation of  $x_2 - x_1$ . Furthermore the same intrinsic resolution is assumed for all reference detectors The resolution is given by the width of the distribution and the variance of the beam divergency

$\gamma$

$$\begin{aligned}\sigma_{div}^2 &= \text{var}(\gamma)(z_2 - z_1)^2 = (0.48\text{mrad})^2(8.4\text{mm})^2 \\ \sigma_i^2 &= \frac{\sigma_{2-1}^2}{2} - \sigma_{div}^2\end{aligned}\quad (3.34)$$

This yields an intrinsic plane resolution of  $1.3\mu\text{m}$ . By the combination of all 4 planes in the track reconstruction, the impact point on the test detector plane can be given with a precision of  $1\mu\text{m}$ .

### 3.4.3 Signal measurements with different detector geometries

As described in section (3.2) layout parameters like implant width and the presence of intermediate strips determine the signal response. They influence the signal sharing between readout strips and determine eventual signal loss to the backplane.

Two different approaches were chosen to investigate the signal response for the different configurations: the single readout strip signal is observed versus the track position; the entire cluster signal is investigated versus the hit position.

To analyse the response of a single readout strip, the track reconstruction is used to predict the hit position on the test detector. The single readout strip signal  $S(x)$  in response to a track at a given distance to its strip centre  $x$  is observed. No restrictions are imposed on the detector signal in the analysis. It is required that the predicted hit position is in the detector acceptance and not on a dead or noisy strip. The gain variations between different channels are below 3% and are not corrected.

To analyse the total cluster signal  $S_{cl}(x)$  as a function of the hit position a cluster search as described in section (3.3) is performed on the test detectors. The measurement of  $S_{cl}(x)$  allows the precise determination of the region where a fraction of the signal is

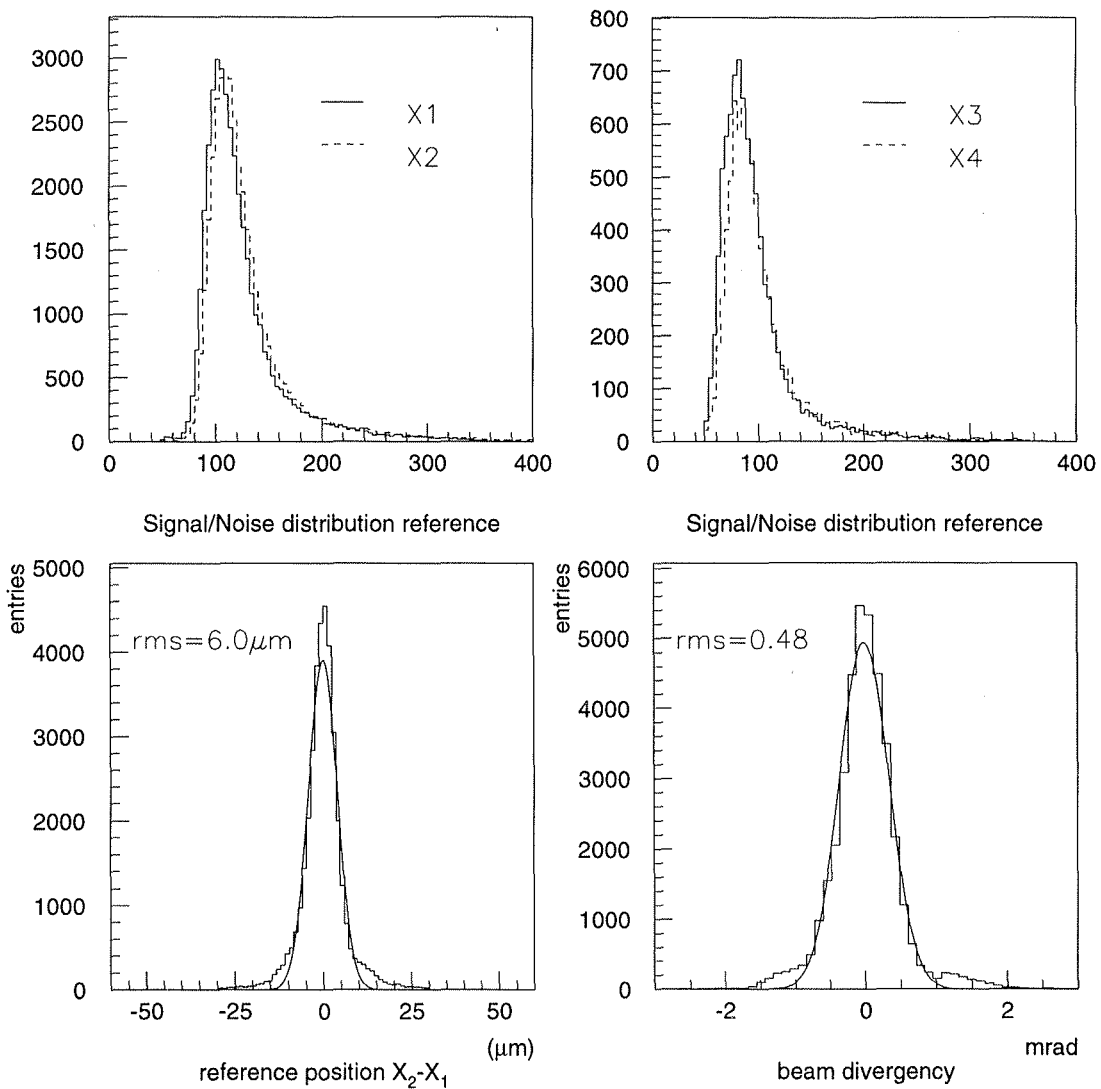


Figure 3.17: The top figures show the S/N performance for reference planes  $x_1$  to  $x_4$ , the bottom ones illustrate the difference of measured hit positions in plane  $x_2$  and  $x_1$  and the measured beam divergence.

lost. A single strip threshold  $C_s = 2.5$  is used for the determination of the cluster strips, the total cluster S/N is required to be higher than  $C_c = 6$ . Only events with exactly one cluster on the test detector are accepted.

Figure 3.18a illustrates the correlation between the readout strip signals left and right of the predicted hit position for a detector without intermediate strips (CSEM nool 1). It clearly indicates that for most events the signal is collected on one of the two strips only. Plot b shows the average readout strip signal  $S(x)$  in dependence of the hit position in the detector plane. The strip signal remains constant over the entire acceptance region of the strip. For perpendicular tracks this results in a digital behaviour of the detector, where the hit position is given by the strip position and no further information is available to improve the position reconstruction precision. The signal on neighbouring strips is given by  $S(x \pm 200)$ . The narrow tail of  $S(x)$  below  $x = -100\mu\text{m}$  and above  $x = 100\mu\text{m}$  indicates an interface region between the strips where charge is shared between two neighbouring implant due to diffusion. The bottom plot shows the dependence of the cluster signal with respect to the hit position between two readout strip centres. The average cluster signal is normalised to the cluster signal measured in a region of  $20\mu\text{m}$  around the readout strip centre. No significant difference between an implant width of  $100\mu\text{m}$  (CSEM nool 1) and  $150\mu\text{m}$  (CSEM nool 2) is observed. The signal collection efficiency appears to be constant throughout the entire region for both detectors.

The same set of illustrations in figure 3.19 describe the behaviour of detectors with one intermediate strip. In plot (a) three distinct regions are visible. In two of them, only one strip carries the entire signal as in the case of no intermediate strips. In the third region both readout strips left and right of the predicted position measure the same amplitude. Plot b shows that the latter region results from hits in the acceptance of the intermediate strip  $x = 50\mu\text{m}$  to  $x = 150\mu\text{m}$ . Below readout and intermediate strips the signal response remains constant and allows no further interpolation within its acceptance area. The signal amplitude for hits on the intermediate strip does not correspond to 50% of the amplitude for hits on the readout strip. For these detectors the signal loss due to their interstrip to backplane capacitance ratio amounts to 15-20% of the charge measured on directly read out strips. The charge loss is precisely restricted to the intermediate strip.

The fraction of signal on intermediate to readout strip can be estimated from the capacitive division of the signal between the amplifier and the backplane capacitance as it is illustrated in figure 3.7. The value for the measured interstrip capacitance of the test structures is approximately 20% higher than the capacitance between two implants  $C_{n1}$ [42]. For the capacitance of the intermediate strip to the backplane half of the measured value for  $C_b$  from table 3.2 is used. It is assumed in the calculation that the signal in response to a hit on the readout strip corresponds to the total signal. Therefore the minor direct coupling between one readout strip and the next readout strips, as well as the coupling from the readout strip to the backplane is neglected. The series of coupling capacitance  $C_c$  and feedback capacitance times the open loop gain of the amplifier  $C_f A_0$  is much higher than the capacitances between implants and backplane, which justifies this assumption. This yields in drawing 3.20  $i_c \approx i_1$  and results in a simplification. Furthermore only capacitances are considered and all resistances are neglected. The ratio of intermediate strip to readout strip signal can be estimated from the simplified net in

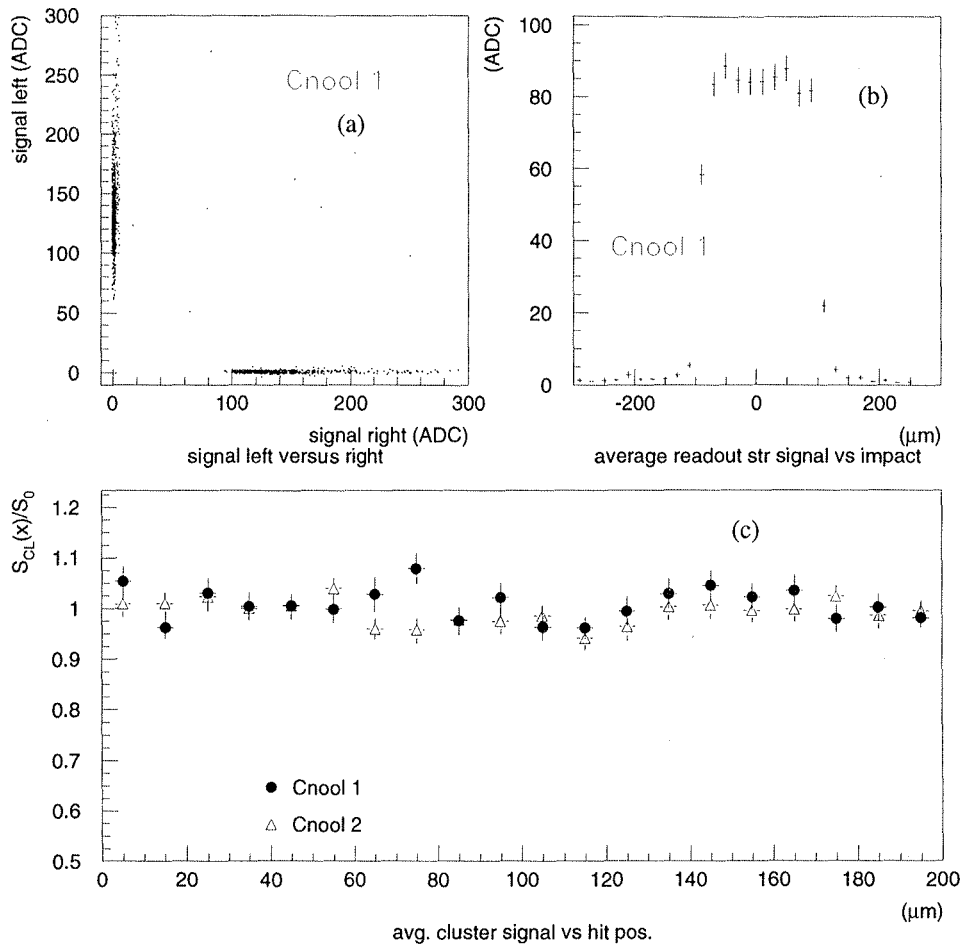


Figure 3.18: Correlation of single readout strip signal and their dependence on the track position for detectors without intermediate strips. The bottom plot illustrates the cluster signal as a function of the track position between two readout strip centres.

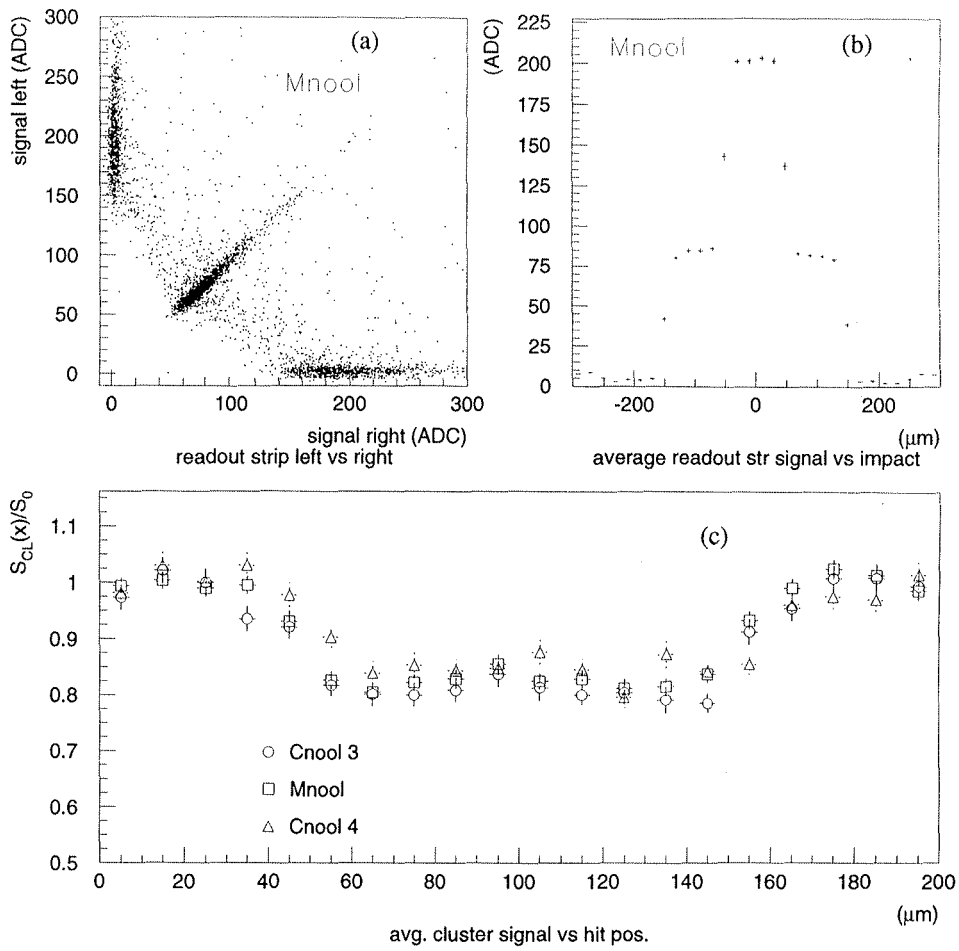


Figure 3.19: Correlation of single readout strip signal and their dependence on the track position for detectors with 1 intermediate strip. The bottom plot illustrates the cluster signal as a function of the track position between two readout strip centres.

figure 3.20 as

$$i_1 \left( \frac{1}{C_{n1}} + \frac{1}{C_c} \right) = i_2 \frac{2}{C_b}$$

$$\frac{S_i}{S_r} = \frac{2i_c}{2i_1 + i_2} \approx \frac{2i_1}{2i_1 + i_2} \quad (3.35)$$

Using the values for  $1.2C_{n1} = C_i$ ,  $C_b$  and  $C_c$  from table 3.2, the ratios obtained for detector CSEM nool 3, CSEM nool 4 and MIC nool are 80%, 82% and 78% which nicely agree with the measured value in figure 3.19

$$\frac{S_i}{S_r} = \frac{4C_{n1}C_c}{C_b(C_{n1} + C_c) + 4C_{n1}C_c} \quad (3.36)$$

To obtain precise values for the signal loss the cluster signal distributions measured for hits on readout and intermediate strip are compared in figure 3.21. The distributions



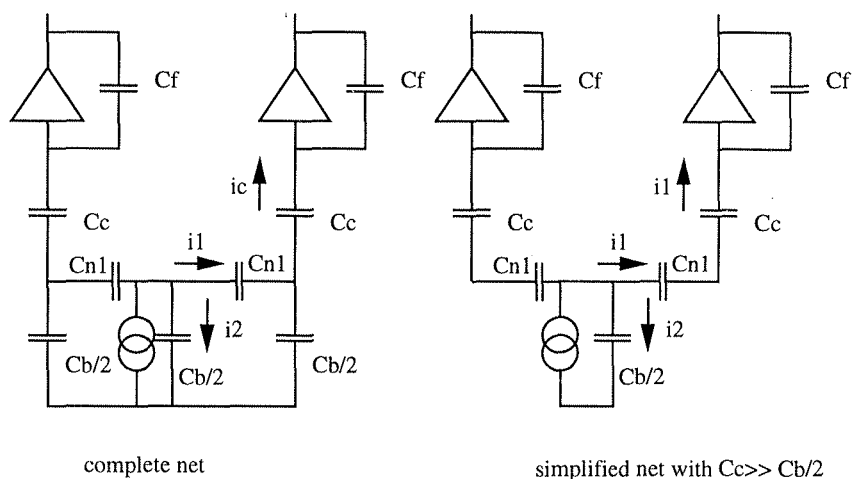


Figure 3.20: Complete and simplified net used for the estimation of  $S_i/S_r$ .

presented were measured for detectors with different implant widths but constant strip pitch of  $100\mu\text{m}$ . The solid line gives the distribution for hits on the readout strip, the dashed line the distributions for hits on the intermediate strip. The most probable cluster signal values are obtained from a Landau fit to the individual distributions. A major increase of signal is observed with increasing ratio of width to pitch, as the interstrip capacitance increases (see table 3.2) while the backplane capacitance remains constant. The ratio of most probable signal on intermediate to readout strip is displayed in figure 3.22 versus the ratio of interstrip to backplane capacitance. The line represents a straight line fit to the data points. The origin  $C_i/C_b = 0$  is included in the fit, as with  $C_b \rightarrow \infty$  no signal is expected anymore.

The signal response of a large readout pitch detector with 3 intermediate strips as measured on detector CSEM nool 5 is displayed in figure 3.23. The increased number of intermediate strips results in an enhanced dependence of the readout strip signal on the hit position as indicated by plot a and b. The detector response with 3 intermediate strips is dominated by capacitive charge sharing between right and left readout strip. The average readout strip signal depends nearly linearly on the hit position which allows preciser interpolation between the readout strips than in the case of only one intermediate strip. Regarding the signal loss to the backplane the situation is worse than for detectors with one intermediate strip. In the region between the readout strips 25% of the cluster signal is lost. Furthermore the fraction of events with full charge collection is decreased to 25% of the entire sample corresponding to hits directly under the readout strip.

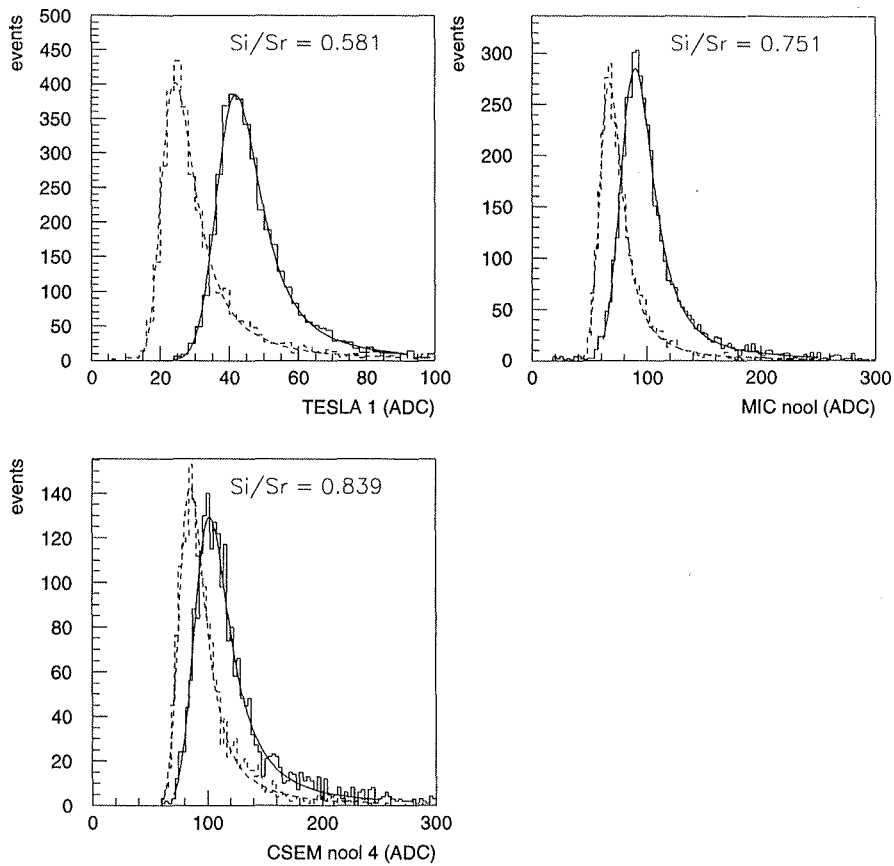


Figure 3.21: Cluster signal distribution for hits on readout strip (solid line) and intermediate strip (dashed line). All distributions are measured on detectors with one intermediate strip but different implant width.

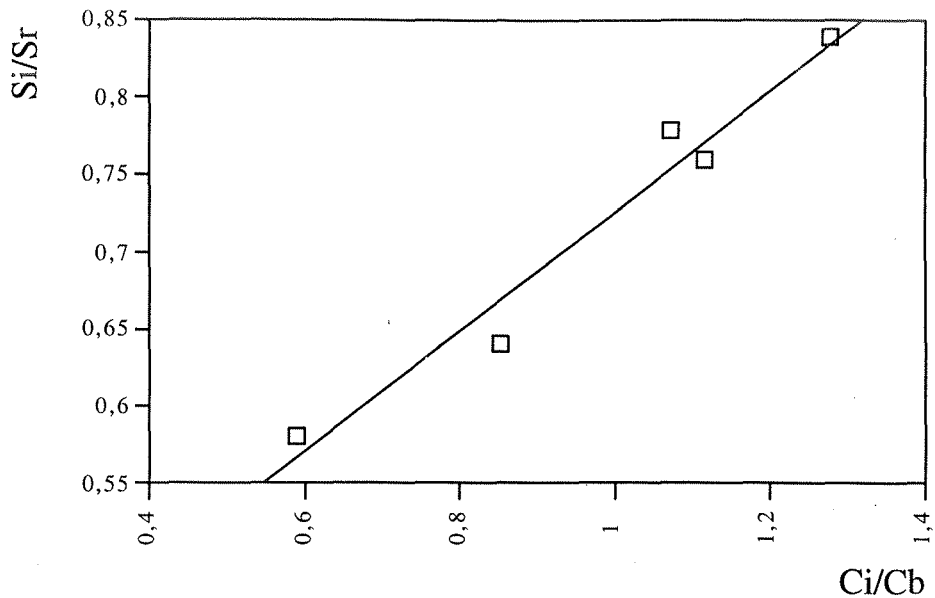


Figure 3.22: Ratio of most probable signal on intermediate to readout strip versus ratio of interstrip to backplane capacitance. The data points correspond to width-to-pitch ratios of 0.2, 0.4, 0.5, 0.6 and 0.75 .

### 3.4.4 Enhanced interstrip capacitance to avoid charge loss

To overcome the problem of charge loss in detectors with intermediate strips a new detector layout was investigated. The ratio of intermediate to readout strip signal depends on the ratio of interstrip to backplane capacitance. As the backplane capacitance remains constant for a given strip pitch, the signal ratio can be influenced by increasing the interstrip capacitance with an overlaying metal layer which couples the intermediate strip implants to the readout strip implants.

During the beam tests detectors with two different layouts of the metal layer (CSEM wiol and MIC wiol) are investigated. In case of the Micron detector MIC wiol the coupling is realised by a metal layer overlapping the entire intermediate strip and the readout strip implant by  $5\mu\text{m}$  in four discrete sections, each 1mm long. The four sections are equally distributed over the strip length of 2cm. The metal layer is separated from both implants by 200nm of silicon dioxide used for producing the coupling capacitance between readout strip implant and readout strip metal line. Thus no additional production step is needed in the detector fabrication. Using the dielectric constant for silicon dioxide  $\epsilon_{SiO_2} = 3.9$  the capacitance of each metal bridge to the strip implant can be estimated to be approximately 0.8pF. Concerning other parameters, the detector is identical to the MIC nool structure, i.e. it incorporates one intermediate strip with  $60\mu\text{m}$  implant width.

In the CSEM detector the metal layer overlaps the right and left intermediate strip implant by  $5\mu\text{m}$  ( $10\mu\text{m}$ ) and fully covers the central intermediate strip. The metal is deposited over the full strip length. In this way the coupling between the intermediate strips is enhanced, but does not fully connect them, as the capacitance between right and left intermediate strip is only half of the capacitance formed by the overlap. In

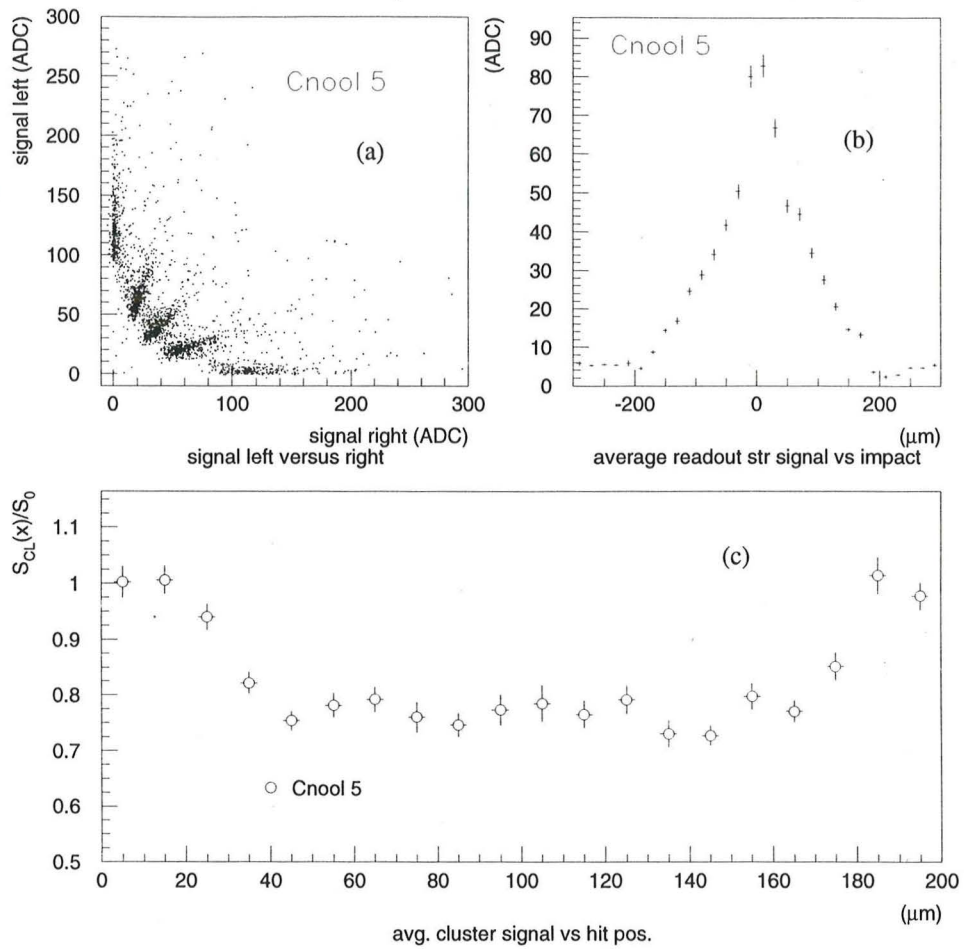


Figure 3.23: Correlation of single readout strip signal and their dependence on the track position for detectors with 3 intermediate strips. The bottom plot illustrates the cluster signal as a function of the track position between two readout strip centres.

addition to 200nm  $SiO_2$  used for the readout strip coupling capacitance, a 800nm  $Si_3N_4$  layer separates implants and metal layer. CSEM wiol 1(2) is apart from the metal layer identical to CSEM nool 5.

Figure 3.24 shows the single strip and cluster signal response for the two test structures in comparison with their counterparts without metal layer. The linear correlation for CSEM nool 5 between hit position and strip signal (plot a) is even improved, as the average loss of signal is limited to 10% compared to 25% without metal layer (plot b). The still present signal loss of CSEM wiol 1 might be due to the fact that the metal does not overlap the readout implant, but for charge sharing relies on the intrinsic capacitances between the implants. Small additional capacitances between readout implant and right and left intermediate implant might further improve the signal collection for CSEM wiol 1.

The same set of illustrations in plot c and d show the behaviour of MIC wiol compared to MIC nool. Plot d indicates less than 10% signal loss with the metal layer. The single strip signal  $S(x)$  for MIC wiol (plot c) exhibits an extreme asymmetry between hits right and left of the readout strip centre. This asymmetry could be traced back to a misalignment of the production masks for metal and  $p^+$  implant. The metal bridge is displaced by  $1.5\mu\text{m}$  to the right with respect to the implant centre which results in an effective overlap of  $6.5\mu\text{m}$  on one side and only  $3.5\mu\text{m}$  on the other. As this yields an asymmetric capacitance between intermediate strip and right and left readout strip, the signal is shared in favour of the right readout strip.

To compare the influence of charge loss on the overall signal distribution for different detectors under test, the most probable signal for the total signal distribution  $S_{mp}(all)$  is normalised the signal distribution measured in a  $30\mu\text{m}$  range below the readout strips  $S_{mp}(ro)$ . The “charge measurement efficiency” is defined as

$$\epsilon_S = \frac{S_{mp}(all)}{S_{mp}(ro)} \quad (3.37)$$

Values for the most probable signals are obtained from a landau fit to the individual distributions. Figure 3.25 shows the shift of the total signal distribution (solid line) with respect to the distribution below the readout strips (dashed line) for detectors with 1 and 3 intermediate strips. The charge measurement efficiency in dependence of  $C_i/C_b$  is presented in figure 3.26 for all test structures figuring intermediate strips.

### 3.4.5 Spatial resolution of different detectors

Only the fact, that the signal on the readout strip depends on the track position between the strips enables us to estimate the hit position with higher precision than readout pitch/ $\sqrt{12}$ . The overall resolution will depend on the individual contributions coming from different regions of the detector. All algorithms used to estimate the precise hit position are based on the measured or assumed correlation between readout strip signals in response to a track at a given position.

One simple way of estimating the hit position is by assuming a linear correlation between readout strip signals and distance to the strip centres. In this case the hit position can be calculated as a signal centre of gravity. When the charge is deposited on

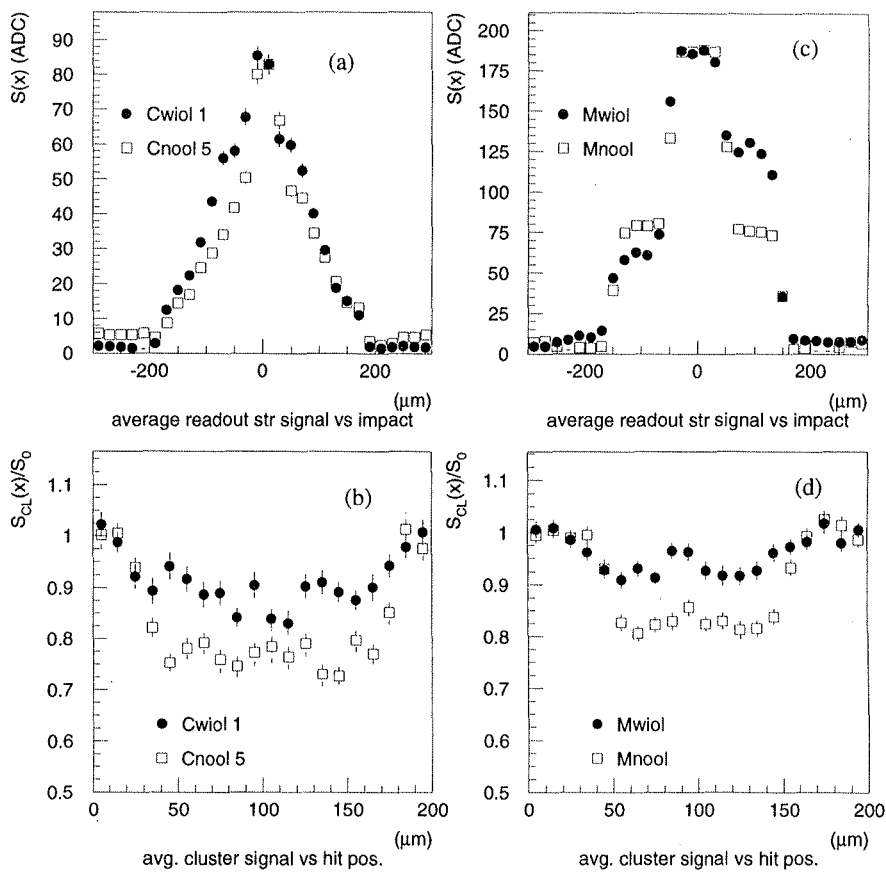


Figure 3.24: Single readout strip signal and cluster signal dependence on the track position for detectors with (full markers) and without (open markers) enhanced interstrip capacitance.

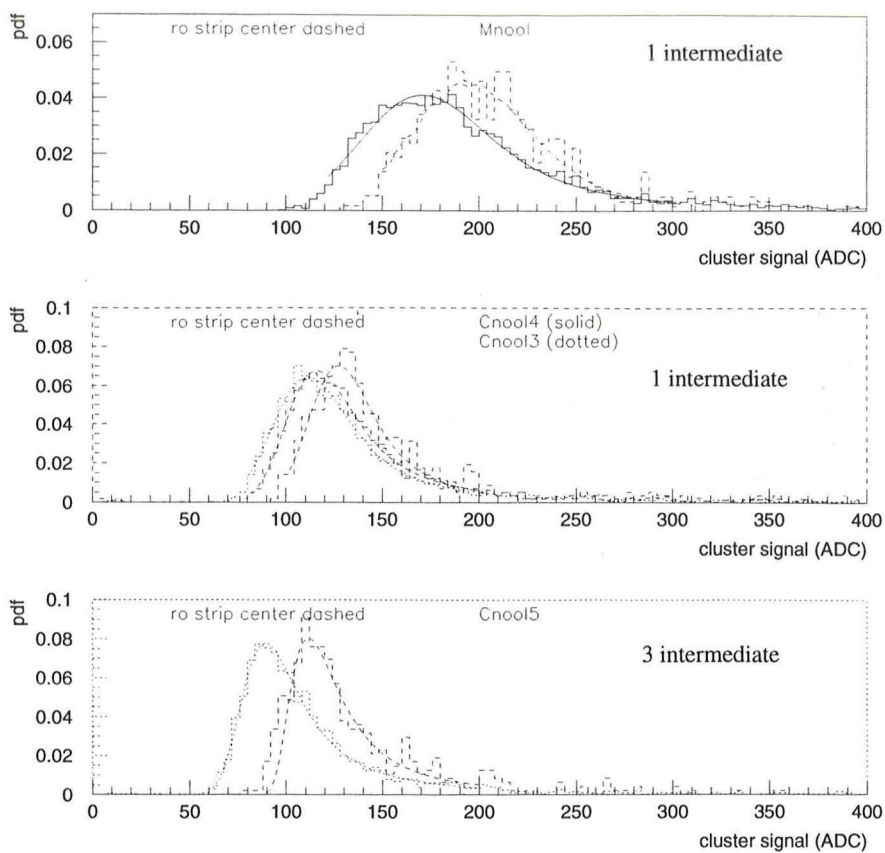


Figure 3.25: Total cluster signal distribution compared to cluster signal distribution next to the readout strip centre.

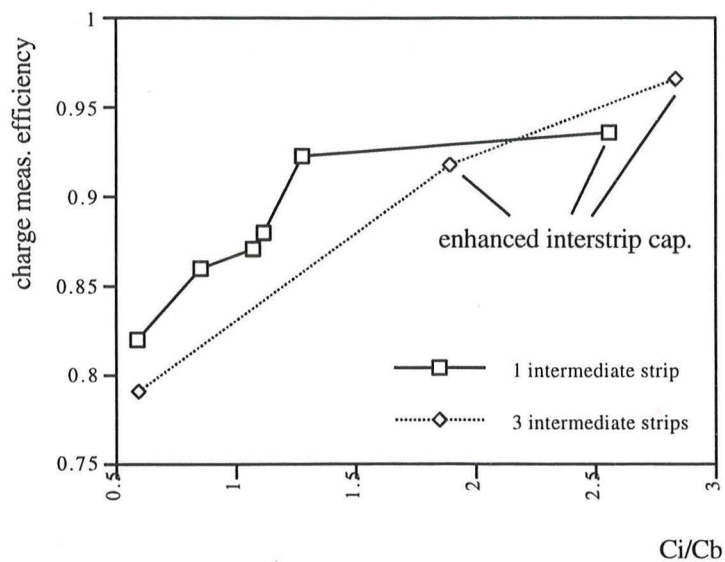


Figure 3.26: Charge measurement efficiency versus ratio of interstrip and and backplane capacitance for detectors with 1 and with 3 intermediate strips.

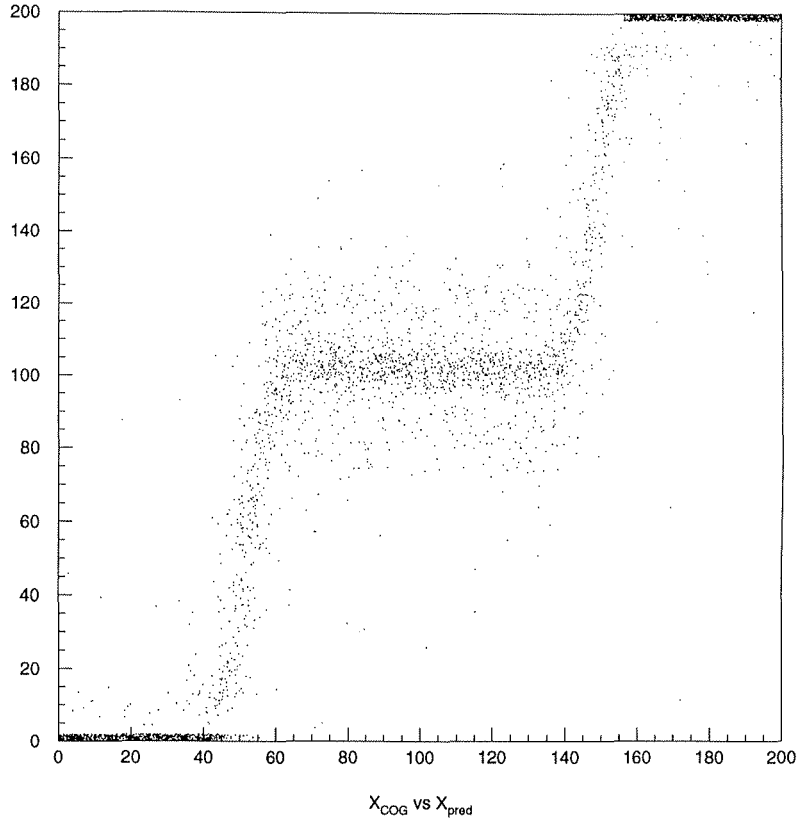


Figure 3.27: Hit position reconstructed with COG versus the predicted position for MIC nool at perpendicular track angle.

two strips the centre of gravity (COG) yields

$$x = X_0 + \frac{S_r}{S_l + S_r} \Delta = X_0 + \eta \Delta \quad (3.38)$$

where  $X_0$  denotes the position of the left strip in the cluster,  $S_l$  and  $S_r$  denote the signals on left and right strip respectively and  $\Delta$  the readout pitch. It is assumed that  $S_l$  and  $S_r$  are the two highest strips in the cluster. The reconstructed hit position using the COG method is displayed versus the predicted in figure 3.27. This plot nicely indicates the systematic error in the position reconstruction for different regions between the strips. The average over the entire region still will not show a systematic error.

Figures 3.18b and 3.19b clearly indicate, that the signal on the single readout strip does by far does not depend linearly on the track position between the strips. The plot demonstrates that the detector has two principally different region: in the first one close to the implant the reconstructed position is independent of the hit position, in the second one, in between the implant, the reconstructed position strongly depends on the precise hit position.

For two strip clusters the above relation still can be used when  $\eta$  is replaced by a function  $F(\eta)$  that reproduces the non linearities due to capacitive charge division,



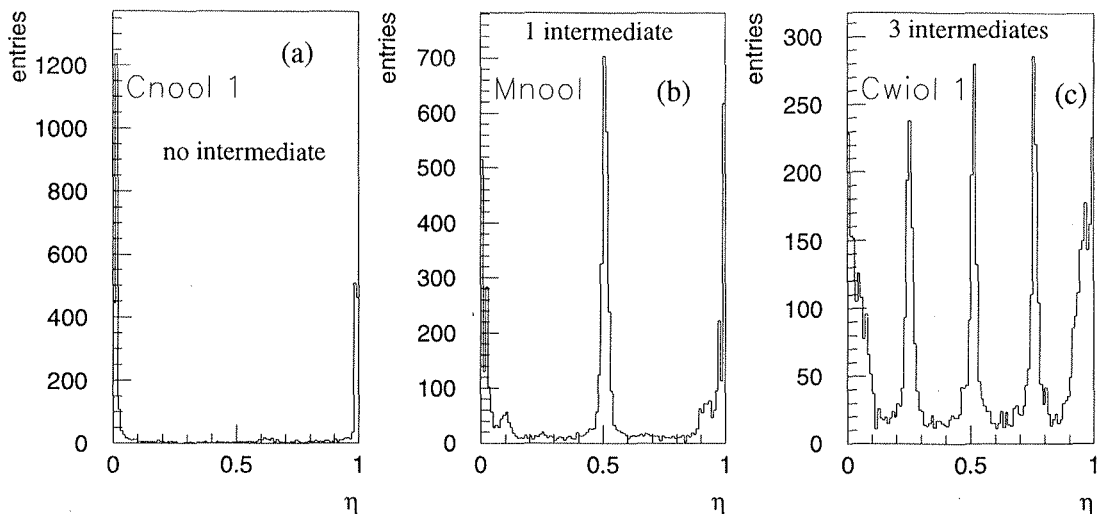


Figure 3.28: Measured distributions of  $\eta$  for detectors with no, one and three intermediate strips.

diffusion and track angle [43]. The probability density function for  $\eta$ ,  $f(\eta)$ , is related to the probability density function for  $x$ ,  $g(x)$ , i.e. the beam profile, as

$$f(\eta) = g(x) \frac{dx}{d\eta} \quad (3.39)$$

The beam profile in our case is uniform over the detector area, which was cross-checked in the data. Consequently  $g(x)$  is constant and the relation between  $x$  and  $\eta$  is obtained from the probability function for  $\eta$  as

$$\begin{aligned} x &= X_0 + \Delta \int_0^\eta f(\hat{\eta}) d\hat{\eta} = X_0 + F(\eta)\Delta \\ &= X_0 + \frac{\Delta}{N_0} \int_0^\eta \frac{dN}{d\hat{\eta}} d\hat{\eta} \end{aligned} \quad (3.40)$$

where  $\Delta$  denotes the readout pitch and  $dN/d\eta$  corresponds to the measured distribution of  $\eta$ . The total number of events  $N_0$  is used to normalise to the measured distribution. In the analysis the probability function  $F(\eta)$  is implemented as a look-up-table with 100 elements. This has the advantage of precise mapping and fast program execution. For large  $N_0$  and no noise the correlation presents the direct mapping of the non linearities between  $\eta$  and  $x$ .

The measured distribution of  $\eta$  for detectors with no, one and three intermediate strips is displayed in figure 3.28. The peaks represent the signal response for hits under the implant. In case of a linear signal correlation  $\eta$  would be uniformly distributed. Entries at  $\eta = 0, 1$  result from events where the entire signal is collected on one readout strip. The peaks can be obtained by projection the two-dimensional histogramm in figure 3.27 to the  $y$ -axis.

Generally a random variable distributed like  $f(\eta)$  can be obtained by transforming a uniform distributed random variable with the inverse (cumulative) distribution function.

Hence, for a given interval of  $\eta$ ,  $x$  is uniformly distributed over the detector region in which this  $\eta$  was measured. Considering the peak of  $\eta = 0.5$  in plot 3.28b the reconstructed  $x$  will be uniformly distributed over almost the full range of the intermediate strip, events with  $\eta = 0$  or 1 over the region of the readout strip. Consequently the resolution for these regions is expected to be the region width divided by  $\sqrt{12}$ .

The measurement error for  $x$  can be derived by propagating the error of  $\eta$  due to noise fluctuations added to the strip signal.

$$\begin{aligned}\sigma^2(x) &= \left(\frac{dx}{d\eta}\right)^2 \sigma^2(\eta) \\ &= \Delta^2 (f(\eta))^2 \sigma^2(\eta)\end{aligned}\tag{3.41}$$

To illustrate the correlation between the signal response and hit position figure 3.29 shows the measured  $\eta$  versus the predicted hit position for a detector with 1 intermediate strip (left) and with three intermediate strips. It shall be pointed out that two ways can be chosen to obtain the correlation: Integrating the  $\eta$  distribution the relation of  $x$  to  $\eta$  can be calculated. This approach is specially useful is no precise prediction of the hit position is available. The correlation obtained by the  $\eta$ -algorithm is drawn as a solid line. The second way to get the correlation is the direct measurement (and if possible parametrisation) of the correlation using a precise hit prediction. This methode is illustrated as a scatter plot. In our case the two approaches yield approximately the same results.

For both detectors  $\eta$  is constant if the track is in the region of the implant. The width of this region depends on the strip pitch and is thus smaller for three intermediate strips. If the track falls in the interface region between two strip implants, transversal diffusion yields a strong dependence of the charge ratios on left and right strip on the precise hit position.

The above general description of the error on  $x$  does not hold for the region with constant signal response for perpendicular tracks. Instead a simple description of the form of

$$\sigma(\alpha = 0) = \sqrt{\sigma_1^2 w_1 + \sigma_2^2 w_2}\tag{3.42}$$

can be used, where one term describes the resolution in the constant part, given by the region width, and the second term describes the resolution in the interface regions between the implants. From figure 3.29 it can be expected that the resolution in the interface region is substantially better, as a given fluctuation in  $\eta$  causes only a small one in  $x$ .

To determine the resolution for each detector, the residual of  $x_{meas} - x_{pred}$  in the detector plane is calculated. The resolution is obtained from the r.m.s. of the measured distributions. For the detectors with three intermediate strips the resolution quoted corresponds to the standard deviation of the fitted Gaussian distribution. Figure 3.30 points out the significant influence of the intermediate strips for the detector spatial resolution. An excellent resolution of  $10\mu\text{m}$  is achieved for the detector with 3 intermediate strips at a readout pitch of  $200\mu\text{m}$ . Detectors with one intermediate strip exhibit a resolution of  $22\mu\text{m}$  to  $28\mu\text{m}$ . The S/N for the CSEM and Micron detector is approximately 100 and 50 respectively. The expected digital resolution of  $60\mu\text{m}$  is exceeded due to alignment problems with this structure and occasional high noise fluctuations on some channels.

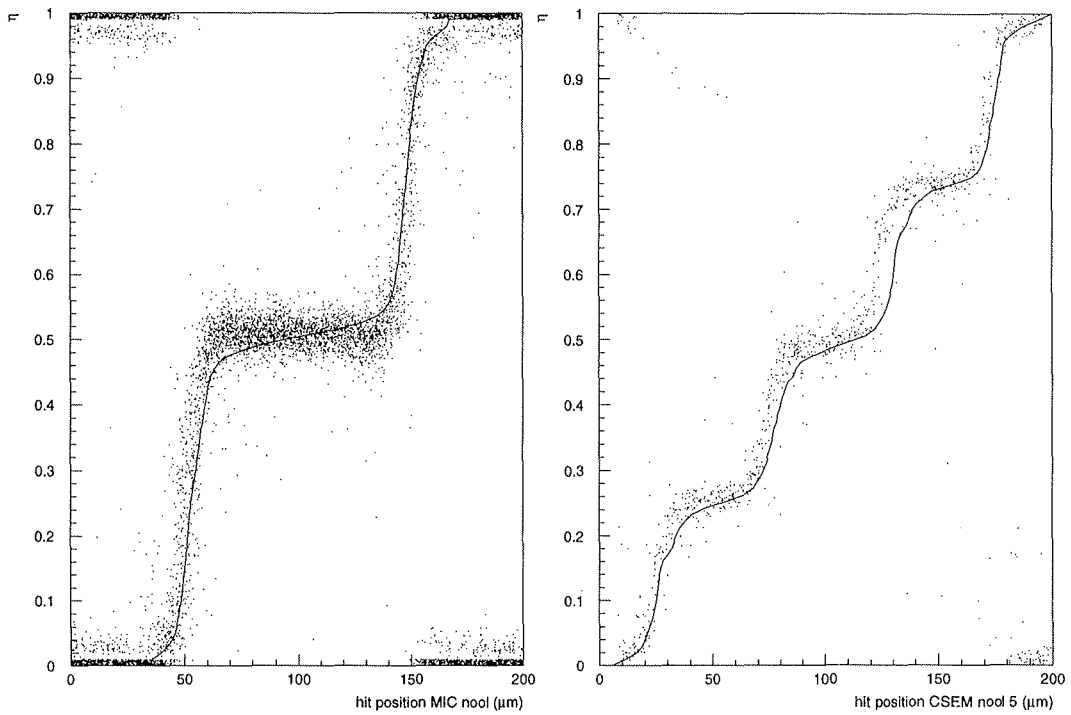


Figure 3.29: Measured  $\eta$  versus the predicted hit position for a detector with 1 intermediate and one with 3 intermediate strips. The correlation obtained from the  $\eta$ -algorithm is superimposed as a solid line.

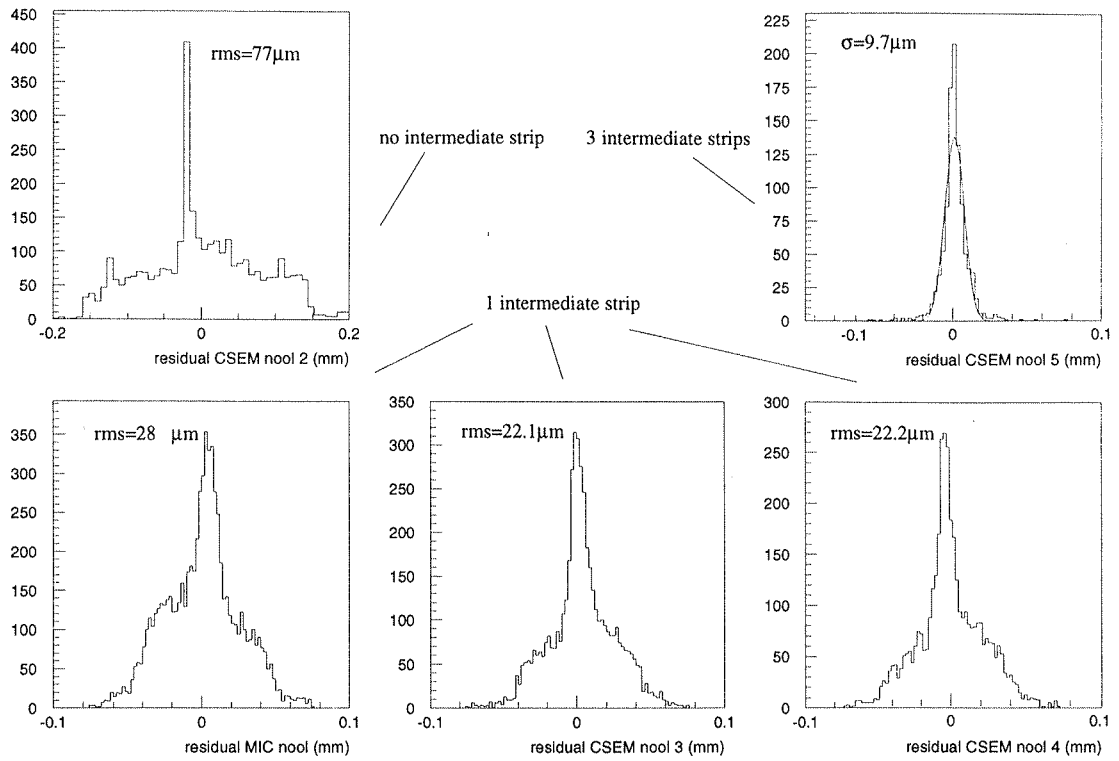


Figure 3.30: Residual distributions measured for detectors without additional metal layer.

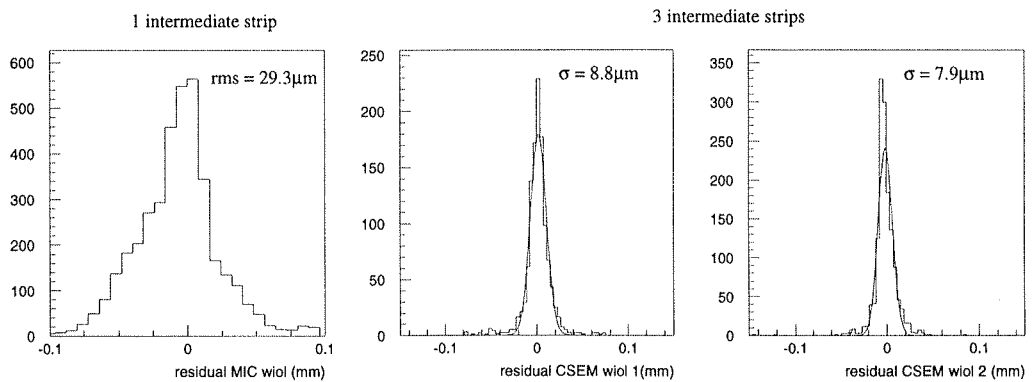


Figure 3.31: Residual distributions measured for detectors with additional metal layer.

The residual distributions for the detectors featuring an additional metal layer are displayed in figure 3.31. In case of 1 intermediate strip the resolution remains unchanged with respect to the same structure without metal layer. In case of 3 intermediate strips the resolution slightly improves to  $8\mu\text{m}$ . It has to be pointed out that the measurement error on the hit position corresponds to only 4% of the readout pitch. The improvement from  $10\mu\text{m}$  to  $8\mu\text{m}$  is likely to be due to the higher S/N found for the metal layer structures CSEM wiol 2. In case of the metal layer structures, the theoretical S/N limit of 115 for this detector-electronic configuration could be achieved, whereas the signal over noise performance on CSEM nool 5 was 30% less than expected which might be due to external noise sources.

The residual distributions for 1 intermediate strip exhibit clearly two contributions that lead to a non-gaussian measurement error. The residual distributions are presented in figure 3.32 versus  $\eta$  for one and three intermediate strips. For the MIC nool detector a resolution of  $25\mu\text{m}$  is measured in the regions of  $\eta = 0, 0.5, 1$ . The events in these regions amount to 80% of the data sample. Comparing this plot to the distribution of  $\eta$  versus the predicted hit position shows that the first regions relate to hits next to strip implants, where  $\eta$  is constant and the detector acts like "digital". The resolution corresponds to the width of the region with  $80\mu\text{m}/\sqrt{12}$ . In the other areas the detector exhibits a resolution of  $4.6\mu\text{m}$ . Those events correspond to hits in the interface between implants where charge sharing is dominated by diffusion which allows good interpolation. The events in the latter region, which is approximately  $20\mu\text{m}$  wide, constitute 20% of the sample.

The same behaviour is found for the detector with 3 intermediate strips though the region of constant  $\eta$  is narrower by a factor of two, leading to a significantly better resolution. Furthermore the detector has four regions where diffusion dominates the charge sharing, each  $20\mu\text{m}$  (FWHM) wide. Therefore the weight on the measurement error in the diffusion region is increased and the population of the digital part reduced. This circumstance explains the significant resolution improvement when using 3 instead of 1 intermediate strip.

### 3.4.6 Influence of signal to noise performance on the spatial resolution

The S/N performance does not only influence the cluster finding, the number of ghost clusters and the efficiency but also the spatial resolution. As shown above the total residual distribution has two components coming from the digital section below the intermediate and readout strips as well as one from the diffusion dominated sections.

In the digital region the resolution is determined by the region width, in case of one strip  $80\mu\text{m}$  and approximately  $30\mu\text{m}$  for 3 intermediate strips. As the reconstructed clusters are uniformly distributed in this region the resolution is expected to be nearly independent of the S/N, but instead will be given by region width divided by  $\sqrt{12}$ . In the interface region the reconstruction precision is significantly influenced by the measurement precision of the signal and will improve with S/N. Thus a total resolution proportional to  $\frac{1}{S/N}$  plus a constant offset is expected.

To investigate the spatial resolution versus the S/N performance for the analysed

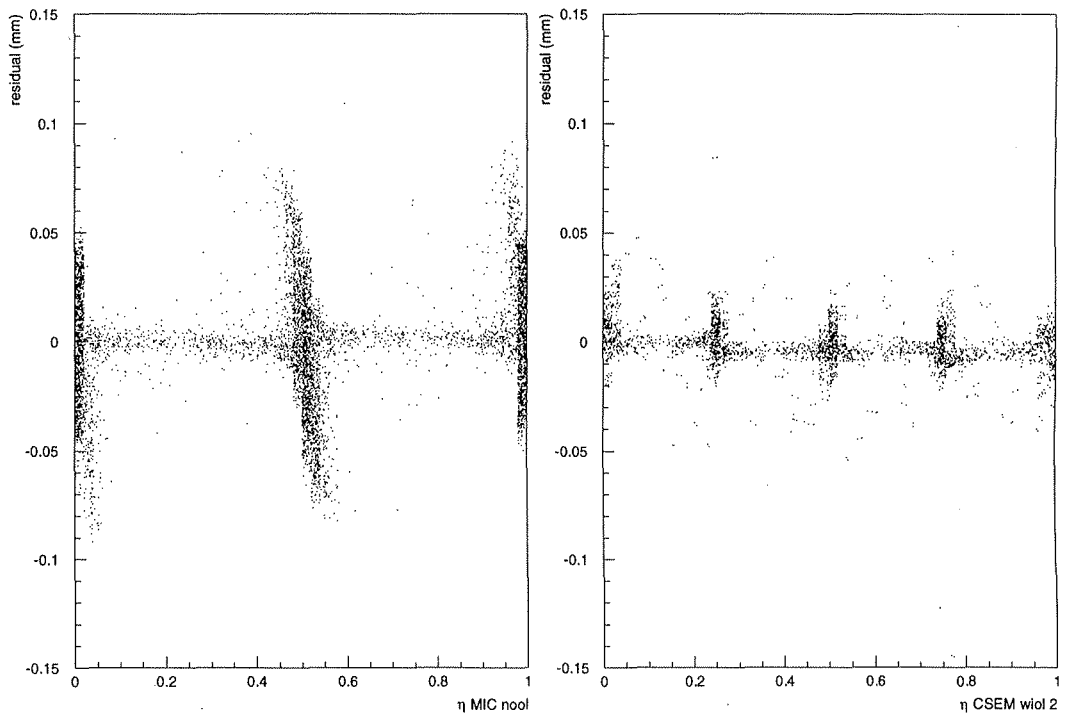


Figure 3.32: Residual distributions versus  $\eta$  for a detector with one intermediate strip (left) and with three intermediate strips (right).

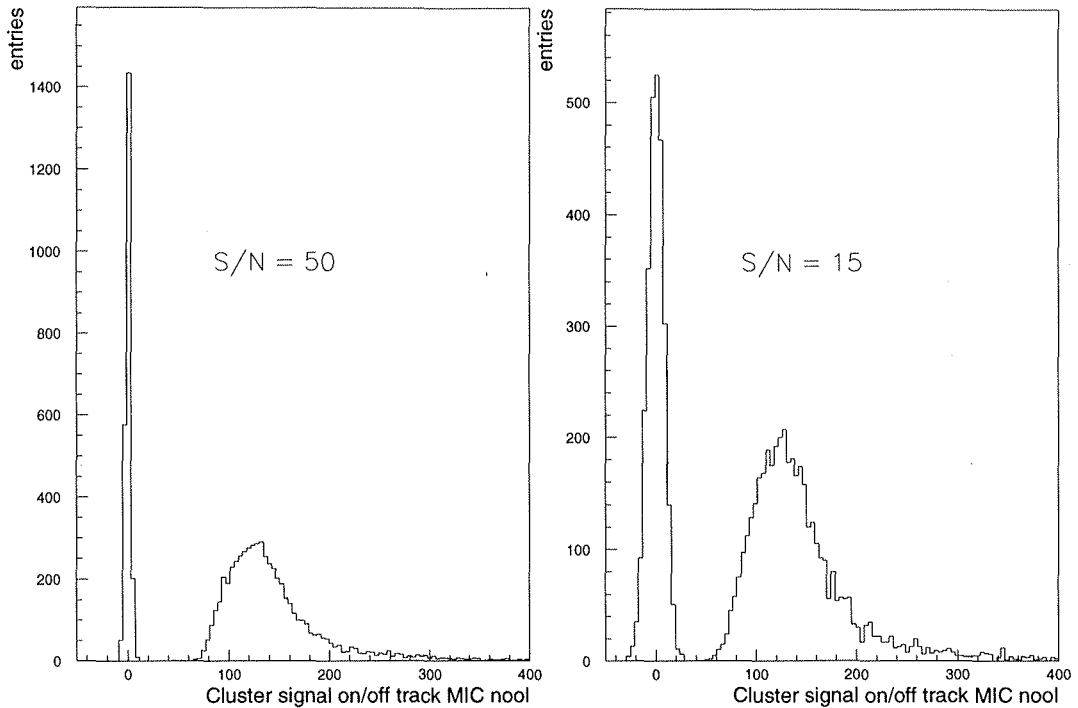


Figure 3.33: Signal and noise distribution for high and low S/N performance.

detectors, the single strip noise is increased artificially and the entire analysis repeated to extract new  $\eta$  and residual distributions.  $F(\eta)$  is newly calculated for each sample, no information from a high S/N performance run is used.

The single strip noise is increased by adding gaussian distributed noise fluctuations to the measured strip signal. This yields single strip signals of the form

$$S = S_{track} + S_{noise} + S_{generated} \quad (3.43)$$

$S_{track}$  is Landau distributed and  $S_{noise}$  and  $S_{generated}$  are gaussian distributed.  $S_{noise}$  denotes the intrinsic present noise. Figure 3.33 illustrates the original signal distribution for the Micron detector with the noise peak of a single strip being superimposed. The right plot shows the same distributions after artificial noise has been added. In the low S/N case, noise peak and signal distribution are well separated which is important to maintain the high efficiency and avoid ghost clusters. The effect of additional noise on the  $\eta$  distribution is illustrated in figure 3.34 for the Micron detector MIC nool with one intermediate strip and the CSEM nool 5 detector with 3 intermediate strips. It can be clearly seen that the additional noise smears the peaks, as the variance of  $\eta$  increases proportional to  $\frac{1}{S^2/N^2}$ . The residual distributions widens with decreasing S/N. Nevertheless at an extremely low S/N of 12 a spatial resolution of  $16\mu\text{m}$  is obtained for three intermediate strips. The resolution of the Micron detector changes only slightly as it is dominated by the resolution of the digital parts. Figure 3.35 shows the dependence of the resolution on the S/N performance for the CSEM detector with and without metal

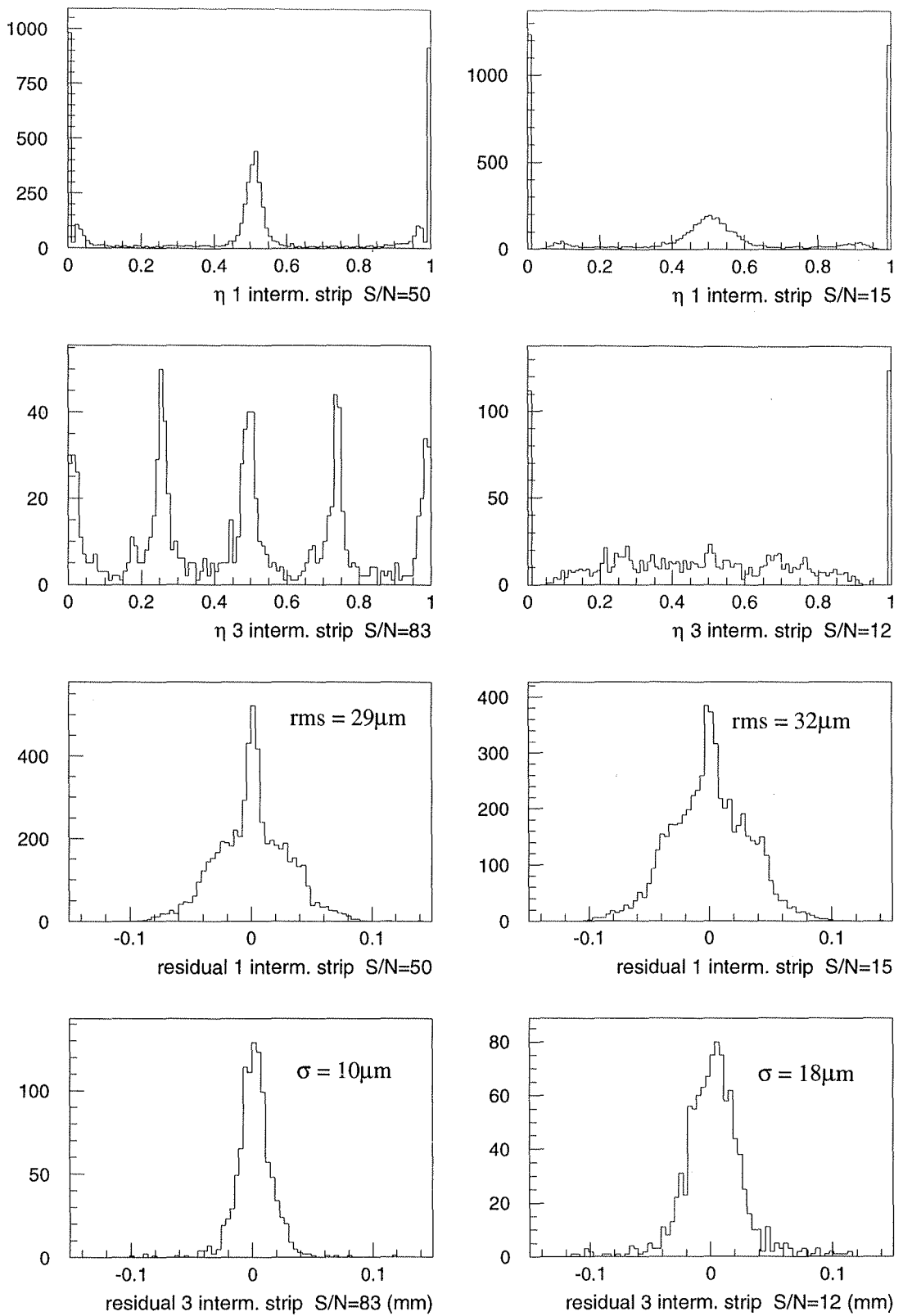


Figure 3.34:  $\eta$  and residual distribution for high and low S/N performances as reconstructed for MIC nool and CSEM nool 5.



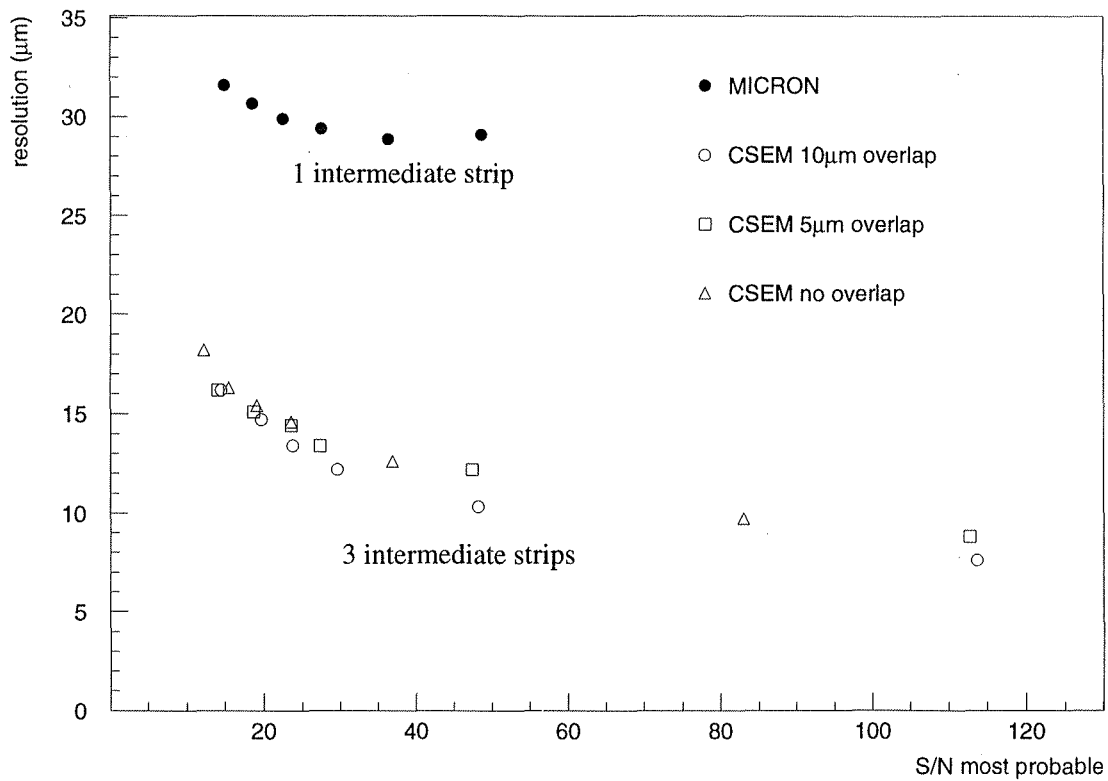


Figure 3.35: The overall spatial resolution versus S/N performance. The resolution is obtained from the residual distribution for the entire detector.

layer and for the Micron detector for different values of  $S/N$ . A clear improvement of the resolution with  $S/N$  is observed on the detectors with 3 intermediate strips (CSEM).

# Chapter 4

## Position reconstruction with the VFT detector at different track angles

In the previous chapter the capabilities of different detector layouts were demonstrated. The tests showed, that with a detector layout with one intermediate strip and a readout pitch of  $200\mu\text{m}$ , a spatial resolution of  $28\mu\text{m}$  can be achieved for perpendicular tracks. As it will be demonstrated in this chapter a track inclination with respect to the detector surface will further improve the resolution.

The choice of one intermediate strip with an implant width of  $60\mu\text{m}$  for the ministrip detector layout is motivated by the good signal measurement efficiency and low noise due to a small detector load capacitance. In the final detector, as ready for installation, particle hits are reconstructed with a signal to noise of 30 (see chapter 5). This guarantees reliable operation with high efficiency and low number of ghost clusters.

The reliability of the system and our concerns about the long time stability of the detector are the main motivation for the simple layout. The detector can be produced with well known and reliable processes by many manufacturers, having long years experience in the production of silicon detectors.

In this chapter beam test measurements carried out on VFT ministrip detectors shall be presented. The main focus of this chapter is to determine the position resolution for different track angles and to test a possible systematic error in the position reconstruction for inclined tracks. The detector tested is a single-sided VFT ministrip detector being read out by the VIKING chip.

The test setup and conditions are the same as the one presented in the previous chapter. The strip side is placed beam upstream in the same position as that of the test detector illustrated in figure 3.16. The strip orientation is parallel to the  $y$  axis. In the data analysis, the detector is aligned for shifts along  $x$  and  $z$ , as well as for rotations around the beam axis. To obtain measurements at different track angles, the test detector is rotated around the central strip axis from  $\alpha = -30^\circ$  to  $\alpha = 30^\circ$  in steps of  $5^\circ$  around the strip axis. The measurements at different track angles give a deep inside view of the charge collection properties of this detector.

## 4.1 Detector signal and spatial resolution

### 4.1.1 Signal measurements at different track angles

Apart from diffusion and capacitive coupling between the strips, an inclination of the tracks in the plane perpendicular to the strip orientation and the detector plane will also result in a spread of the signal over several strips. The effect of track inclination is manifold: The total cluster signal will increase as the path length of the particle increases with  $1/\cos \alpha$

$$S(\alpha) = \frac{S_0}{\cos \alpha} \quad (4.1)$$

The signal on one single strip will decrease as the path length within the collection area of one strip decreases with respect to perpendicular tracks. Thus the S/N for the single strips decreases which may cause problems in the detection of the signal on cluster edges in case of high noise. If only the strips on the edge of the cluster are used for a position estimate the decreasing S/N can effect the resolution. It also has to be mentioned that the probability of  $\delta$  ray emission increases according to the path length, which can spoil the spatial resolution.

In the case of the VFT detector, where the inclination angle is limited to roughly  $30^\circ$  and the strip pitch is large, the track inclination will result in a charge deposition on more than one strip. This allows to use charge interpolation between the strips to improve the resolution as it will be shown later.

The number of strips which collect the signal is determined by the projection of the track segment in the detector to the strip plane. For tracks perpendicular to the strip axis (but not to the strip plane), the projection increases as  $T \tan \alpha$  with the track angle, where  $T$  denotes the detector thickness. In case of  $30$  degrees inclination this corresponds to  $173\mu\text{m}$  projected track length on the strip plane. Furthermore the actual number of strips carrying some signal information will be determined by transversal diffusion and coupling between the readout and intermediate strips.

### Signal measurements using the track prediction

To evaluate the signal response at various track angles two different approaches were chosen: in one thresholds are applied to the signal, in the other one the track prediction is used to determine the cluster signal.

In the commonly used cluster finding thresholds are imposed on the measured strip signal as described in section 3.3. A single strip threshold  $C_s = 2.5$  and a cluster threshold  $C_c = 6.0$  is used to identify the cluster. This analysis method, referred to as "threshold analysis" uses the signal information on the test detector. Therefore the results may slightly be influenced by the cluster finding and selection of events.

To avoid these problems, an unbiased signal calculation was carried out. After the track is reconstructed with the information from the reference system, the track impact on the test detector is predicted. Using the alignment data from the reference and test detector, the number of the strip next to the impact is calculated. The cluster signal is obtained as the sum of the signals from  $n$  readout strips closest to the prediction. No thresholds are imposed on the data. As noise contributions on the single strip signal

and contribution from ionization are uncorrelated and the average noise contribution is zero, the calculated signal average is unbiased. This analysis is referred to as “prediction analysis”.

$$\begin{aligned}
S &= \sum_{i=1}^n S_{track}(i) + S_{noise}(i) \\
\text{var}(S) &= \text{var}\left(\sum_{i=1}^n S_{track}(i)\right) + nN^2 \\
&\quad \text{with } N = \sigma_i(S_{noise}) \\
\langle S \rangle &= \left\langle \sum_{i=1}^n S_{track}(i) \right\rangle
\end{aligned}
\tag{4.2}$$

$$\tag{4.3}$$

Figure 4.1 shows the signal response as obtained by the threshold analysis at track angles from  $0^\circ$  to  $30^\circ$ . On the left side the cluster signal distribution is displayed, on the right side the number of strips in the cluster is plotted. At  $0^\circ$  track incident the signal distribution has two components, one from hits on the intermediate strip and one from hits under a readout strip. As 24% of the deposited charge is not measured in case of hits on intermediate strips, its average signal is smaller than in case of hits on the readout strips. The convolution of the two contributions widens the total distribution. Hits on the readout strip yield clusters with one strip and hits on intermediate strip clusters with two strips. Their fraction is roughly equal. Two strip clusters are slightly enhanced by diffusion. Three strip clusters can be correlated to the events in the Landau tail of the signal distribution coming from  $\delta$ -rays. With increasing track angle, the average signal increases and the fraction of events with two or more strips in the cluster increases. At  $30^\circ$  track inclination the signal is deposited on two or more strips. The total ionization is partially deposited below intermediate and readout strips.

In the analysis using the hit prediction on the test detector the total cluster signal is given by the sum of  $n$  single strip signals next to the prediction. Figure 4.2a shows the average signal versus the number of strip used in the sum. The curves for different track angles are superimposed. The strip where the hit is predicted ( $n = 1$ ) contains on average 75% of the total cluster signal; that is reached when the second or third strip next to the prediction is included in the sum. Adding more than three strips does not increase the average signal anymore but only the distribution width as expected from equation (4.2). The average cluster signal for  $n = 3$  is displayed versus the track inclination in figure 4.2b. The increase of the signal with track inclination can be seen clearly, the expected signal dependence on the path length according to equation (4.1) is superimposed as a dashed line. Plot figure 4.2c shows the average cluster width as obtained in the threshold analysis. Both analyses give consistent results concerning cluster width and signal.

### 4.1.2 Single strip signal correlation

As the position reconstruction is based on the signal information from each readout strip, the correlation of the strip signals in the cluster is of major importance. The correlation of the readout strip signals has been precisely measured for different track angles in the testbeam with VFT ministrip detectors.

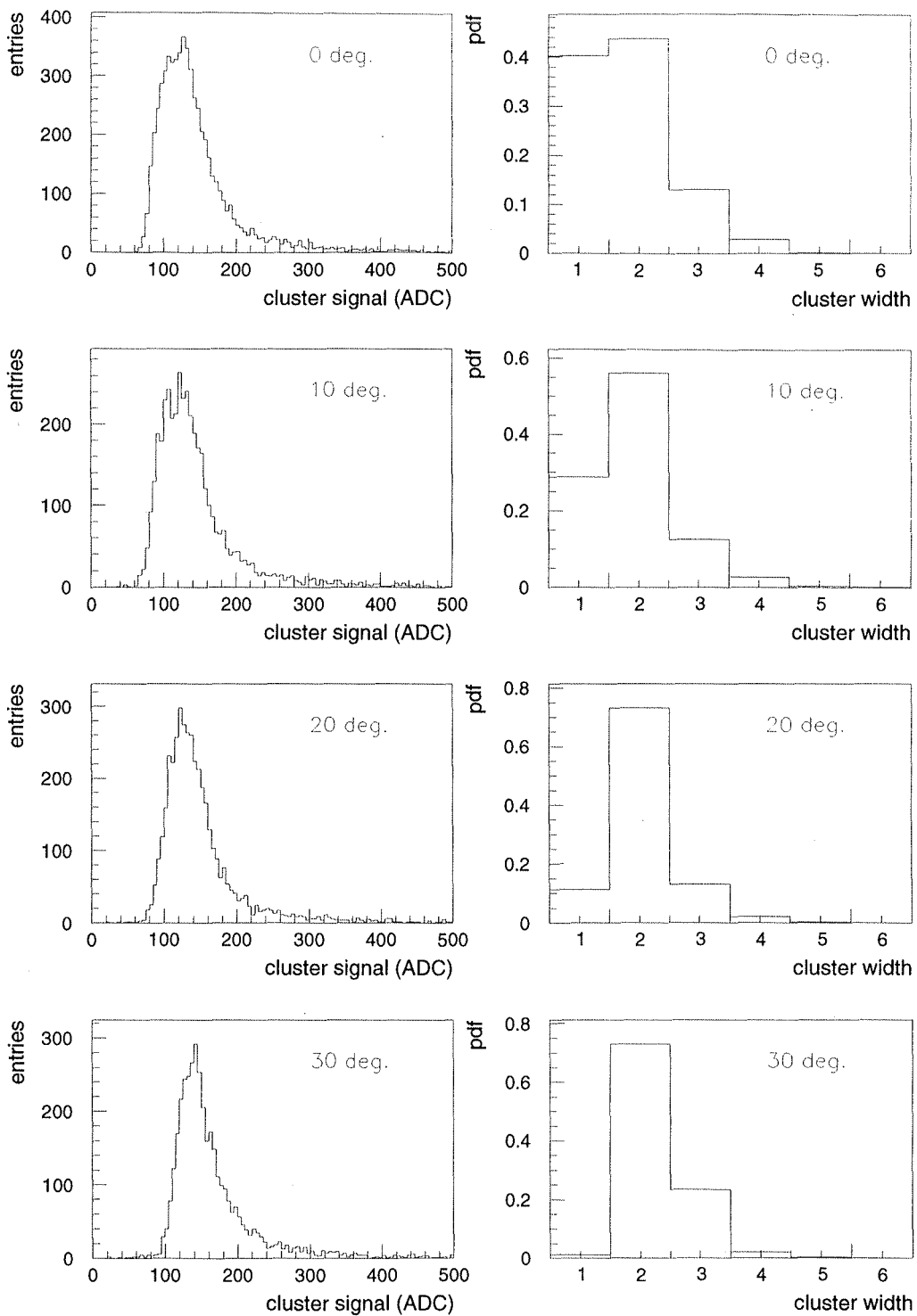


Figure 4.1: Distributions of cluster signal (left) and width (right) as obtained by the cluster finding using thresholds as measured in the test beam with a VFT ministrip detector. At  $0^\circ$  in nearly 50% cluster is contained on a single strip.  $30^\circ$  the charge is always charge among several strip, thus the single strip clusters vanish.

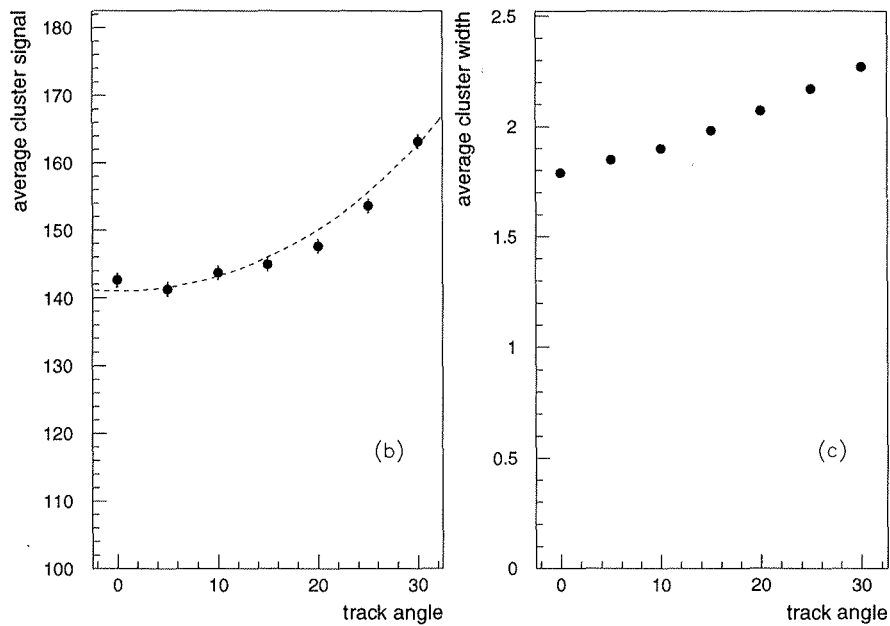
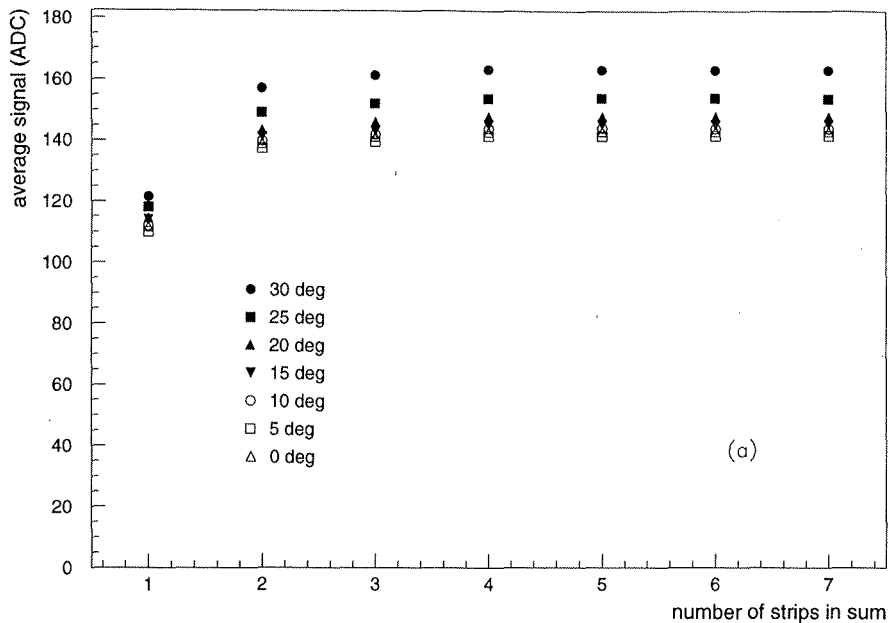


Figure 4.2: Average cluster signal versus number of strips used for the signal sum in the analysis using the track prediction (plot a). Plot b shows the average signal sum for  $n = 3$  at different track angles together with the expected  $1/\cos \alpha$  behaviour. Plot c gives the average cluster width versus the track inclination for the analysis imposing thresholds (see text).

## Modelling of the detector response

In order to provide a better understanding of the processes leading to the observed signals on the readout strip a signal model was prepared. Processes determining the size and time dependence of the signal on the strips are

- position of the charge deposition in the detector bulk
- the electric field distribution between strip implants and backplane
- the drift path and velocity of electrons and holes depending on the electrical field
- transversal diffusion during the drift
- capacitive coupling between intermediate and readout strips as well as coupling between the readout strips.

To describe the net induced charge difference between the creation time of electron-hole pairs and the time when they reach the electrodes a simple electrostatic model is considered. The detector is described by an infinite electrode plane on one side, corresponding to the n-side of the detector, and a plane of strips, the p-side, parallel to it at a distance equal to the thickness of the detector. The layout is represented in figure 4.3a.

At the creation time  $t_A$  of the electron-hole pair the total induced charge  $Q(t_A)$  on the electrode  $M$  has a contribution from the electron and additionally from the hole with same absolute value<sup>1</sup> but different signs. Hence the total induced charge  $Q(t_A) = 0$ . At a time  $t_B$  when the electron reaches the backplane, the electron will only induce charge on the backplane and none on the strip side. Similarly at  $t_B$  the hole will only induce charge on electrode  $M$ . All charges  $Q$  in figure 4.3 reflect a time dependent charge and not a time integrated charge. If one is only concerned about the total induced charge difference between creation time and absorption time of e-h pairs, the model of electrons and holes drifting is equivalent to a single charge (hole) drifting along the entire path as illustrated in figure 4.3b. The drift path is determined by the electrical field and diffusion.

The above said is reflected in the simulation by two assumptions: First, the on the strip side induced signal per created electron-hole pair corresponds to the signal that a hole drifting through the entire detector would induce. Thus the total signal size is independent of the distance where this electron-hole pair was created. Second the entire signal is on the electrode where the drift terminates.

During the process of charge collection the electrodes  $S_1$  and  $S_2$  act as “spectator” electrodes: At the time of creation the induced charges from electron and hole cancel on  $S_1$  and  $S_2$ . While they separate due to the drift field their contributions will not compensate and thus a net induced charge can be observed on them. When the hole and electron reach electrode  $M$  and the backplane, the induced charge on  $S_1$  and  $S_2$  is zero again. The integral over the induced current between creation and collection time is zero for the spectator electrodes. The model of spectator electrodes has successfully been used for the signal calculation of drift chambers with split cathode plates [36].

---

<sup>1</sup>The contribution from each charge is given by the integral of the electric field produced by the charge, over the surface of the electrode  $\int \vec{E} d\vec{A}$



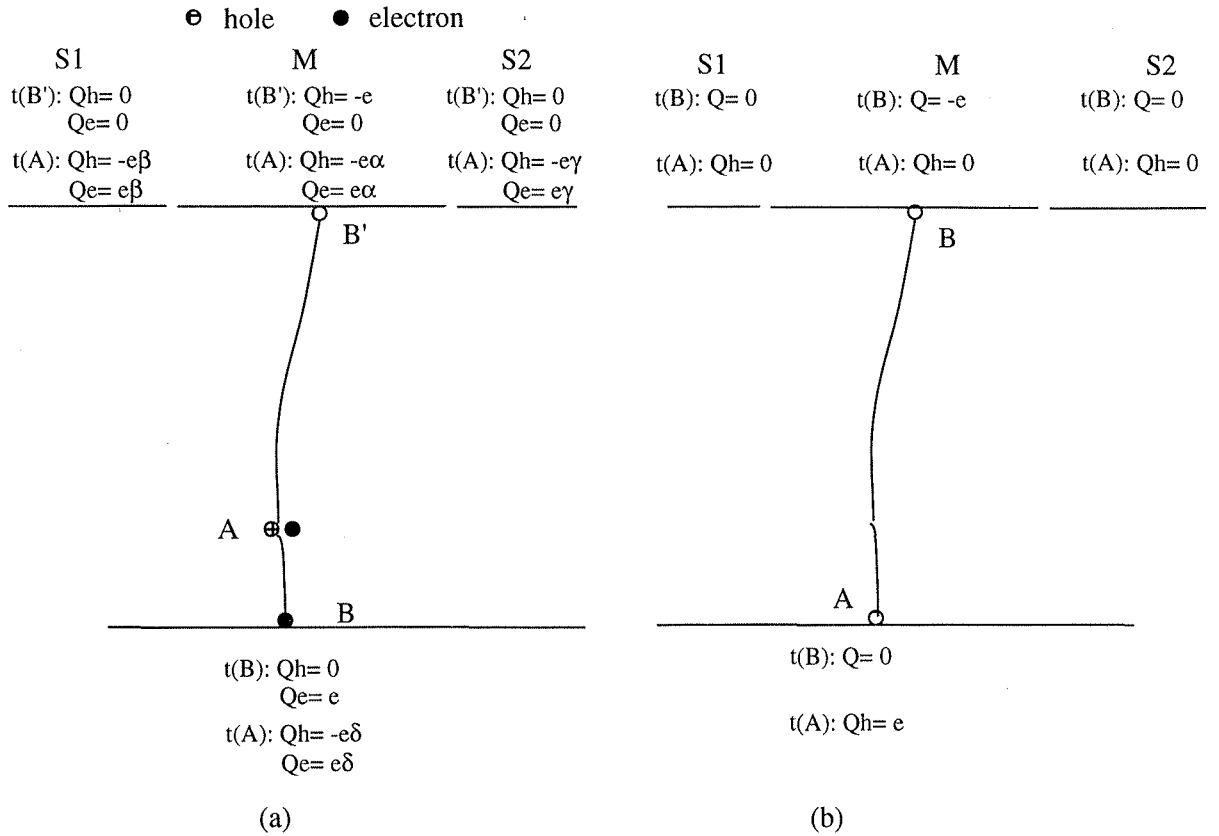


Figure 4.3: Simulation model used for the description of the time dependent induced charge on the strip surface for the drift of an electron-hole pair (a) and an equivalent hole charge through the entire detector (b).  $\alpha$ ,  $\beta$ ,  $\gamma$  and  $\delta$  denote the fraction of induced charge on each electrode either electron or hole at  $t_A$ .  $t_A$  and  $t_B$  denote the time immediately after the creation and before the absorption of the charge. No homogenous electrical field has to be assumed to describe the charge collection in this model. The application of a homogenous field is only used in the model for simplification while modelling the diffusion.

Several assumptions apply to this simple model of charge measurement:

1. As only the difference in induced charge between creation time and collection time is regarded, it is important that the time, when the induced charge is measured is longer than the collection time needed to drift the electrons and holes to the electrodes. In this case the complicated calculation of the electrical field and the time dependence of the induced signal current can be omitted. For the preamplifier used for the tests, the integration time is significantly longer than the collection time, which is about 20 to 30 ns.
2. The electrodes and amplifier have to have low impedance and act like “grounded” so that they can absorb and supply current. Otherwise, the signal deposited on a readout electrode is not completely transferred to the amplifier, or the integral of the signal current on the spectator electrodes does not cancel.
3. One important limitation is the requirement that no charge is trapped during the drift to the electrodes. In case of charge trapping the signal size will depend on the creation and trapping point of the electron-hole pair and a more complicated simulation, e.g. using weighted field methods as described in references [37][38][39] and references therein, is required to describe the induced signal.
4. The electrons and holes have to reach the electrodes in a shorter time than the integration time of the amplifier. Ionization charge that drifts very slowly towards the electrode produces an induced current signal with a long time constant. The amplifier integration time may be too short to sufficiently integrate this tail of the current signal.

Technically the simulation proceeds in two steps: first a charge generation at several points along the track in the bulk, and second the signal collection on intermediate and readout strips. The path of the particle through the detector of  $300\mu\text{m}$  thickness is split in 30 individual segments as illustrated in figure 4.4. A Landau distributed energy loss for a minimum ionising particle is generated in each segment individually. Each segment is characterized by its position in the bulk  $x_i$  and  $z_i$  and its charge  $q_i$ . The charge is strictly distributed along the track, thus no  $\delta$ -rays are simulated.

The detector is assumed to have a homogeneous<sup>2</sup> electrical field  $V_{fd}/T$ , where  $V_{fd} = 45\text{V}$  is the full depletion voltage and  $T = 300\mu\text{m}$  the detector thickness. To simulate the effect of diffusion, the generated charge  $q_i$  is assumed to have two fractions  $q_{i,1} = \frac{\frac{T}{2} - z_i}{T} q_i$  and  $q_{i,2} = \frac{z_i + \frac{T}{2}}{T} q_i$ . Only the region  $-T/2 < z < T$  as illustrated in figure 4.4 is considered. These charge fractions are inspired by the fact that in an ideal capacitor with infinite electrodes a charge  $q_i$  drifting from  $z_i$  to the electrode  $S$  will induce a net signal proportional to  $\frac{\frac{T}{2} - z_i}{T}$  on  $S$ , and vice-versa, the drift to electrode  $B$  will induce a net signal proportional to  $\frac{z_i + \frac{T}{2}}{T}$  on electrode  $S$ . As diffusion will happen independently for electrons and holes in the detector, a displacement of the charges reflecting the diffusion is generated independently for the two fractions  $q_{i,1}$  and  $q_{i,2}$ . Each charge fraction is displaced from its original

---

<sup>2</sup>The above described model of the induced signal for a single charge is valid for any field configuration

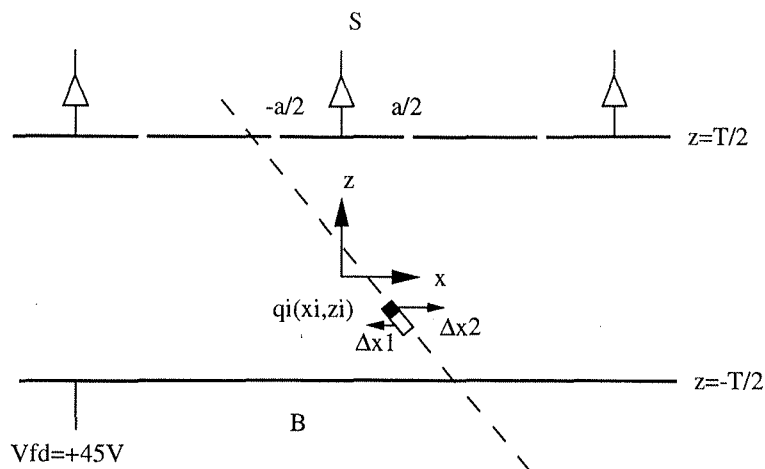


Figure 4.4: Simulation of charge segments in the detector bulk.

position  $x_i$  by a gaussian distributed random distance  $\Delta x$  with a standard deviation of

$$\begin{aligned} \sigma_1(z_i) &= \sqrt{2 \frac{D_h}{\mu_h} \frac{(T/2 - z_i)T}{V_{fd}}} & \text{for } q_{i,1} \\ \sigma_2(z_i) &= \sqrt{2 \frac{D_e}{\mu_e} \frac{(z_i + T/2)T}{V_{fd}}} & \text{for } q_{i,2} \end{aligned} \quad (4.4)$$

where  $\frac{D_h}{\mu_h} = \frac{D_e}{\mu_e} = 0.026V$  denotes the ratio of diffusivity and mobility.

In the signal collection phase the final signal on each strip  $S$  is regarded as the sum of all charge fractions for all segments within the acceptance of this strip, i.e. a strip pitch of  $a = 100\mu\text{m}$ . Figure 4.5 shows the deposited charge distribution projected on the plane  $z = 0$  for different track angles. The gaussian smearing of the distribution edges is due to the simulated diffusion. All curves are normalised to their integral. For a direct comparison of the absolute values see figure 4.2

To calculate the final output signal for a configuration like the VFT ministrip detector with one intermediate strip, the charge coupling between intermediate strip and readout strip has to be respected. Every other strip is regard as a readout strip where the final signal is measured. The signal of the readout strip consists of the the signal directly deposited on it plus the fraction of charge coupled from the adjacent intermediate strips to it. From the SPICE simulation carried out previously for this detector network (figure 3.11) it is assumed that 37.5% of charge from the intermediate strip is coupled to each adjacent readout strip. This implies that 25% of the signal from intermediate strips is lost. A direct coupling between readout strips is neglected.

For a final comparison with measurement data, a constant “gain” is applied to the signal on the readout strips. The value for this simulation gain has been adjusted so that the simulation yields the same average signal as measured for perpendicular track at the centre of one readout strip, i.e.  $x = 0, \alpha = 0$ . No further adjustments were made to the signal simulated at other positions or different track angles.

## Results of testbeam measurements

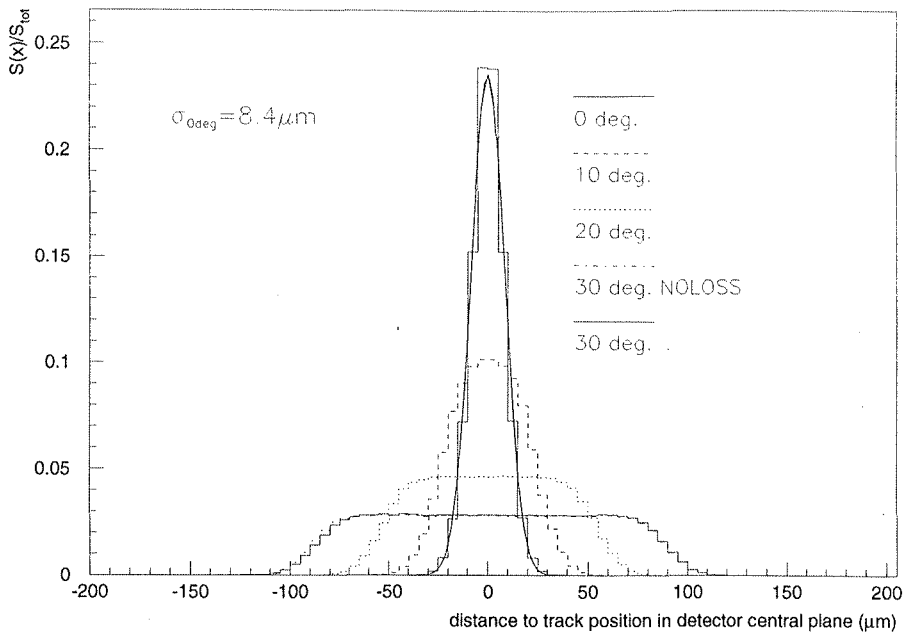


Figure 4.5: Simulated charge distribution projected to the detector central plane for different track angles.

Using testbeam data it was possible to precisely measure the single readout strip signal in dependence of the hit position on the detector for various track angles. The aim of the measurement is to determine the correlation of the readout strip signal and the track position with respect to the strip centres. With this measurement the influence of diffusion, track inclination and capacitive coupling can be studied and provides important information for their later use in the position calculation.

After the alignment of the test detector with respect to the reference system, the correlation between strip signal and hit position is measured. This is done by plotting the signal of a given readout strip versus the distance of the track in the detector central plane ( $z = 0$ ) to the centre of the readout strip. The track distance to the strip centre is obtained from an extrapolation of the track reconstructed in the reference system. The average readout strip signal versus the track distance to the strip centre for track angles from  $0^\circ$  to  $30^\circ$  appears on the left hand side of figure 4.6. The crosses represent the measurements and the solid line the results of the simulation. The simulation is in excellent agreement with the data. On the right hand side the same correlation is shown as a scatter plot, from which the effect of the landau tail on the signal average can be estimated.

For perpendicular tracks the signal correlation shows a step-like behaviour. If the track traverses the detector in a region of about  $\pm 40\mu\text{m}$  around the strip centre, the entire signal is collected on the readout strip. If the track is displaced by  $100\mu\text{m}$  to the centre of the intermediate strip the signal on the readout strip is about 37% of the signal on the readout strip. The measured data agree nicely with the simulation values obtained from the SPICE simulation. The signal on the readout strip is roughly independent of

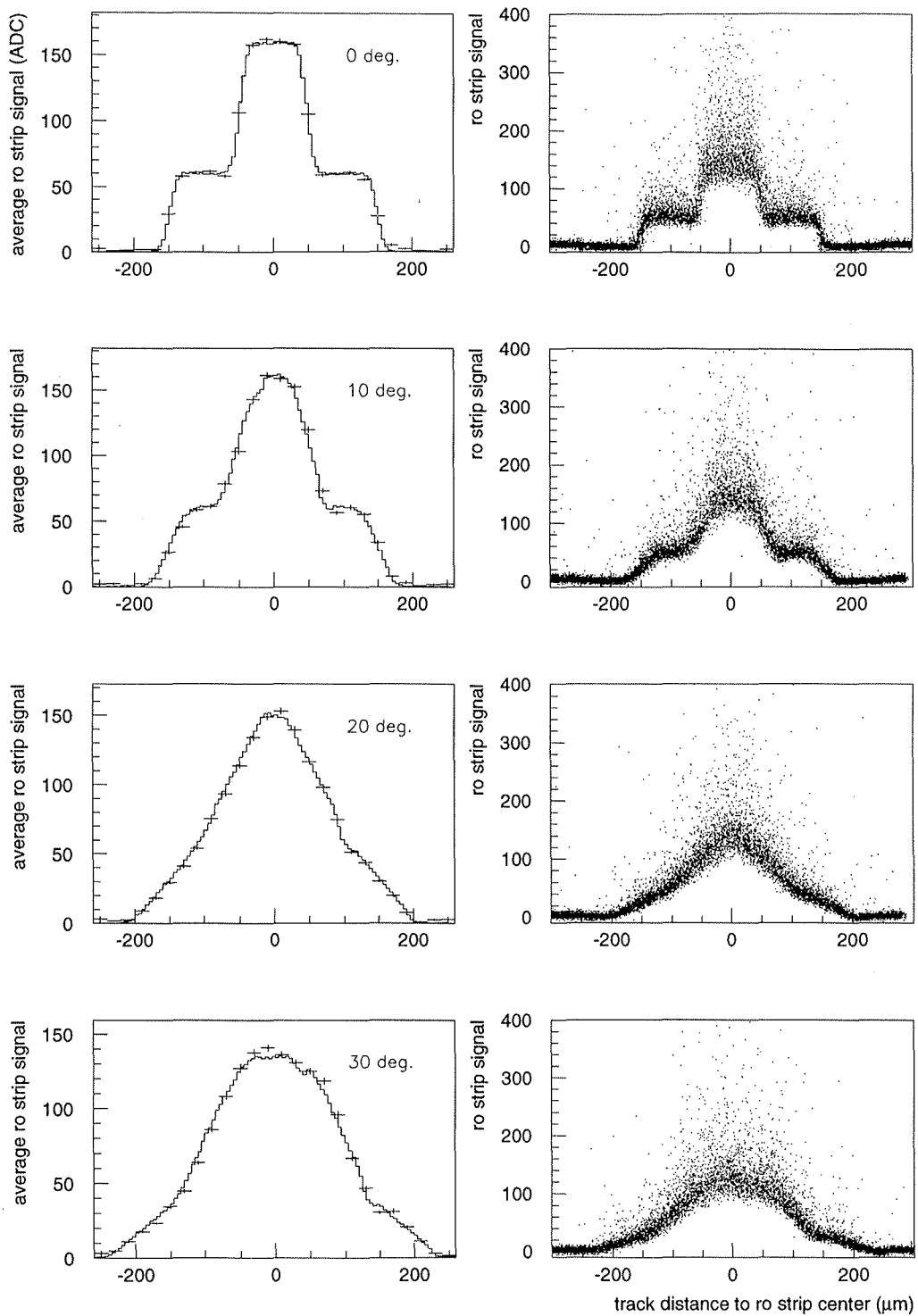


Figure 4.6: Readout strip signal as a function of the track distance to the strip centre in the detector middle plane. On the left side the average signal measured (crosses) is compared to the simulation results. On the right side the testbeam measurements are displayed as scatter plots.

the hit position if the track falls in a region of  $\pm 40\mu\text{m}$  around any strip centre. In a small region between the strips the signal response is altered by diffusion. In that region the signal strongly depends on the precise position of the track, an information used later for precise position reconstruction. The width of this diffusion dominated region is measured to be about  $20\mu\text{m}$ , which nicely agrees with the FWHM of the simulated charge cloud at  $0^\circ$  in figure 4.5. For perpendicular tracks, the signal response is symmetric around the readout strip centre.

When the incident angle is increased to  $\alpha = 10^\circ$ , the region where the readout strip is not independent of the hit position becomes larger. The charge is partially deposited below the readout strip and the intermediate strip. Consequently the region of constant response around the strip centres at  $x = 0, x = \pm 100\mu\text{m}$  is reduced.

At  $\alpha = 20^\circ$  a nearly linear correlation between hit position and signal response is measured. At this track angle, the step-like correlation for perpendicular tracks due to the large strip pitch is nearly fully compensated by the charge sharing between readout and intermediate strip. Therefore the signals measured can be used for a preciser reconstruction of the hit position than for perpendicular tracks. The top of the distribution at  $x = 0$  is smeared out by diffusion. In the range of  $\alpha = 0^\circ$  to  $\alpha = 20^\circ$  the entire signal is collected on two strips only. This is coherent with the measurements where the total cluster signal is reconstructed with the help of the track prediction (figure 4.2a).

If the track angle is further increased to  $\alpha = 30^\circ$  a nearly constant region at  $x = 0$  develops again. This is due to the fact that tracks traversing the detector in this region deposit a constant amount of charge in the acceptance of the readout strip. Equal fractions of charge will be deposited on right and left intermediate strip. These fractions are capacitively coupled to the next readout strips. Therefore at  $\alpha = 30^\circ$  the signal will be measured on three readout strips for tracks near  $x = 0$ .

On the plots for  $\alpha = 10^\circ, 20^\circ, 30^\circ$  a clear asymmetry around the strip centre is observed. This asymmetry cannot be explained by diffusion. A successful way of description is achieved in the simulation by introducing a small insensitive volume in the detector bulk. Charge deposited in this volume, located below the strip surface between the implants (see figure 4.8) is not transferred to the electrodes fast enough to contribute to the signal. Two effects may be responsible for the existence of such an insensitive volume:

- Charge deposited in this volume might be trapped at the oxide-bulk interface and therefore does not contribute to the total signal with its drift.
- The electric field lines in this volume may terminate rather on the oxide charges between the strips than on the implants. The deposited charge will only slowly move towards the electrodes. This results in a long tail of the induced current signal that is not sufficiently integrated by the charge amplifier.

In the simulation the cross section of this not to the signal contributing volume is arbitrarily chosen square. The size used in the simulation is determined to match the asymmetry at  $30^\circ$  at the readout strip centre. The same volume is able to describe the small asymmetries observed in the region of the intermediate strip at this angle. Furthermore it describes the smaller asymmetries being observed at the other track angles. At  $30^\circ$ , tracks at  $x \approx -50\mu\text{m}$  will fall completely outside all not contributing regions, whereas a track at  $x \approx +50\mu\text{m}$  will lay with its end on the strip side in this region and

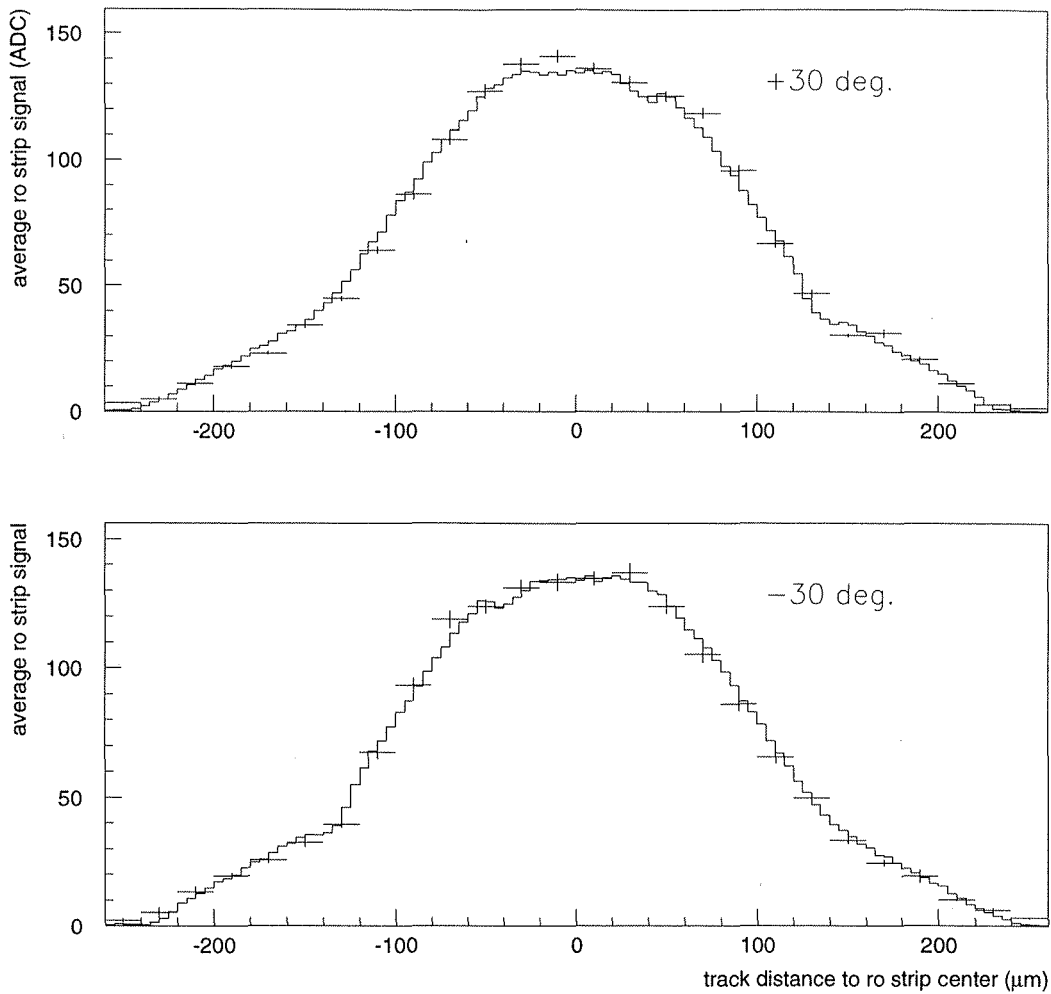


Figure 4.7: Average signal versus hit position for testbeam data recorded at  $\alpha = 30^\circ$  and  $\alpha = -30^\circ$ . The crosses mark the measurement data and the solid line the results of the simulation.

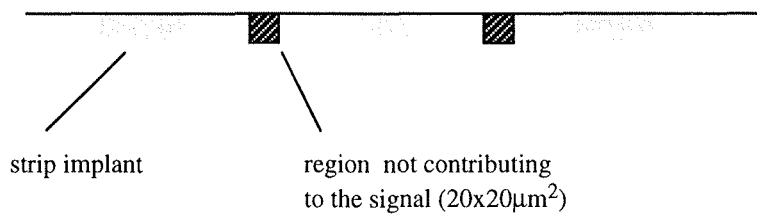


Figure 4.8: Implementation of a region not contributing to the signal in the simulation.

thus less signal will be recorded. A nice periodicity with the strip pitch is observed in the asymmetries.

The existence of a descret, not contributing region is supported by the fact that the asymmetry should move to the other side of the readout strip centre if the sign of the angle is inverted. To cross-check this hypothesis, data at  $\alpha = -30^\circ$  have been recorded and compared to the measurements at  $\alpha = 30^\circ$ . The test detector has been rotated in the setup to  $\alpha = -30^\circ$ , no changes were made to the electronics and analysis, in particular the readout direction. The results are compared in figure 4.7. Nicely the inversion  $S(x, \alpha) = S(-x, -\alpha)$  can be seen supporting the hypotheses of a dead region between the strip implants. An additional way of explanation can be an equal charge sharing between the strips of the charge deposited in the volume between. To describe the asymmetry the volume is required to be wider than the assumed  $20\mu\text{m}$ . Contrary to the other two hypotheses no charge would be lost and the full cluster signal maintained in this case.

### 4.1.3 Position reconstruction at different track angles

To reconstruct the hit position from the measured signals the  $\eta$  algorithm introduced in section (3.4) is used.  $\eta$  is calculated from the highest and second highest signal found in a cluster search with thresholds  $C_s = 2.5$  and  $C_c = 2.5$  on the VFT detector. For the analysis events are chosen, where the hit position on the test detector is within the acceptance area of the detector and not on dead or noisy strips. Furthermore events with two or more tracks reconstructed in the telescope are rejected. The cluster found on the test detector closest to predicted hit position is used for the analysis.

As the  $\eta$ -algorithm is based on two single strip signal, it is instructive to see the correlation between the single strip signals left and right to the track. Figure 4.9 illustrates the strip signals left and right of the predicted hit position on the measured detector for four different track angles. For perpendicular tracks three distinct regions are observed. When the track is in the acceptance of one readout strip the entire signal is measured on this strip and the other only contains random noise fluctuations. Hits on the intermediate strip result in equal signals on both strips. The tails towards high signal values are due to  $\delta$ -rays. In these three regions the detector exhibits a “digital” behaviour: the signal is either entirely contained on one readout strip or equally shared between two. Only few events give an increasing signal on one strip while the other strip signal decreases. These events correspond to hits between intermediate and readout strip. Their signal correlation is mainly determined by diffusion.

With increasing track angle these distinct regions disappear and a high signal on one strip is accompanied by a low signal on the other readout strip. The signal correlation for more inclined tracks is dominated by the circumstance that the signal is partially deposited below two implants.

The digital behaviour for perpendicular tracks is well reproduced in the distribution of  $\eta$  displayed in figure 4.10. On the left side the figure shows the distribution of  $\eta$  and on the right side its integral  $F(\eta)$  as it is used to calculate the hit position from the two strip signals.

The three classes of events from plot 4.9a correspond to the peaks at  $\eta = 0, 0.5, 1$ . At



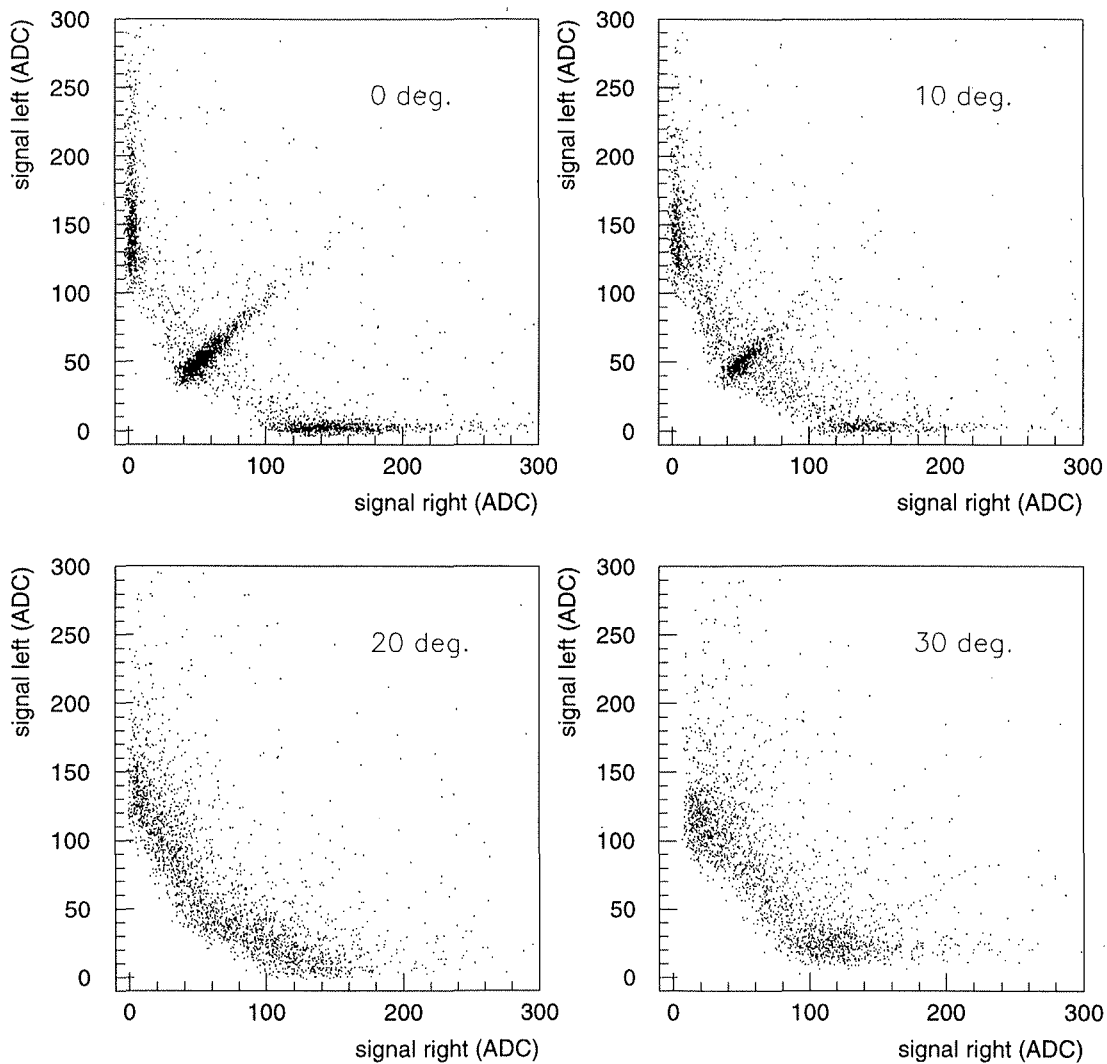


Figure 4.9: Readout strip signals left and right to the predicted hit position for different track angles.

10° the fraction of events between the peaks is already enhanced as parts of the tracks come to fall in the interface region between readout and intermediate strip. This also leads to an increased dependence of the calculated position on the measured  $\eta$  in the region between  $\eta = 0.1$  and  $\eta = 0.4$ . At 20° the  $\eta$  distribution is nearly constant. The response of a single readout strip in case of  $\alpha=30^\circ$  for tracks close to the strip centre does not strongly depend on the hit position (figure 4.6). The fraction of events with high signal on one strip and low signal on the other are enhanced. Due to the fact that the charge is measured on two or more strips, no events with  $\eta = 0$  or 1 are recorded at  $\alpha=30^\circ$ .

To illustrate the dependence of  $\eta$  on the hit position between the strips,  $\eta$  is plotted in figure 4.11 versus the predicted hit position in the detector central plane. The prediction is obtained from the track reconstructed in the testbeam reference telescope.  $\eta$  is calculated from the highest and second highest strip in the clusters found by the cluster search with thresholds. No prediction is used in the determination of  $\eta$ .

Tracks next to the strip centre of both intermediate and readout strip lead to a constant  $\eta$  for perpendicular tracks. Noise fluctuations on the strips next to the highest strip in the cluster can cause a wrong assignment of left and right strips resulting in the groups of events at prediction 0 and  $\eta = 1$  and vice-versa. When the track angles is increased the region of events with constant  $\eta$  decreases. At  $\alpha=20^\circ$  the correlation between  $\eta$  and the hit position is nearly linear. At all angles the measured correlation between hit position and  $\eta$  is well reproduced by the  $\eta$ -algorithm shown as a solid line.

#### 4.1.4 Spatial resolution at different track angles

The spatial resolution of the VFT ministrip detector is determined by means of the residual distribution formed by predicted and calculated hit position in the detector central plane.

Special attention is given to the alignment of reference and test detectors. Any misalignment both in translation and rotation would result in a wider and non-centred residual distribution. At all different track angles the detectors are aligned individually. The intrinsic resolution of the VFT detector is given by the variance of the residual distribution minus the squared error of prediction. As the error on the prediction is about  $1\mu\text{m}$  its contribution to the variance of the residual is further on neglected and only the variance of the residual is given.

Figure 4.12 displays the residual distribution measured at different track angles. Between  $\alpha = 0^\circ$  and  $\alpha = 15^\circ$  the distributions clearly exhibit two different contributions with a large and a small variance respectively. The residual distribution reflects a mixture distribution, which is fitted by the sum of two gaussian distributions. Furthermore it has to be considered, that the error on the hit position depends on the hit position itself. The intrinsic resolution is then given by the weighted sum of the two standard deviations as

$$\begin{aligned}\sigma^2 &= w_1\sigma_1^2 + w_2\sigma_2^2 \\ w_i &= \frac{\sigma_i f(\mu_i)}{\sum_{i=1}^2 \sigma_i f(\mu_i)}\end{aligned}\tag{4.5}$$

where  $\mu_i$  denotes the mean value, 0 in our case, and  $f(\mu_i)$  is the function value of the each gaussian distribution at its mean.

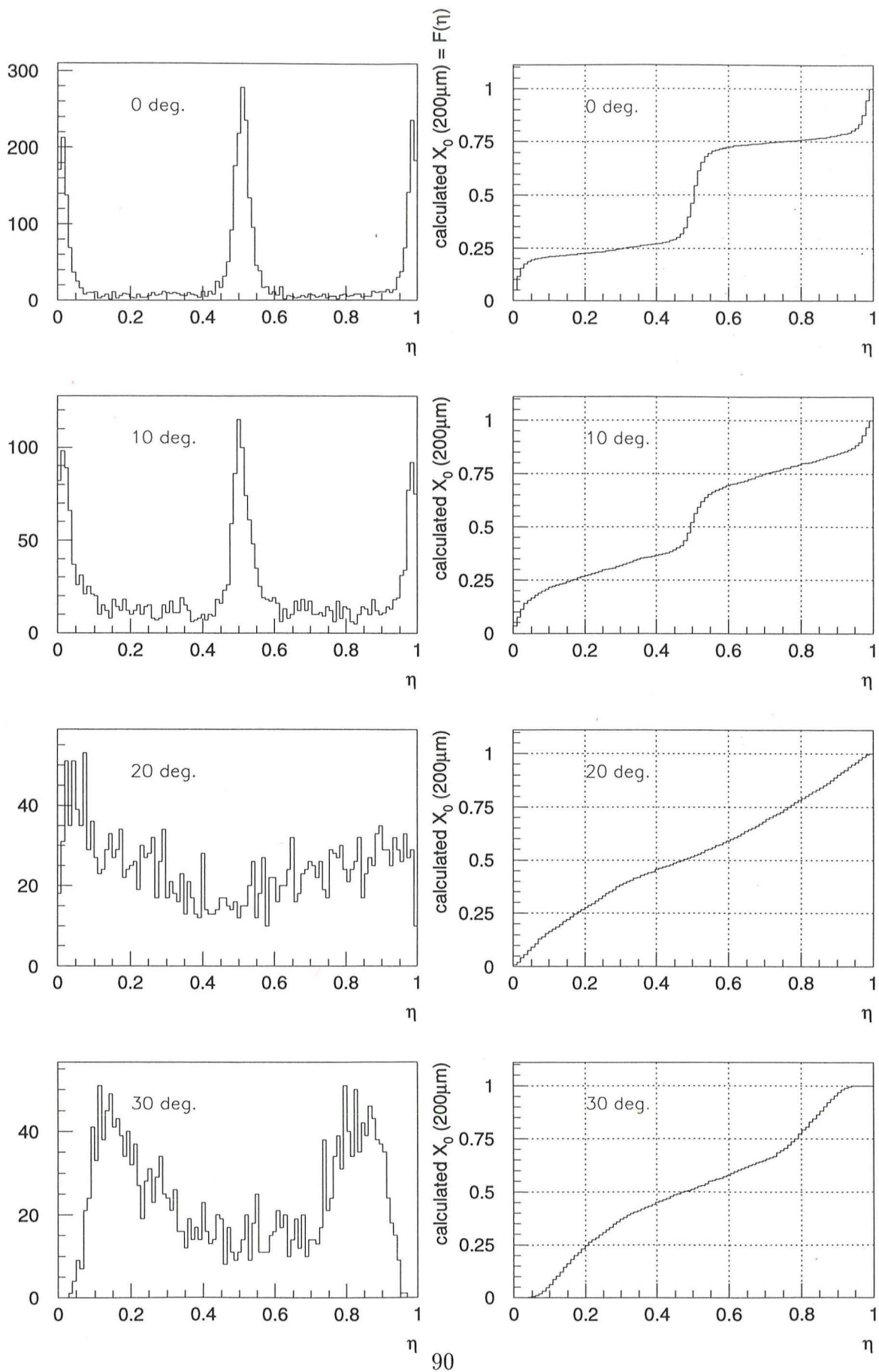


Figure 4.10: Distribution of  $\eta$  and its integral at different track angles.

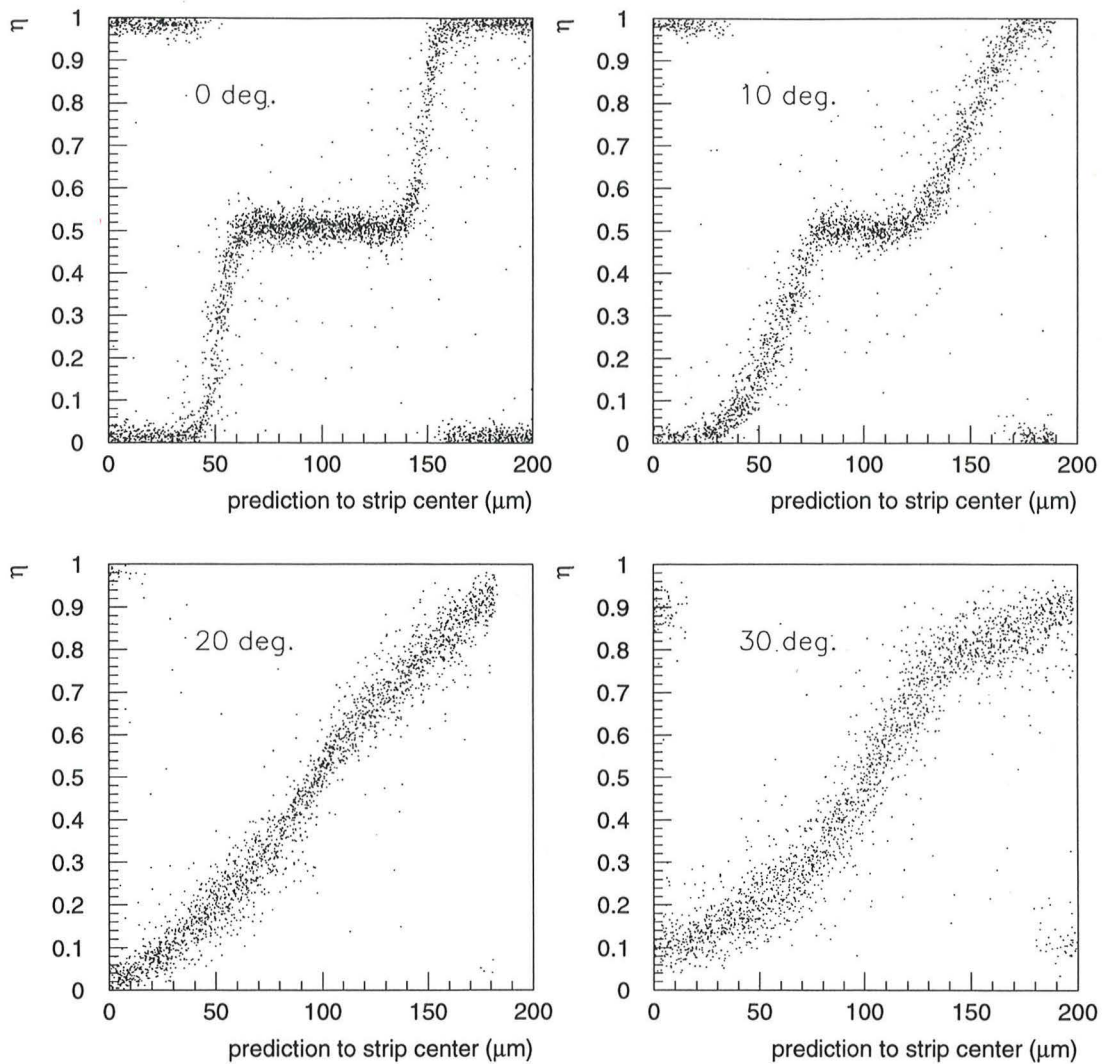


Figure 4.11: Measured correlation between  $\eta$  and the hit position predicted by the track reconstruction. Noise fluctuations lead to ambiguities in the assignment of left and right strip if the hit is next to the readout centre.

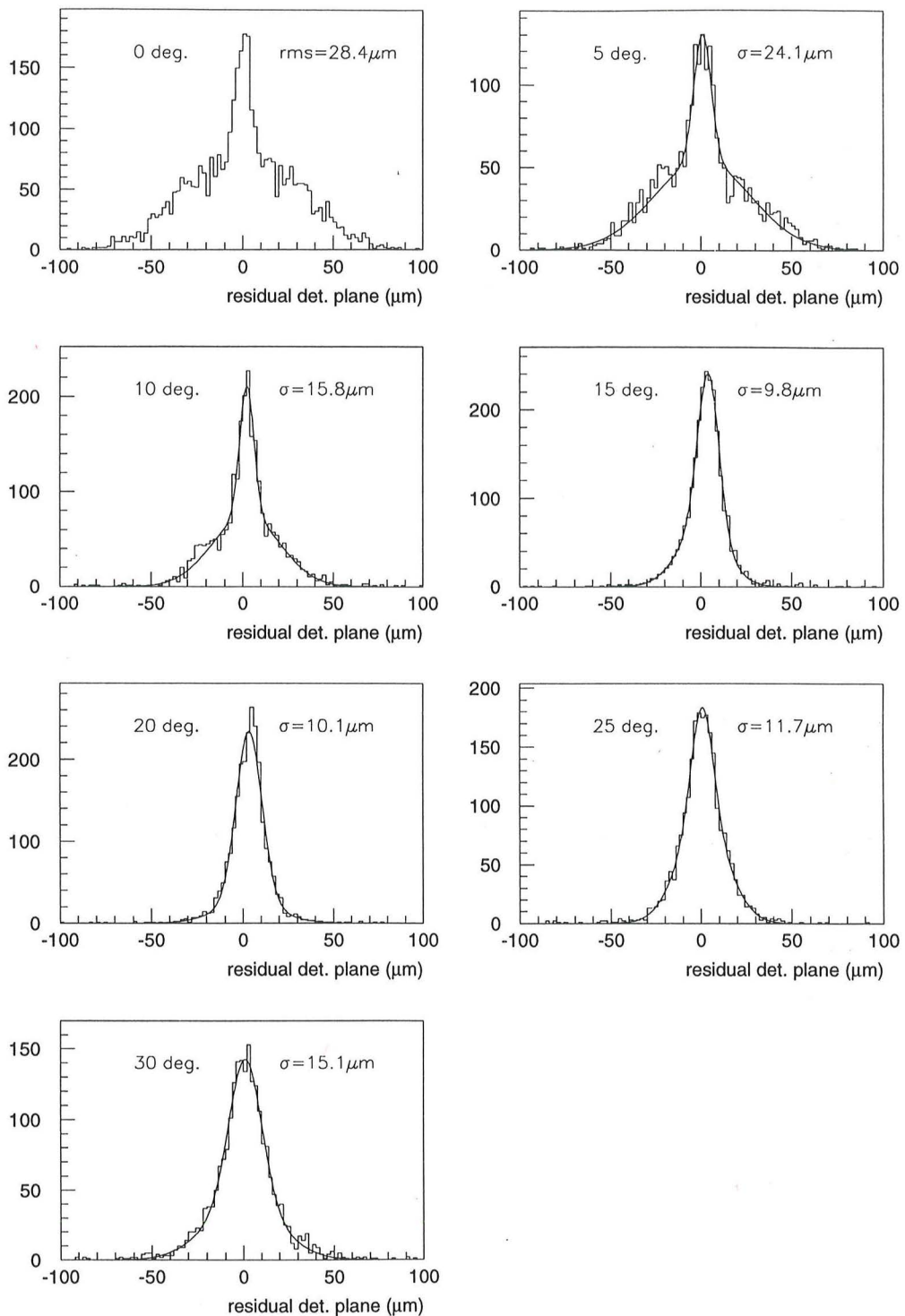


Figure 4.12: Residual distribution at different track angles for the VFT ministrip detector.

With increasing track angle the shoulders in the residual distribution diminish. This results in an overall improved intrinsic resolution of the detector. The optimum resolution is achieved for a track inclination of about  $15^\circ$  to  $20^\circ$ . Considering the detector arrangement in the DELPHI Very Forward Tracker a spatial resolution of about  $28\mu\text{m}$  in the detector plane is expected for the plaquette measuring the  $\phi$ -coordinate. The inclination angle on this plaquette relative to the strip axis varies between  $0^\circ$  and  $5^\circ$ . For the other plaquette giving the  $\theta$  coordinate in DELPHI the inclination angle is in the range of  $20^\circ$  to  $30^\circ$  and thus an intrinsic detector resolution of  $12\mu\text{m}$  can be expected. For both plaquettes the measured intrinsic resolution is significantly better than the demanded resolution of  $70\mu\text{m}$ .

To cross-check the results of the testbeam data analysis events have been simulated using the simulation presented above for the signal correlation. For each inclination angle a set of 10000 tracks is used for a comparison to the testbeam results. For each track, signals on the readout strips are simulated and a random noise added to the single strip signal. The r.m.s. noise in the simulation is chosen such that the most probable value of the simulated cluster S/N distribution is equal to the measured value for  $\alpha = 0^\circ$ , i.e. about 55. The noise value was not altered for simulation of other track angles. The same thresholds as in the testbeam analysis are used for the cluster finding in the simulation. The position is reconstructed using the  $\eta$ -algorithm where the simulated  $\eta$  distribution is used to determine  $F(\eta)$ . The residual distribution is again fitted by the sum of 2 Gaussian distributions. Figure 4.13 shows the intrinsic spatial resolution in the detector plane versus the track angle. The testbeam data are presented as solid markers, while the line shows the result of the simulation. The coherence between data and simulation is good as the shape and variance of the residual distribution are nicely reproduced by the simulation for all different track angles. A substantial improvement of the spatial resolution is observed between  $5^\circ$  and  $15^\circ$ .

The angle dependence of the spatial resolution results from changes of the correlation between hit position and measured  $\eta$ . Using the  $\eta$ -algorithm for position interpolation, the error on the reconstructed coordinate depends on layout parameters like the readout pitch  $\Delta$  or the number of intermediate strips, reflected by the function  $f(\eta)$ , and the signal-to-noise performance of the detector-electronic system. From figure 4.10 it becomes clear that a given fluctuation in  $\eta$  due to random noise fluctuation results in a large position error for large slopes of  $F(\eta)$ . Thus, for perpendicular tracks, one expects for events with  $\eta$  close to 0, 0.5 or 1 a worse resolution than for hits in the diffusion dominated region between the implants, for which  $\eta$  lays between the peaks. The overall best resolution can be expected for track angles of about  $20^\circ$ , where the correlation between hit position and  $\eta$  is nearly linear. To illustrate the above on data figure 4.14 shows the residual versus  $\eta$  for  $0^\circ$ ,  $10^\circ$ ,  $20^\circ$  and  $30^\circ$ . The shoulders in the residual distribution for perpendicular tracks are due to events under or close to the strip implant. With increasing track angle, the charge splitting between two strips due to the track angle causes an improvement of the resolution.

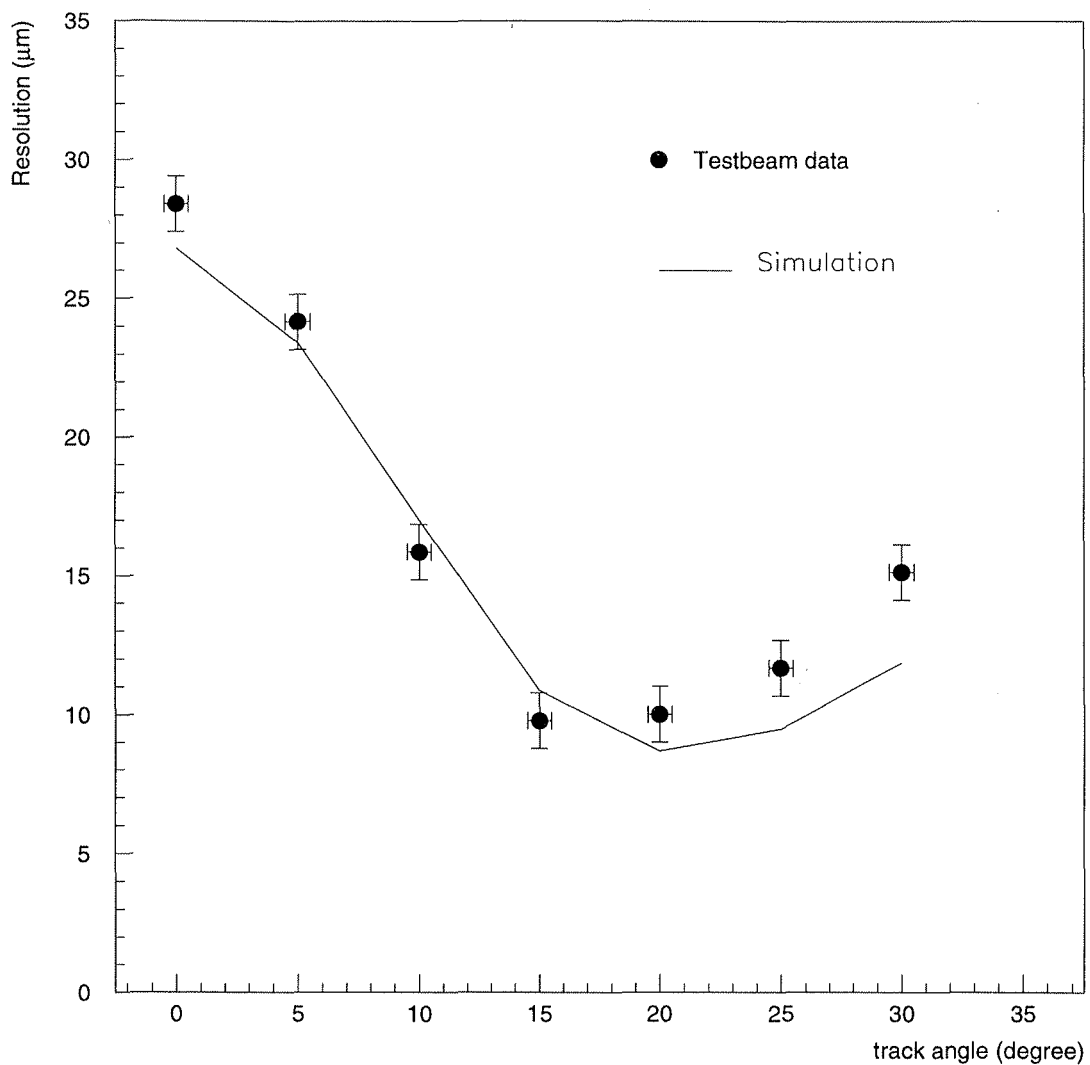


Figure 4.13: Intrinsic detector resolution in the detector plane versus the track angle  $\alpha$ . Test beam results are displayed as markers while the solid line presents the simulation results.

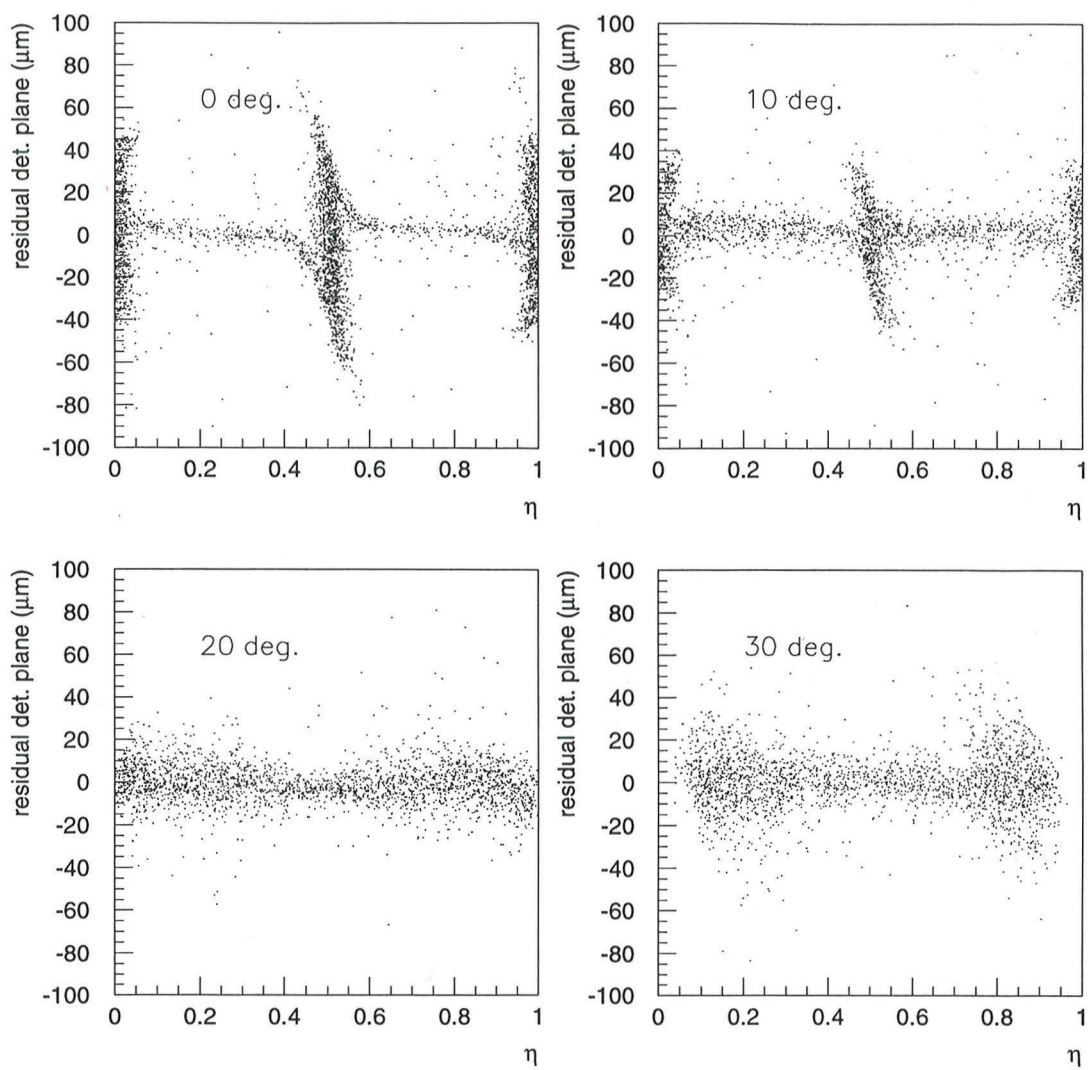


Figure 4.14: Measured residual versus  $\eta$  for different track angles .



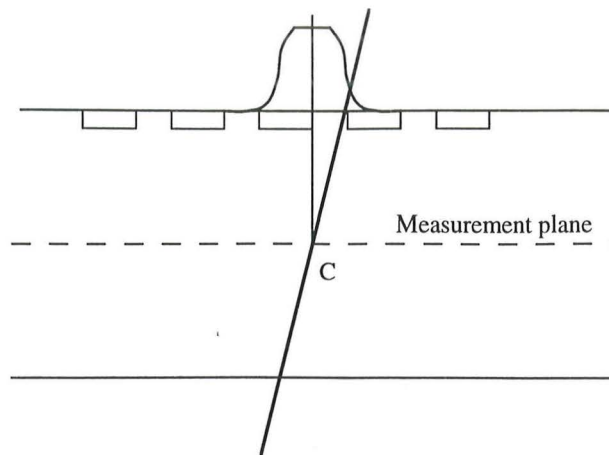


Figure 4.15: Definition of the measurement plane.

## 4.2 Contributions to the measured spatial resolution

In this section parameters and effects influencing the spatial resolution shall be discussed. Effects inherently present in the detectors like diffusion,  $\delta$ -rays or charge loss as well as external parameters like electronic thresholds, track angle or gain variations of the electronic may have an influence on the resolution or can create systematic errors in the position reconstruction.

As the detector is a planar device measuring the track intersection in one coordinate, one needs to define the plane in which this coordinate is measured, i.e. the measurement plane. In practice this plane will lay parallel to the strip plane in the bulk. Due to the fact that the VFT ministrip module consists of two independent detector plaquettes the two coordinates within one module will be measured in two different planes. This fact has to be taken into account in the track reconstruction as the planes will have different  $z$  positions in DELPHI and therefore require separate treatment. The precise knowledge of the measurement plane position with respect to the strip plane is desirable since only the strip plane can be measured during the mechanical survey of the module positions.

The position reconstruction in silicon detectors is based on the reconstruction of the centre of gravity of the charge cloud projected on the strip plane. If the charge cloud is symmetric around its mean value and its measurement does not introduce any asymmetry, the intercept of its centre with the track will yield the detector central plane as the effective measurement plane. This is schematically illustrated in figure 4.15. If the deposited charge is asymmetric around the track or the signal measurement does not maintain the symmetry, the reconstructed centre and consequently the measurement plane will shift.

The signal functions at different track angles as seen in figure 4.6 prove to be nearly symmetric around the readout strip centre for a measurement plane in the detector centre. They reflect the charge collection process as well as its measurement. The residual distribution as produced by the simulation, where the detector central plane is used, appear to be centred for all track angles. Furthermore the periodicity in the asymmetries support the assumption of a central measurement plane. No shift of the measurement plane with respect to the track angles is observed. A possible dependence of the measurement plane on the incident angle is, as long as it is small, of minor importance in DELPHI as the

angle variations on the VFT modules is limited to  $\pm 3^\circ$  around the average angle. Any possible overall shift will be absorbed in the alignment of the detector crowns.

To detect relative shifts of the measurement plane from an overall effective measurement plane the residual distribution can be used. It has to be stated that during the alignment of the detectors their effective measurement plane is used, regardless of its distance to the strip plane, as the alignment is based on centering the residual distribution.

#### 4.2.1 Spatial resolution as a function of the interstrip position

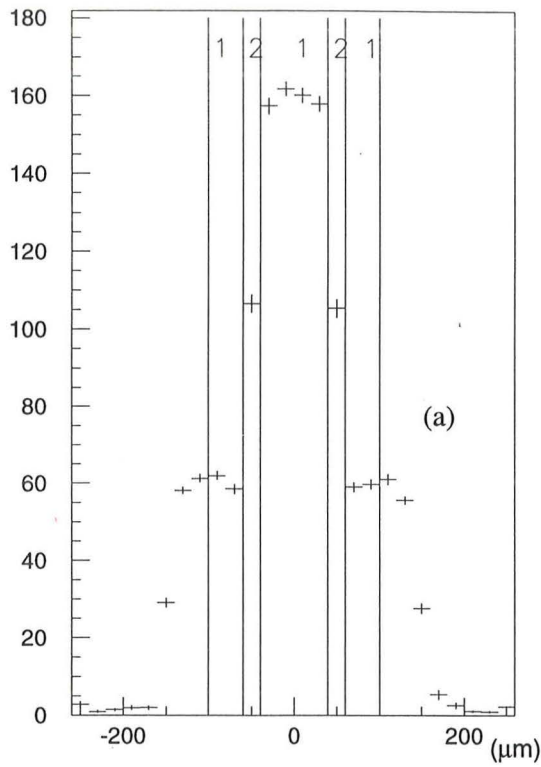
The intrinsic detector resolution is not constant for all regions between the strips as it shown earlier in figure 4.12. Figure 4.14 illustrates the fact, that the residual distribution has various components with variances and weights, which are connected with separate regions of  $\eta$ . Each value of  $\eta$  is related to a certain space region between the readout strips. Likewise, the resolution can be determined in dependence of the hit position between the strips. To do so, different regions between the readout strips are selected, which are presented in figure 4.16a and 4.16b. The plots show the average readout strip signal in dependence of the hit position for  $0^\circ$  and  $30^\circ$  incident angle. The choice of the regions is motivated by the different slopes of the curves, which in turn translate to different sections of  $F(\eta)$ .

For perpendicular tracks, plots c and d show the residual distribution for the two regions. The “box” like shape of the residual distribution finds its cause in the fact that the signal response is constant in this region, thus the strip position is reproduced in the reconstruction. The resolution of 26 nicely corresponds to the region width divided by  $\sqrt{12}$  expected for this digital section. Region 2 corresponds to the interstrip region where the charge division is dominated by diffusion. The strong dependence of the signal response on the track position results in an excellent resolution of  $4.6\mu\text{m}$ . The fraction of events in this region is given by the diffusion width relative to the strip pitch and is, in our case, approximately 20% for the VFT detector. The overall resolution can be parametrised as

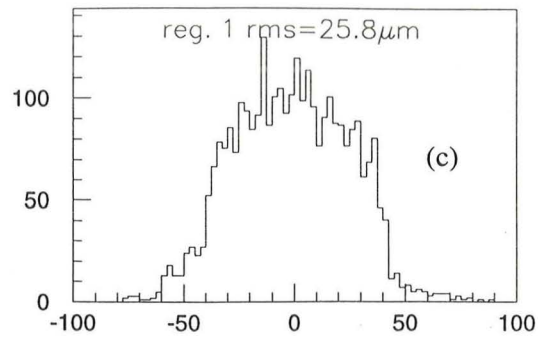
$$\sigma(\alpha = 0) = \sqrt{\frac{a^2}{12}w + \left(\frac{b^2}{\left(\frac{S}{N}\right)^2} + c^2\right)(1-w)} \quad (4.6)$$

where the first part stands for the digital section with  $a \approx 80\mu\text{m}$  being the width of the region.  $w$  denotes the fraction of events with digital resolution, which can be estimated to be  $\frac{a}{\Delta}$  in case of uniform irradiation. The second part consists of a S/N dependend part, where  $b$  is in the order of the diffusion dominated interface region between the implants, plus a constant contribution  $c$ .

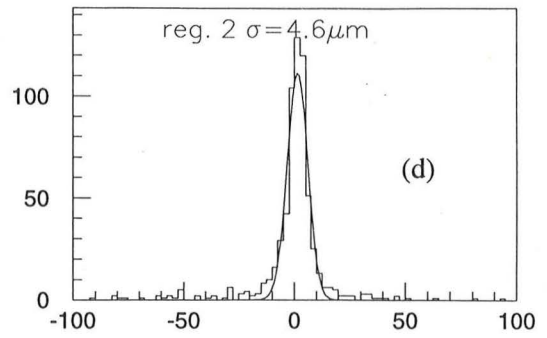
For  $30^\circ$  tracks the situation is different in so far as the signal response is never constant with changing hit positions. However, two regions with different slopes of the strip signal function can still be identified, which compare to different slopes of  $F(\eta)$  in figure 4.11. Each region covers 50% of the detector surface, where region 1 is centred around the readout strip and region 2 around the intermediate strip. The resolution around the readout strip (region 1) is  $14\mu\text{m}$ , region 2 gives an intrinsic resolution of  $9\mu\text{m}$ . Both residual distributions are centred at 0 pointing out that the measurement plane does not shift between the two regions.



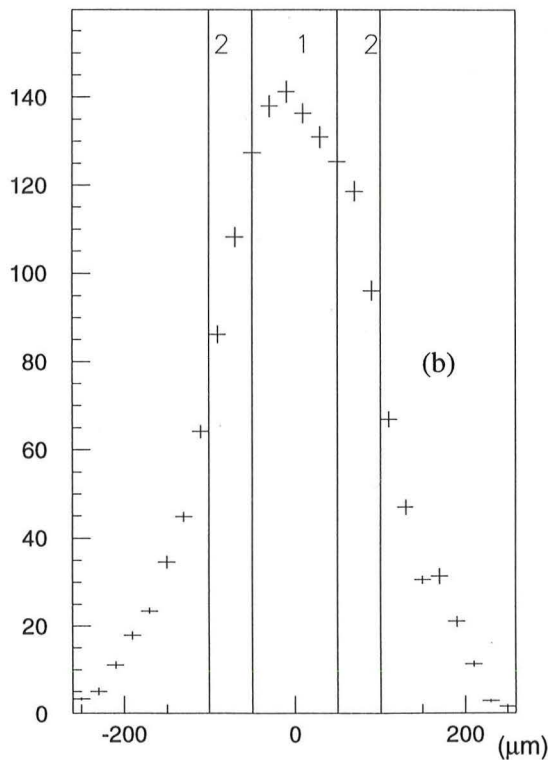
average readout str signal vs impact



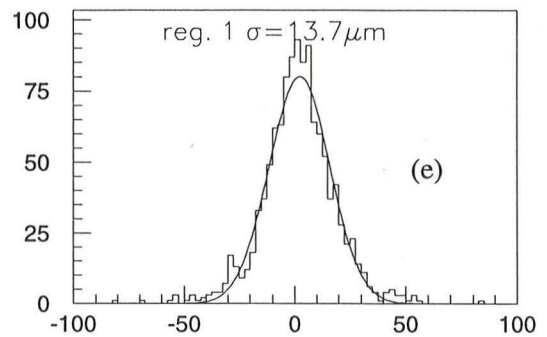
residual 0 deg. region 1



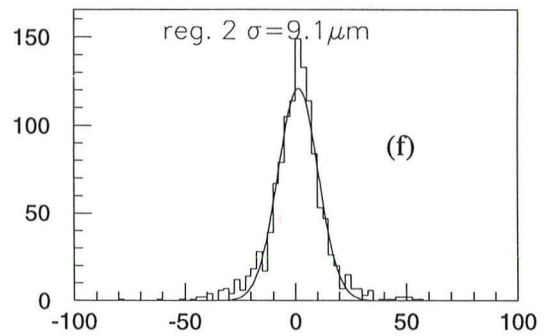
residual 0 deg. region 2



average readout str signal vs impact



residual 30 deg. region 1



residual 30 deg. region 2

Figure 4.16: Selection of regions between the readout strip centres and their corresponding  $\eta$  and residual distributions for perpendicular (a) and  $30^\circ$  (b) tracks.

## 4.2.2 Influence of signal loss

Two different sources of signal loss have been considered: The signal loss for hits on the intermediate strip is related to the working principle of capacitively coupled readout and has been measured directly.

Secondly the presence of a volume not contributing to the signal on the strip surface between the strip implants is strongly supported as it excellently reproduces the measured asymmetries in the readout strip signal function in figure 4.7. This asymmetry would indeed lead to a shift of the measurement plane if a common function  $F(\eta)$  is chosen for the reconstruction of data sets with different polarities of the track angle. In DELPHI this problem is overcome as the effect of asymmetry is corrected for by using the measured  $\eta$  distributions for  $\alpha = +30^\circ$  and  $\alpha = -30^\circ$ . For optimum position reconstruction in DELPHI two different functions  $F_{\alpha=+30}(\eta)$  and  $F_{\alpha=-30}(\eta)$  have to be used for plane Bottom MS1 and plane Bottom MS2 of the VFT ministrip detector. The simulation indicated no significant change of spatial resolution with and without the assumption of a region, not contributing to the signal.

Concerning shifts of the measurement plane the above said also applies for signal losses on the intermediate strips. Additionally, the signal loss on intermediate strips leads to a change of the  $\eta$  distribution. The change of  $F(\eta)$  is demonstrated in figure 4.17 for a track angle of  $\alpha = 30^\circ$ . The dots indicate the measured correlation, while the solid line gives the simulated correlation with 25% charge loss and the dashed curve displays the simulation result if no charge loss is present.

As long as both sources of signal loss are reflected in  $F(\eta)$ , they do not cause a systematic shift of the measurement plane.

## 4.2.3 Influence of $\delta$ -rays

The production of  $\delta$ -rays influences the intrinsic detector resolution, as it affects the deposited charge distribution in the silicon bulk. The  $\delta$ -ray trajectory results in deposition of charge off the incident particle trail and therefore displaces the charge centre of gravity. Consecutively the reconstructed position is shifted from the original particle track. The production probability of a  $\delta$ -ray with an energy higher than 60keV, corresponding to an electron practical range of  $56\mu\text{m}$ , along a  $300\mu\text{m}$  path in the silicon bulk, is 9% [44].

Events where a  $\delta$ -ray contributes additionally to the most probable energy loss can easily be selected in the measured signal distribution, as they are responsible for the tail in the Landau distribution. A selection cut is placed at 1.7 times the most probable signal, which corresponds to the most probable energy loss in  $300\mu\text{m}$  silicon (88keV) plus a deposited energy higher than 60keV due to the  $\delta$ -ray.

Figure 4.18 shows the measured signal distributions for perpendicular and  $30^\circ$  tracks with the selected tail events shaded. The selected events amount to approximately 8% of the total event sample. The central plots illustrate the residual distribution for events in the signal peak region, the right plots give the residual distribution for the tail events. For both track angles the variance of the residual distribution is  $28\mu\text{m}$  for events containing  $\delta$ -rays. In the case of perpendicular tracks the total variance is not altered significantly by tail events as the detector resolution is approximately the same. For  $30^\circ$  tracks the situation is different as the detector resolution is approximately  $13\mu\text{m}$ . At  $30^\circ$   $\delta$ -rays lead

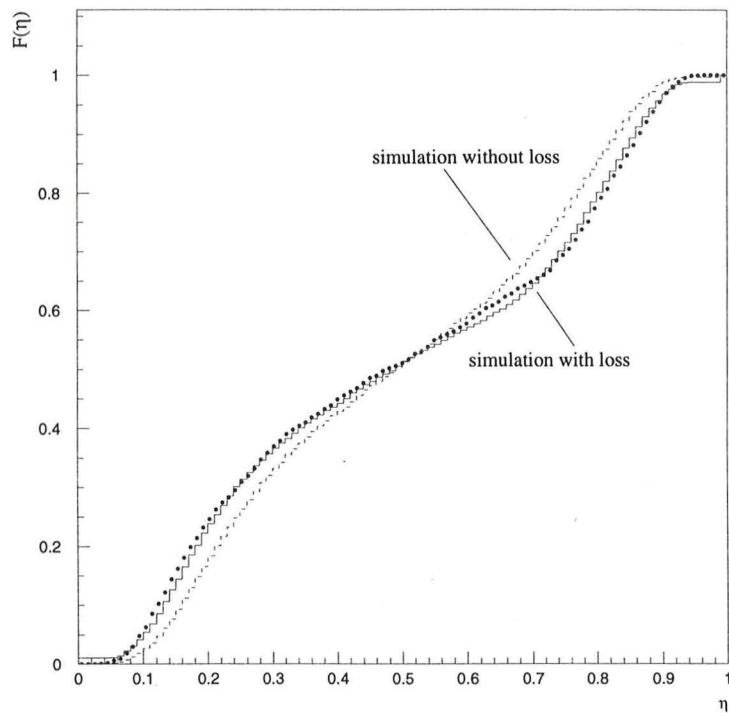


Figure 4.17: Integrated  $\eta$  distribution  $F(\eta)$  versus  $\eta$  for  $30^\circ$  tracks. The dots indicate the measured correlation, the solid line gives the simulation result with charge loss, the dashed line the simulation result without signal loss on the intermediate strip.

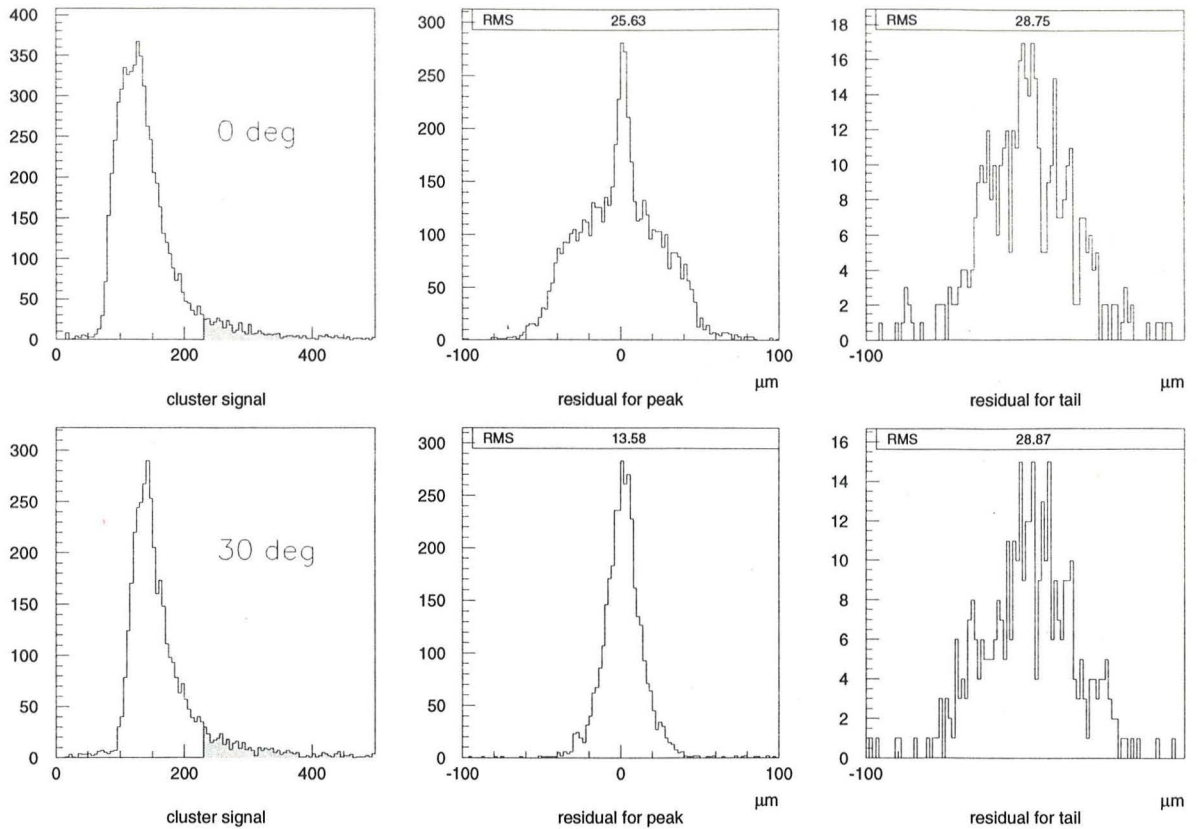


Figure 4.18: Signal distributions for perpendicular and  $30^\circ$  tracks with the selected  $\delta$ -ray events (shaded). The central and right plots show the residual distribution for the signal peak and tail region.

to a visible shift of the reconstructed hit position from the particle track. Events with  $\delta$ -rays constitute the tail of measured residual distribution at  $30^\circ$  track angle. Although the reconstructed position for a particular event is shifted, the total systematic shift is zero, since  $\delta$ -rays are uniformly distributed in azimuthal angle around the particle track.

# Chapter 5

## Production and Test of the VFT ministrip detector

This chapter will describe the production of the final VFT ministrip detector and tests carried out on it. The detector quality was monitored throughout the production and is completed by acceptance tests before the modules are mounted. Detailed tests of all components before the detector production are unavoidable as the failure of a single component will make one entire module unusable. One module consists of 2 silicon detectors, 2 BeO hybrids, two fan-in and 4 MX6 chips, and thus presents a substantial investment in money and time.

### 5.1 Production of the VFT ministrip detector

The detector chip is manufactured by Micron Semiconductor Ltd. on 4" high resistivity silicon wafers supplied by Wacker. Specifications of the detectors are listed in table 5.1. Prior to delivery, each detector is tested by Micron for leakage current on guard ring and detector active area, depletion voltage, punch-through voltage of the FOXFET biasing structure, breakdown voltage of the silicon dioxide layer and number of defect strips. To cross-check the results and detect faults on the individual plaquettes, crucial parameters like leakage current and depletion voltage are measured again after the detectors are delivered. The results of our measurements on the delivered detectors shall be summarised

Test	min	max
full depletion voltage $V_{fd}$		40V
punch through voltage of FOXFET bias structure at $V_{gate} = 0V$		15V
break down voltage of coupling capacitor	$V_{fd}$	
leakage current on bias line (drain) at $V_{fd} + 15V$		$3\mu A$
leakage current on guard ring at $V_{fd} + 15V$		$10\mu A$
Number of defect channels		5

Table 5.1: Specifications of detector parameters to Micron Semiconductor Ltd.

below. Each detector fulfilling the specifications is released for production and glued to one electronic hybrid in the first production step. Each top detector is equipped with one aluminium support ("ear") which is used for the detector support in the transport and test jigs as well as for its fixing on the final crowns. The hybrids are already equipped with two MX6 readout chips and a connector on one type of hybrid. On the so-called single-sided modules the fan-in is glued before all detector readout strips are bonded to it and from it to the readout chips. Once this step is completed, each single-sided module is tested with pulsed light source [45]. Light pulses from a diode emitting  $1\mu\text{s}$  pulses of 940nm wavelength are projected on each strip. A stereo microscope is used to focus the light on the detector strip side resulting in a light spot of  $10\mu\text{m}$  diameter. By this means each single-sided detector is tested for correct pedestal, noisy and dead strips as well as signal gain. Bonding faults on the detector, fan-in or readout chips are detected at this early stage and hence can be repaired.

After the tests on single-sided modules are completed, pairs of top and bottom detectors are formed. The single-sided detectors are glued together back to back on the aluminised n-side of the detector. To make the connection for the back plane of the detectors, a  $25\mu\text{m}$  thick aluminium bonding wire is glued with conductive glue between the detectors. The wire reaches out of the module and is connected to a pad on the hybrid surface. single-sided detectors are selected in a way that top and bottom detector have similar depletion and punch-through voltage so that they can be operated under the same conditions when the common backplane voltage is supplied. For gluing the so-called double sided modules, the two single-sided ones are aligned with respect to each other with a precision of  $20\mu\text{m}$ . At this stage the two detector sides are, apart from the backplane connection, still independent. To transmit the readout and control signals from the top to the bottom detector, the connections between bottom and top hybrid are made along one side of the module. A picture of a final detector module is displayed in figure 5.1.

Finally, the double-sided detectors are calibrated for their signal response and tested for dead channels and noise performance. In addition, the relative positions of the two plaquettes with respect to each other and with respect to two reference spheres on the bottom side of the module is measured on a 3D survey bench. This measurement gives starting values for the alignment of the detector with a precision of  $4\mu\text{m}$ . Each module is tested by three different methods - to be described later - before it is mounted on the crowns in groups of six modules. This extensive test of the individual modules is necessary as no manipulation or repair work is possible once the modules are mounted on the crown. As the detector modules are extremely fragile and have only very few areas, where they can be supported, a special machine was constructed to pick the detectors from their transport frames and move them on the crown with vacuum pens. This machine allows the positioning of the modules on the crowns with distances between the modules of less than 0.5 mm which is clearly impossible free handed. One final crown equipped with 6 detectors during the mounting phase is displayed in picture 5.2. Removable supports are fixed to the crown after the mounting to allow the manipulation of each crown. Once each crown is mounted, the detectors are connected to the repeater electronics via  $100\mu\text{m}$  thick kapton cables.

Every completed crown is tested again by means of calibration signals and  $\beta$ -source for accidental errors on modules, capton cables or repeater. Each module on the crown



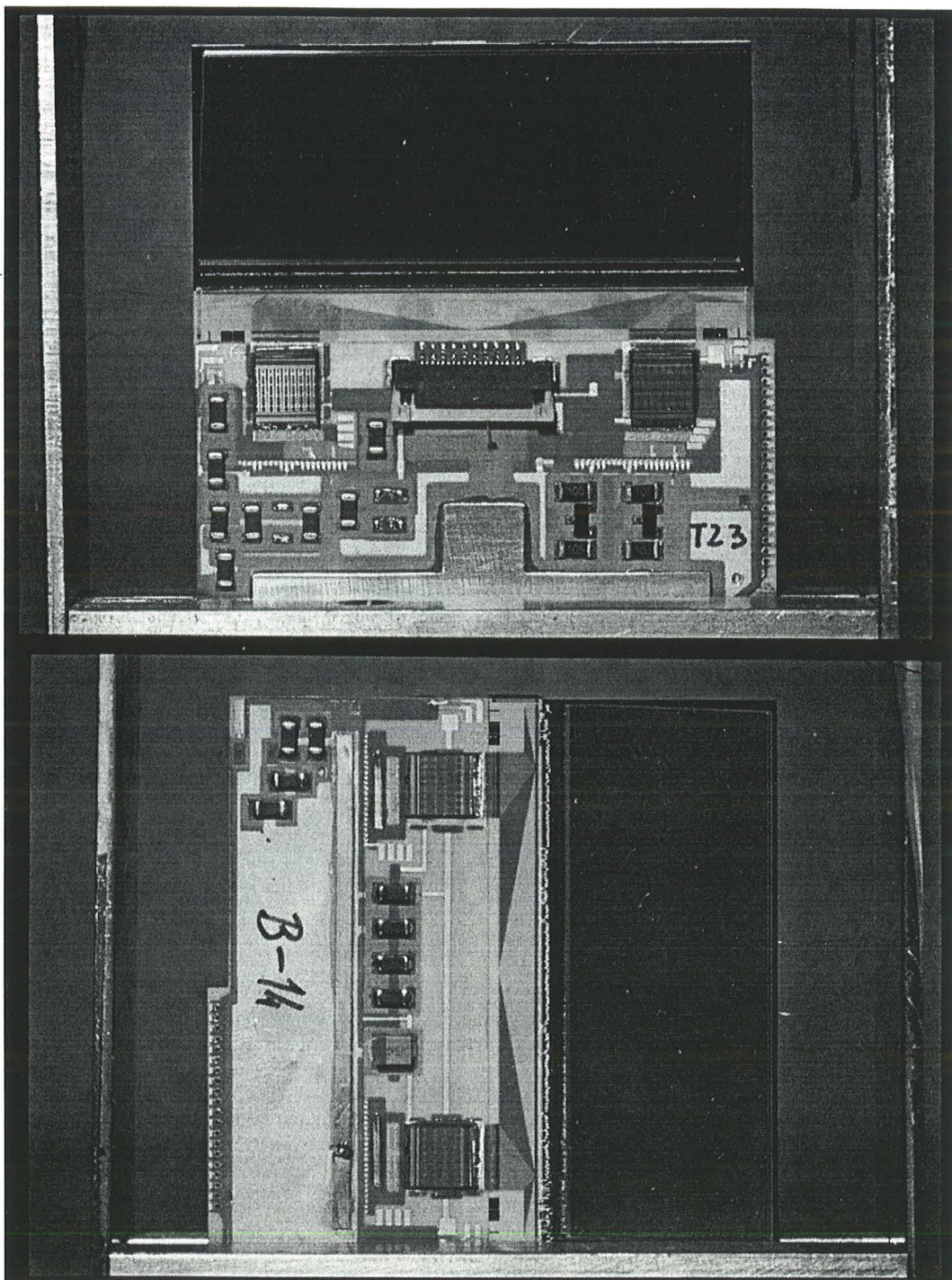


Figure 5.1: Picture of a VFT ministrip detector module in front and rear view.

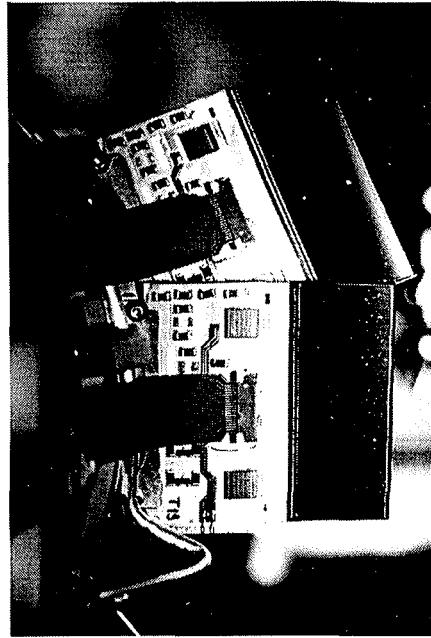
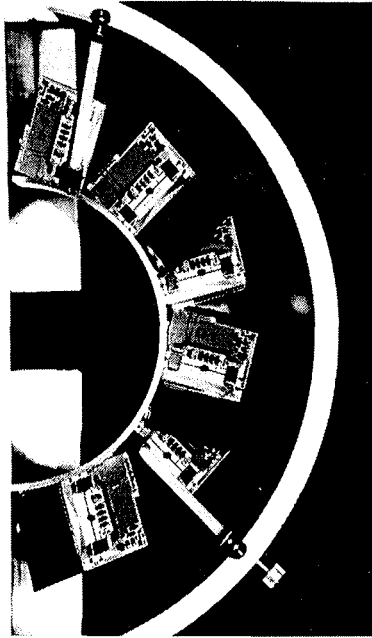
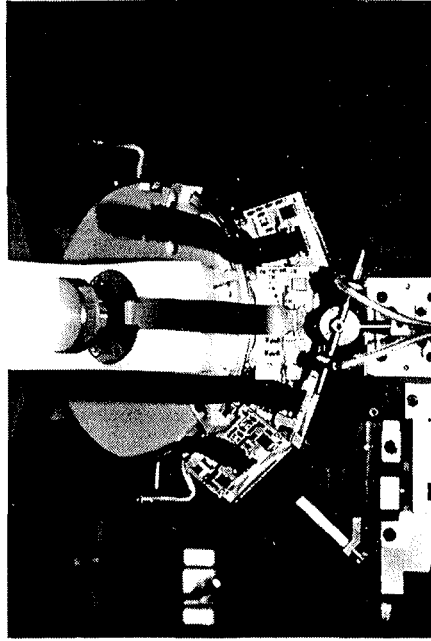
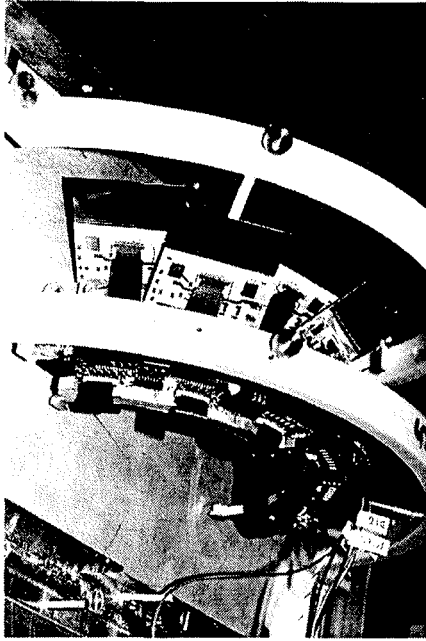


Figure 5.2: Mounting of the detector on the support crown (top row) and a VFT ministrip crown ready for installation (bottom row).

can be supplied and tested individually. The detector leakage current and noise level is monitored for periods of days under final operation conditions to ensure detector stability. Finally the position of the modules on a crown with respect to each other is measured again on the 3D survey machine. A final VFT ministrip crown is displayed in picture 5.2.

## 5.2 Test of silicon detector parameters

As the silicon plaquettes form the center piece of the ministrip detector, extensive tests were carried out to select silicon detectors for the production of the VFT ministrip detector, allowing reliable and stable operation of the detector system. The main concerns for later operation are related to detector leakage current stability since a high leakage current deteriorates the S/N performance. Furthermore, the influence of the readout and control electronics on the noise performance is analysed. The final operation voltage of the detector is given by the FOXFET punch-through voltage between bias line and strip implant plus the voltage needed to fully deplete the detector bulk. A uniform depletion and punch-through voltage is desired to allow common voltage supply to several detectors. A maximum number of defect strips under 2% is required to limit detector inefficiencies. The criteria used for the acceptance tests [46] on the finished modules are

- sum of depletion and punch-through voltage, i.e. the detector operation voltage, less than 60V. As will be shown later some detectors have a punch-through voltage higher than 15V. For the operation the sum of punch-through voltage and full depletion voltage is relevant, therefore a limit to the sum is set.
- detector leakage current in the active area less than  $3\mu\text{A}$  at 60V;
- guard ring leakage current less than  $10\mu\text{A}$  at 60V operation voltage
- the sum of drain and guard ring leakage current has to stabilize during the long time test at a value less than  $13\mu\text{A}$ , which reflects the sum of the drain and guard current in the specifications to Micron;
- a maximum of 5 defect strips per detector.

In total 130 detectors have been tested for their short and long time behaviour of the leakage current, the full depletion voltage, the punch through voltage of the FOXFET biasing structure and pinholes through the coupling oxide between implant and metal readout line.

### 5.2.1 Detector leakage current

Two sources of leakage current are measured: the guard ring current and the drain current on the biasline.

Firstly the current on the guard ring is measured by contacting the widest of the three guard rings. The bias line, or drain of the FOXFET structure, is kept on the same potential as the guard ring, i.e. on ground, but only the current of the guard ring is measured. The voltage on the backplane is automatically ramped up in steps of 2V to

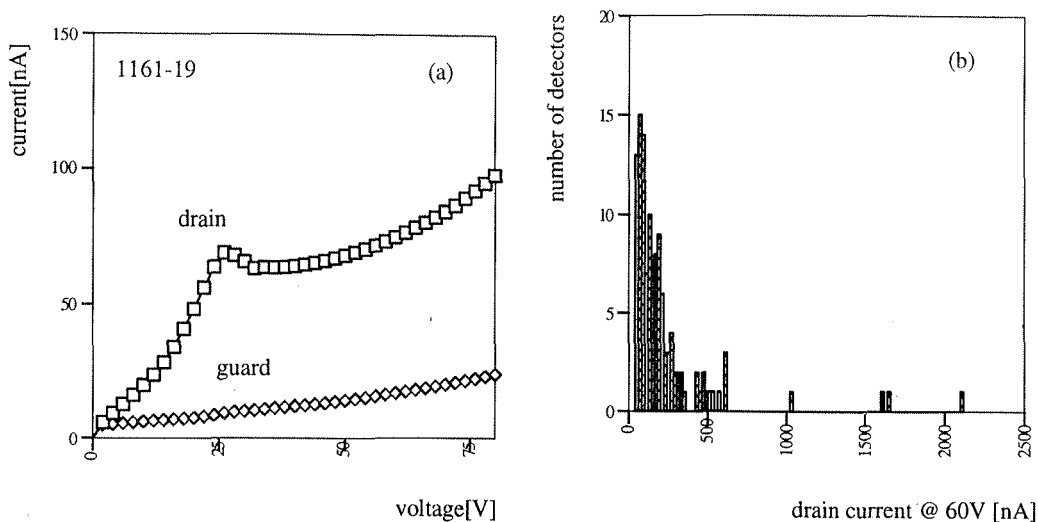


Figure 5.3: Leakage current in the detector active area and on the guard ring (left). The plot on the right shows the drain leakage current at 60V bias voltage for 110 detectors.

60V with a delay of 10 seconds between the measurements. The current-voltage (IV) measurement was carried out with a Keithley Source-Measure Unit K237. The guard ring absorbs the leakage current mainly generated by impurities and defects along the detector edges which would otherwise be collected on the edge strips of the detector. Depending on the detector processing and handling it can vary from nA to several tens of  $\mu\text{A}$ . Apart from this shielding of the active detector area it has no influence on the detector performance.

Secondly the leakage current of the detector active area is measured on the bias line to the strip implants in the same manner with keeping the guard ring on ground. Both bulk and surface currents contribute to the total current measured. This current should be as low as possible as it represents a source of parallel noise for the amplifier. Figure 5.3 illustrates the leakage currents measured in the detector active area and on the guard ring. The total measurement time is approximately 10 minutes. The plot on the right shows the drain leakage current at 60V operation voltage for 110 detectors. The average drain leakage current for  $27\text{cm}^2$  active area is on average 150nA. In a second test the leakage current stability is tested by monitoring the sum of drain and guard ring current at 60V operation voltage for several hours. In general a good stability with time is observed, which is illustrated by the left graph of figure 5.4.

On 30 detectors an increase of leakage current with time is observed until a plateau at a few  $\mu\text{A}$  is reached. It is found that for all those detectors only the guard ring current contributes to the current increase while the drain current remains constant. Detector reaching the plateau below the specification limits are accepted for detector production. The leakage current on single strips is typically 300pA.

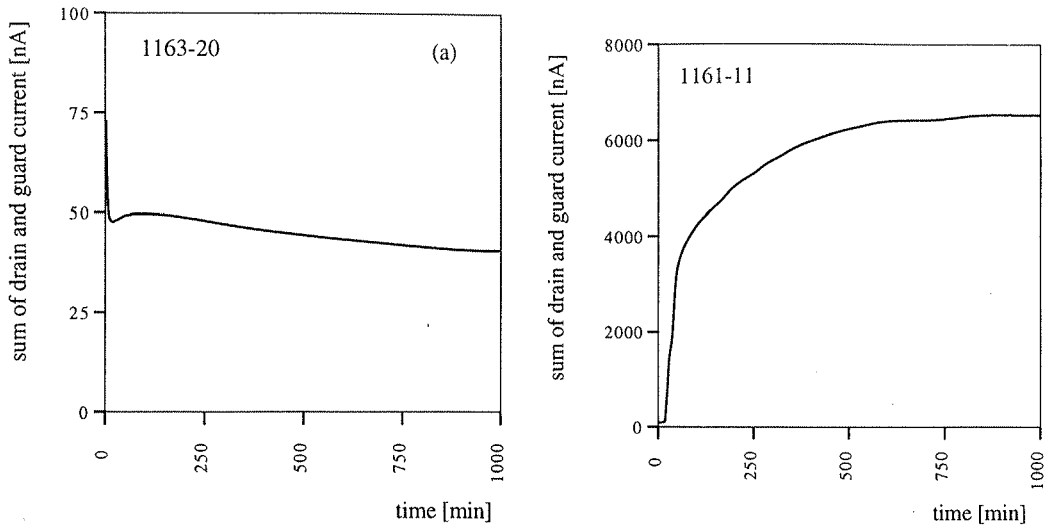


Figure 5.4: Sum of drain and guard ring leakage current for two detectors.

### 5.2.2 FOXFET dynamical resistance

To bias the strips on an AC coupled silicon detector the strips have to be connected to a common bias line via a large resistor. The value of this resistor has to be high as it acts as a parallel resistor on the amplifier input, and thus influences the noise. In our case this resistor is formed by the channel resistance of a pnp field effect transistor, where the two  $p^+$  regions correspond to the strip and biasline implant. The strip acts as the source of the FET, the biasline as its drain. This biasing scheme has been successfully used by several groups [47] [48] [49] [50]. For its realization, no additional steps are needed in the device fabrication, which for example are necessary for the production of discrete polysilicon resistors. The space used is small, thus a high active detector area is maintained. The channel length is  $6\mu\text{m}$  and has a width of  $10\mu\text{m}$  for our detector. The channel is covered by  $1\mu\text{m}$  silicon dioxide used to separate the gate contact from the channel.

The biasing is achieved by the so-called punch-through effect between strip and biasline: When a voltage is applied between the  $p^+$  regions, one of the two pn junctions becomes forward biased and the other one reverse biased. The voltage difference is mainly taken up by the reverse biased junction around which a depletion region begins to form. If the voltage is increased, this depletion region will grow and reach the forward biased junction at the strip when the so-called “punch-through voltage” is exceeded. The voltage offset between biasline and source will logarithmically depend on the current between strip and biasline, therefore the resistance between strip and bias line is said to be dynamical. The resistance will decrease when the current between strip and bias line, i.e. the strip leakage current during normal detector operation, is increased. The value of the punch-through voltage is mainly determined by the existence of fixed positive space charge in the oxide and on the Si-SiO<sub>2</sub> interface [51], which leads to an electron accumulation layer below the oxide and increases the punch-through voltage. By applying a negative voltage to the gate the pnp FET, the accumulation layer and therefore the punch-through voltage can be influenced.

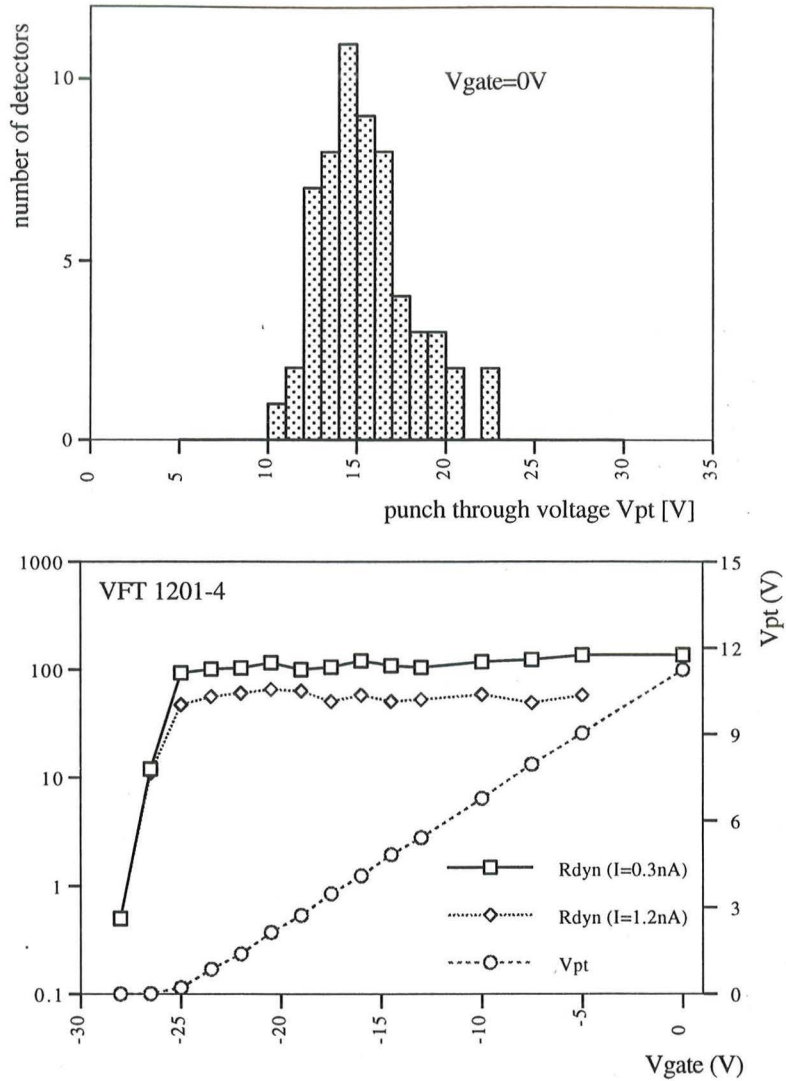


Figure 5.5: Punch-through voltage  $V_{pt}$  at  $V_{gate} = 0$  for 60 detectors (top). The lower plot shows the dynamical resistance and punch-through voltage at different gate voltages.

To operate the detector, the voltage  $V_{op}$  is applied between backplane and biasline. After the punch-through voltage  $V_{pt}$  is reached the voltage on the strip implant will be  $V_{op} - V_{pt}$ .  $V_{op} - V_{pt}$  is used to create the depletion between implant and backplane. To fully deplete the detector volume an operation voltage has to be applied that exceeds the sum of full depletion voltage  $V_{fd}$  between backplane and strip and punch through voltage  $V_{pt}$  between strip and bias line. For this reason both characteristic voltages  $V_{fd}$  and  $V_{pt}$  have to be tested on each detector.

The upper plot in figure 5.5 shows the measured punch-through voltage for a subset of the detectors. For the measurement of the punch-through voltage an operation voltage of 60V is applied to the backplane while the biasline and gate are grounded. The potential difference between the strip implant and the biasline is measured on a sample of strips to give the punch-through voltage at  $V_{gate} = 0$ . No external current is imposed so that  $V_{pt}$

is measured at a drain-source current  $I_{ds}$  equal to the strip leakage current.

The bottom graph in figure 5.5 shows the dynamical resistance as a function of the applied gate voltage. It is derived from a measurement of the voltage difference drain-source at varying drain-source currents at a given  $V_{gate}$ . The dynamical resistance is calculated from the slope of the VI curve at two different values of  $I_{ds} = 0.3, 1.2\text{nA}$ . At the average strip leakage current  $I_{ds} = 0.3$  a resistance of  $130\text{M}\Omega$  is measured which remains constant until  $V_{gate} = -25\text{V}$ . At  $V_{gate} = -25\text{V}$  the FOXFET is switched on and the resistance drops sharply. At  $I_{ds} = 1.2\text{nA}$  the resistance decreases to  $60\text{M}\Omega$ . The same plot gives the punch-through voltage at different gate voltages. The punch-through voltage is measured at  $I_{ds} = 0.3\text{nA}$ . The gate voltage can be used to adjust the voltage difference between biasline and strip without altering the resistance over a wide range.

### 5.2.3 Backplane capacitance and depletion voltage

The full depletion voltage  $V_{fd}$  between strip implant and backplane is defined as the voltage necessary to extend the depletion region from strip implant to the backplane contact. Any voltage below will result in a narrower depletion region and hence lead to signal loss. It can be determined by measuring the capacitance of the strip side to the backplane, which is proportional to the width of the depletion region and thus shows a  $\frac{1}{\sqrt{V}}$  behaviour (compare equation 3.16).

$V_{fd}$  depends on the resistivity of the silicon wafer and is measured by Micron on a DC coupled diode placed next to the detector on the wafer. Contrary to the MICRON measurement our measurement is carried out on the detector itself. A positive voltage is applied between the biasline (ground) and the backplane to deplete the detector. The backplane capacitance is measured with a Hewlett Packard LCR Meter HP4285A, which sources  $100\text{kHz}$  signal with  $0.1\text{V}$  amplitude on the backplane and measures it on the bias line. The device under test is assumed to be a capacitor in parallel to a resistor.

An intrinsic problem in measuring the total backplane capacitance of a FOXFET biased detector is illustrated in figure 5.6b. For this measurement the detector is operated at normal conditions, i.e.  $V_{gate} = 0$ . The measured capacitance at  $60\text{V}$  corresponds only to the capacitance of the biasline to the backplane, as the rest of the detector is shielded from the measuring signal by the high FOXFET resistance. Once the FOXFET is brought to its conducting state by applying  $-30\text{V}$  to the gate contact, compare with figure 5.5, all strips are connected to the biasline. Under this condition the backplane capacitance of the entire bulk volume is measured as illustrated in plot (a). The measured capacitances of  $900\text{pF}$  corresponds nicely to the geometrically expected capacitance

$$C_b = \epsilon_0 \epsilon_{Si} \frac{A}{T} = 931\text{pF} \quad (5.1)$$

where  $A$  denotes the detector area,  $T$  the thickness,  $\epsilon_0$  the permittivity of vacuum and  $\epsilon_{Si}$  the dielectrical constant of silicon. The expected  $\frac{1}{\sqrt{V}}$  behaviour is reproduced by the measurement as illustrated in plot (c).  $V_{fd}$  is obtained from the intersection point of line fits to the linear and constant part of the graph. Plot (d) shows the distribution of  $V_{fd}$  (open histogram) and  $V_{fd} + V_{pt}$  (hatched histogram). The detectors exceeding the specification limits were not used for production and replaced by new detectors by MICRON.

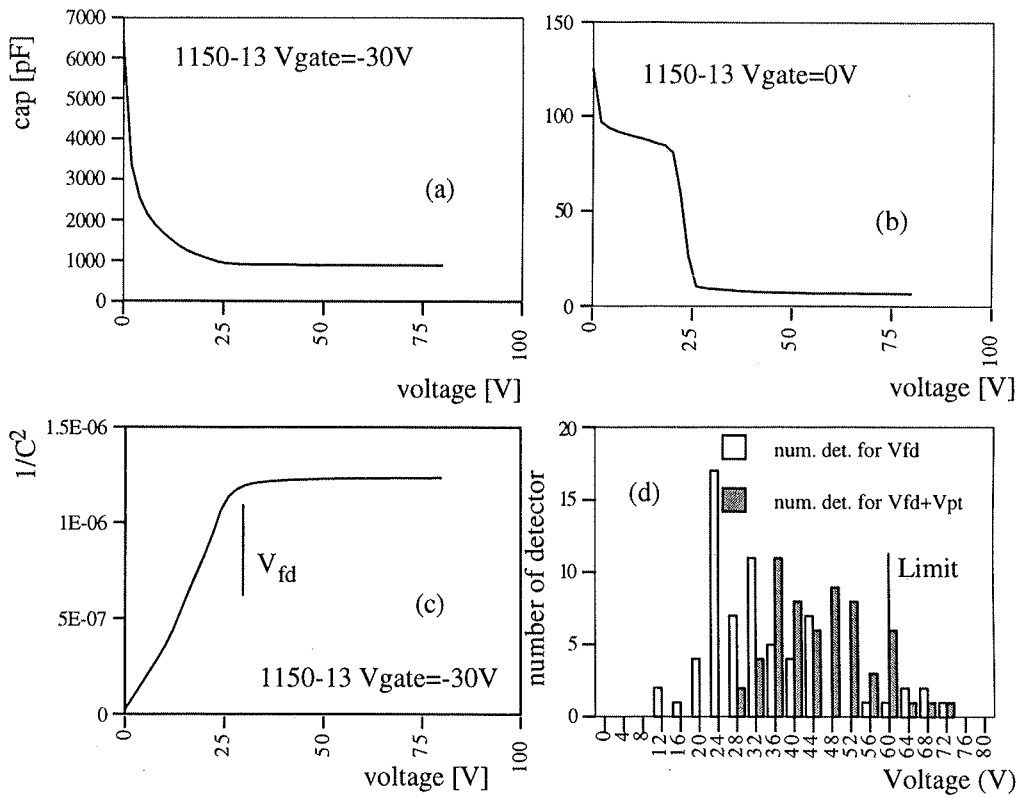


Figure 5.6: Measured capacitance between biasline and backplane at  $V_{gate} = -30, 0V$  and distribution of  $V_{fd}$  (open histogram) and  $V_{fd} + V_{pt}$  (hatched histogram) [52] .



## 5.2.4 Coupling capacitance and pinholes in the coupling oxide

The value of the coupling capacitor between the readout strip implant and the aluminum readout line, realized by a 200nm thick layer of  $\text{SiO}_2$ , can influence the performance of the detector in two ways. Firstly its value has to be large compared to the backplane and interstrip capacitance to guarantee efficient charge transfer to the amplifier. Secondly it separates the amplifier input from the strip implant. In case of a DC connection between implant and amplifier input through a pinhole in the oxide layer, the detector leakage current will run directly into the amplifier and may saturate it.

The coupling capacitor is tested by measuring the capacitance between the probe pad on the implant and the metal readout line. A constant coupling capacitance of 77pF/cm is measured for each readout strip<sup>1</sup>. This value is sufficiently high to allow efficient charge collection. Furthermore every readout strip is tested for pinholes through the oxide by MICRON before the detector is delivered. A maximum number of 5 strips with pinholes is allowed on the individual detector. The measurement is repeated after delivery on a sample of detectors for each delivery batch and agrees with the MICRON measurement. On average the detectors have one strip with pinholes.

## 5.3 Final acceptance tests on the VFT ministrip modules

Before the finished modules can be mounted to the final support, each of them has to undergo extensive tests at CERN. The aims of the tests are to

1. detect any electronic problem on the detector,
2. calibrate the signal gain for each channel,
3. record the number of dead, noisy and saturated channels,
4. verify the S/N performance,
5. optimize operation parameters like backplane and gate voltage.

To test these parameters a setup was constructed which allows to test each module with calibration signals and with a Sr-source.

In the calibration setup, illustrated in figure 5.7, a voltage step  $V_0$  is generated externally and coupled on the backplane voltage supply line of the module. The value of  $V_0$  can be adjusted by a potentiometer, the timing is chosen such that the step falls between the S1 and S2 signals of the data capture cycle shown in figure 3.5. The detector is under normal operation condition, i.e. biased, therefore the well-known backplane capacitance of each strip acts as a calibration capacitor on the amplifier input. The input charge corresponds to  $C_b V_0$  and during our tests is approximately the charge deposited by a minimum ionizing particle.

In the source setup the VFT module is mounted below a  $^{90}\text{Sr}$ -source. The readout is triggered by a scintillator having the same active area as the detector. The scintillator is

---

<sup>1</sup>measured with Keithley Quasi Static CV meter K595

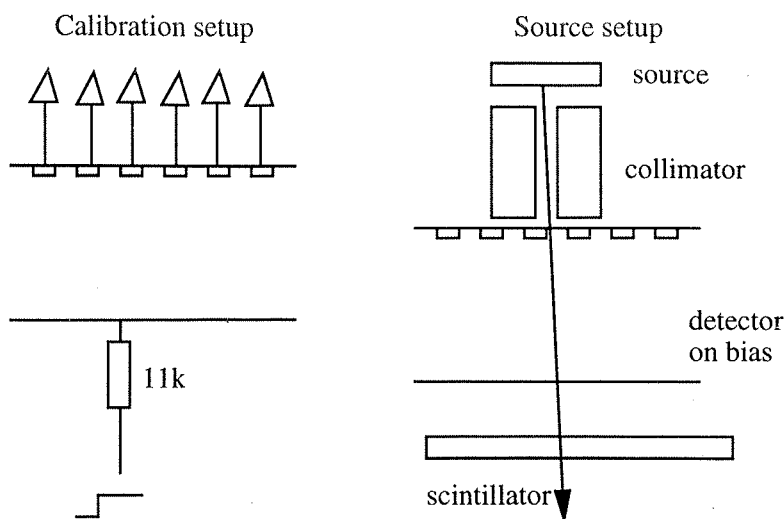


Figure 5.7: Schematic illustration of the calibration and source setup.

read out on two sides, the coincidence of the two scintillator signals triggers the module readout. The double-sided readout of the scintillator is necessary to reduce the noise coming from the photo-multiplier. The recorded signal in the VFT module is approximately 10% higher than the one of a minimum ionizing particle. The track angle is limited to about  $10^\circ$  due to the geometry of the setup.

The setup (figure 5.8) is constructed only with final components of the VFT detector system in order to obtain the best possible comparability to its later performance in DELPHI. This applies especially to the components in the analog signal transfer to the ADC. Indeed the latter determines the final signal gain and can influence the noise performance. All detector tests are carried out with original VFT repeater cards, which amplify the analog signals coming from the detector and multiplex the control signals to the individual detectors. The timing for the signals controlling the data capture and readout cycle is chosen to match the final timing as close as possible. The digitization of the analog data is done by one SIROCCO fastbus module. Additionally, only final power supplies are used for the supply of backplane voltages, and the supply voltage of the MX6 chips and repeater cards.

As this setup matches one full quarter of the VFT ministrip detector it also provides a good opportunity to test and optimize the data acquisition software. This specially applies to the program running on the SIROCCO digital signal processor that is used to calculate the strip signals from the raw data and detect signal clusters for data compression reasons.

### 5.3.1 Results of the signal calibration

The calibration setup is used to determine the signal gain for each use in the DELPHI offline analysis of the VFT detector.

The signal gain measured with this calibration is the product of the gain of each MX6 amplifier channel, the gain of the voltage amplifier on the repeater card and the gain of the input amplifier on the SIROCCO. While the first mentioned can vary from one readout

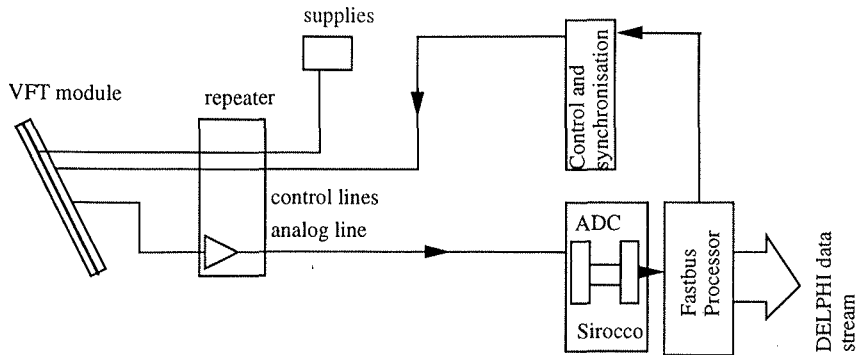


Figure 5.8: Setup used for the detector acceptance tests. This figure illustrates the data acquisition for one quarter of the VFT ministrip detector system.

strip to another, the latter ones are constant for three adjacent modules on a crown since they are multiplexed together and digitized by the same SIROCCO channel.

Strips are regarded as “dead” if their signal in response to the calibration pulse is less than 50% of the average signal of all channels on the chip. Channels with a r.m.s. noise higher than 5 times the average r.m.s. noise of all channels on one chip are regarded “noisy”. Channels with a pedestal voltage saturating the SIROCCO ADC are called “saturated” channels. The sum of all three types of substandard channels on each detector side must not exceed 5 in order to be accepted for final use in the VFT detector.

Figure 5.9 illustrates the typical response of one VFT module to the calibration pulse. One calibration run consists of 100 events without a calibration pulse on the detector and 100 additional events with the calibration pulse on. The pedestal and noise of each channel are obtained from the mean and r.m.s. of the ADC count spectrum recorded without calibration pulse. The channel signal in response to the calibration signal is given by the difference of mean ADC value with and without calibration pulse. The two plots on the left hand side show the pedestal for all channels on TOP and BOTTOM detector. The pedestal variation between the channels is small compared to the range of the 10 bit ADC.

The two central plots indicate the signal response to the calibration pulse. The dead channels can easily be identified as no calibration signal is recorded. The main causes for dead channels are either bad amplifier channels on the MX6 chip or interrupts on the fan-in lines. As the charge of these channels cannot be transferred to the amplifier, it is capacitively coupled to the adjacent channels leading to an increased signal on them.

The backplane capacitance of the edge strips on the right side of each plaquette is smaller than the other strips as they are shorter, which results in a smaller signal. On the contrary, the first strip in the readout covers a larger active area than the other strips which explains the higher signal measured on it. Furthermore a gain difference between the two chips of each plaquette is observed. The module additionally exhibits a clear modulation of the channel gain every 16 channels. This is due to the internal structure of the MX6 chip [53].

The two plots on the right hand side in figure 5.9 give the r.m.s. noise for each channel

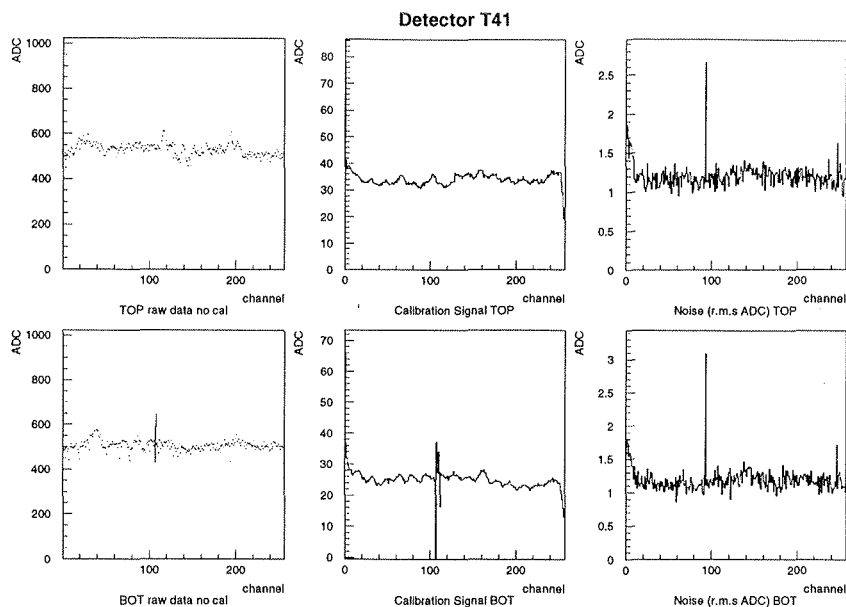


Figure 5.9: Pedestal, signal in response to the calibration pulse and r.m.s. noise of all channel of a typical VFT ministrip module.

on the TOP and BOTTOM side of the module.

The distribution of substandard channels on TOP and BOTTOM detectors for 31 modules is given in figure 5.10. On average each module side has two bad channels which are of limited use for the position reconstruction. The number of dead and noisy channels is about equal, while nearly no channels are saturated.

### 5.3.2 Results of the $^{90}\text{Sr}$ source test

After the proper functioning of each module has been tested with calibration pulses it is tested with a  $^{90}\text{Sr}$  source to determine its S/N performance. This test also provides a cross-check of the noise measured during the calibration run. Contrary to the calibration test the common mode shift it corrected during the source test.

Figure 5.11 illustrates the response of a typical detector in the source test. The two plots on the left show the S/N distribution for the TOP and the BOTTOM detector. The tail on the lower end of the distribution is due to electrons passing the module at the very end of the S1-S2 measurement window (refer to figure 3.5). The S2 switch is closed before the maximum voltage is reached on the C2 sample capacitance in the MX6 chip. Thus the measured detector signal is smaller. This effect is an artefact of source tests with the MX6 chip and will not be present in DELPHI. For the operation in DELPHI the time when particles cross the detector is precisely known from LEP synchronisation signals and remains constant, therefore the S1-S2 window can be adjusted properly. The measured most probable S/N is 32 on both detectors.

The right hand plot shows the hit position on the TOP detector versus the hit position on the BOTTOM detector. As the source is collimated, only a part of the detector is

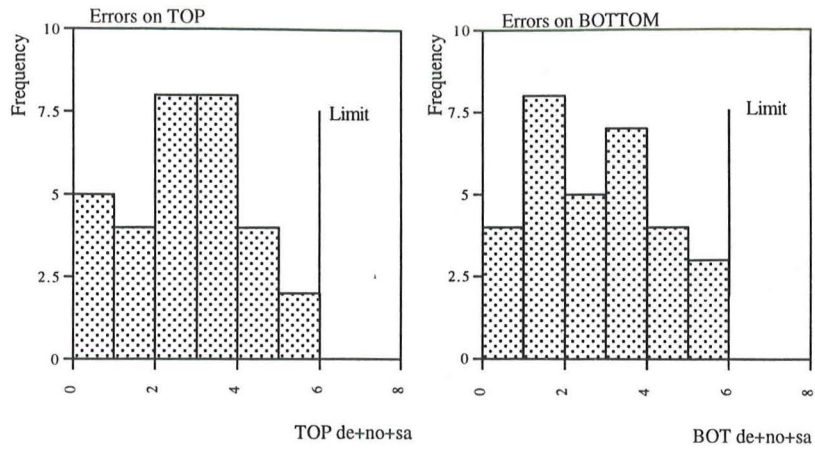


Figure 5.10: Distribution of substandard channels on accepted VFT ministrip modules for TOP and BOTTOM side of the modules.

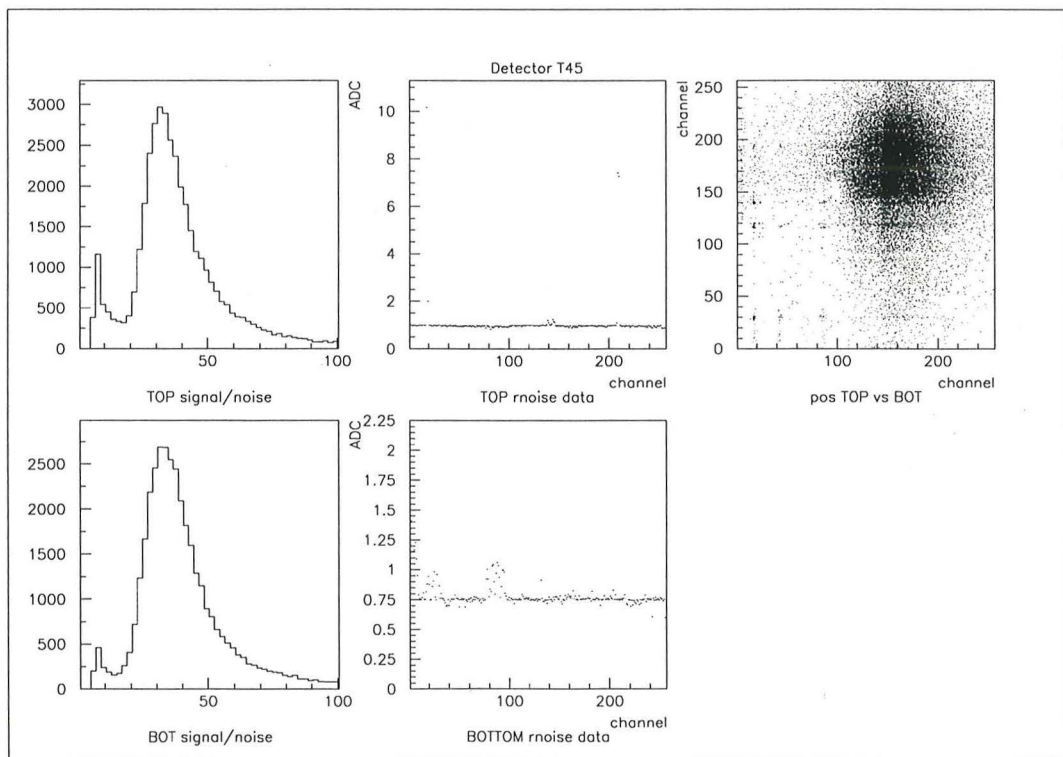


Figure 5.11: Results of a source test on a typical VFT ministrip module. The plots show the S/N distribution and r.m.s. noise for TOP and BOTTOM side of the detector. The right plot shows the measured hit position on TOP versus BOTTOM side.

exposed to it. The measured distribution is not smooth but exhibits a clear structure. This is due to the screening of the detector from the low energy electrons caused by the electronic hybrid and components on it.

The two central plots illustrate the r.m.s. noise of all channels for this module. The average r.m.s. noise is 1.1 ADC counts for this detector. Using the most probable energy loss with 26000 electrons and the measured S/N with 33, an approximate ENC noise of 780 electrons is present. The theoretical limit can be calculated by using the measured values for interstrip and backplane capacitance, capacitance of the fan-in (1.5pF), dynamical resistance of the bias resistor in parallel to the feedback resistor and measured strip leakage current. The resistor in the amplifier feedback loop is assumed to have 50M $\Omega$ . The measured backplane and interstrip capacitance of one readout line plus the capacitance of the fan-in sums to the total load capacitance of  $(0.77 + 0.69)5.2 + 1.5 = 9\text{pF}$  on the amplifier input. An average strip leakage current of 0.3nA is used for the calculation. Using equations (3.22) to (3.24) the total expected ENC noise can be calculated as

$$ENC_{cal} = \sqrt{(325 + 23 \cdot 9)^2 + 144^2 \cdot 0.3 + \frac{1024^2}{36}} = 564 \quad \text{electrons} \quad (5.2)$$

This calculation considers the input transistor of the MX6 amplifier channel only and assumes all other components in the signal transfer to the ADC to be noiseless, which is clearly not the case. The upper limit most probable  $(S/N)_{mp}$  value is calculated with the above  $ENC_{cal}$  and respecting the charge measurement efficiency of 87% for our detector to be 37. On average a  $(S/N)_{mp} = 31$  is obtained in the source test, as illustrated in figure 5.12.

## 5.4 Test beam studies with VFT ministrip modules

Before the main production of the VFT ministrip detector started the first three modules produced were tested in a testbeam run at the SPS accelerator at CERN. The aim of this study was to cross-check the layout and production techniques used. Furthermore, the operation voltages on backplane and gate contact for later use in DELPHI were optimized.

The VFT module is aligned with its strip plane perpendicular to the beam axis. The detector is exposed to a 80GeV/c pion beam. The readout and detector supply is identical to the one described above for the source tests. Figure 5.13 shows the most probable signal in dependence of the backplane voltage  $V_b$ . The value is obtained from a Landau fit to the total cluster signal distribution. During this test, the gate contact is grounded together with both the guard ring and the biasline. This is the operation mode foreseen for DELPHI. At low  $V_b$  the detectors are not fully depleted, thus the signal increases slightly with  $V_b$ . After  $V_b$  exceeds 50V the signal remains constant, as the detector is depleted. All three detectors reached the plateau before 60V.

The most probable S/N ratio for the entire cluster S/N distribution is 25 to 27 for the three modules. The difference compared to the source test may be due to additional external noise sources during the testbeam, as well as higher energy deposition by the source than by the minimum ionising particle. The cluster S/N distribution contains two contributions with different S/N ratios corresponding to hits on the intermediate strip

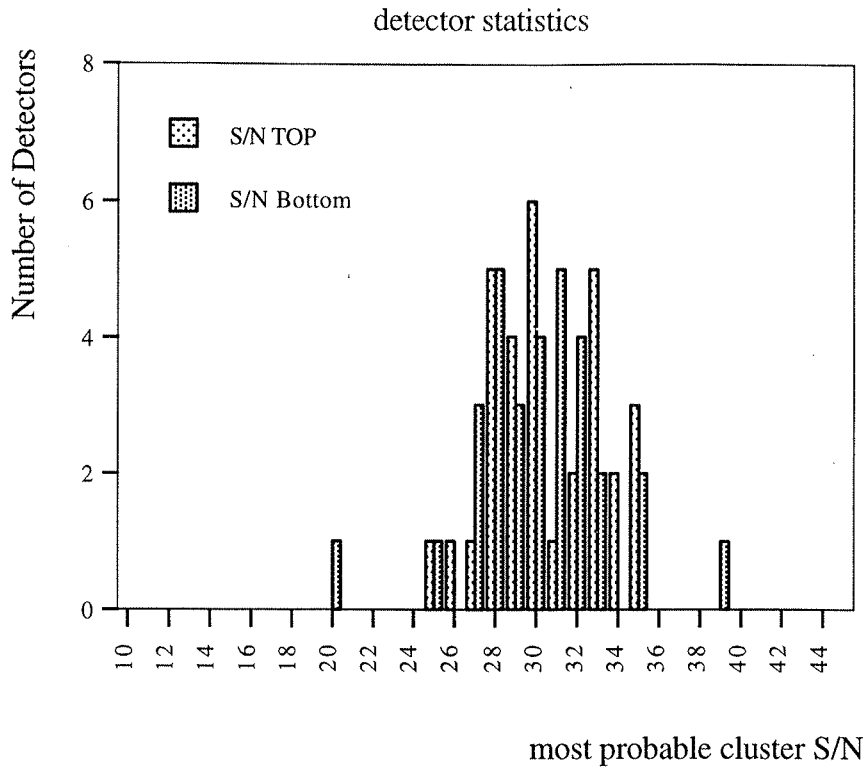


Figure 5.12: Distribution of measured  $(S/N)_{mp}$  and average r.m.s. detector noise for 30 VFT ministrip modules.

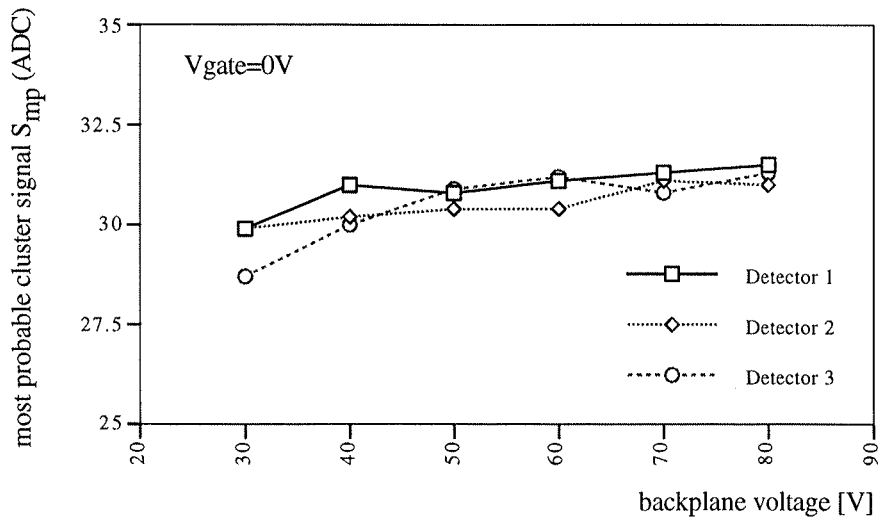


Figure 5.13: Most probable cluster signal  $S_{mp}$  versus backplane voltage. The detector is operated at  $V_{gate} = 0V$ .

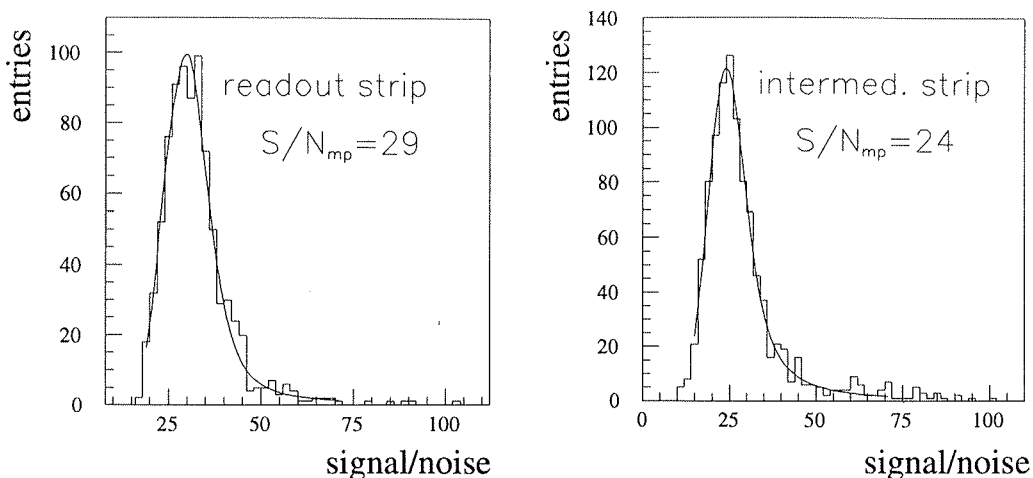


Figure 5.14: S/N distribution for hits on the readout and intermediate strip at  $V_b = 60V$  and  $V_{gate} = 0V$ .

and hits on the readout strip. On the readout strip a S/N of 29 is measured and on the intermediate strip of 24. The corresponding distributions are shown in figure 5.14. The ratio of signal intermediate strip to readout strip is perfectly consistent with the previous measurements on test detectors presented in section 3.4.

The influence of the gate voltage is twofold: It controls the dynamical resistance of the FOXFET, and thus might influence the noise and secondly it may be used to steer the voltage offset between biasline and strip implant  $V_{pt}$  as illustrated in figure 5.5.  $V_{gate}$  is varied for the following test to investigate possible changes to the S/N performance. For this test  $V_b$  is set to 60V and  $V_{gate}$  is varied from 0 to -12V. The most probable S/N for the total detector is plotted in dependence of the gate voltage in figure 5.15. No significant change to the S/N performance is observed.

The detectors are planned to be operated at a backplane voltage of 60V and a gate voltage of 0V in DELPHI.

During this testbeam a particular problem has been observed. Groups of channels on the detectors had extremely high pedestals and some channels among them eventually saturated. The channels pedestal varied over the entire range of the ADC but remained stable. The same groups of channels with high pedestal were observed on all three detectors at the same position. This problem has been traced back to the particular way the MX6 chip is operated: Before the particle passes the detector, the MX6 chip needs the RESET and S1 signals. As the control lines on the hybrid are close to the detector strip surface, the transient of the RESET and S1 signal produced a pick-up signal on the aluminium readout lines on the detector, which increased the pedestal and eventually saturated the amplifiers. This problem was solved by routing these two signals on two small kapton lines on top of the hybrid to the MX6 chip.



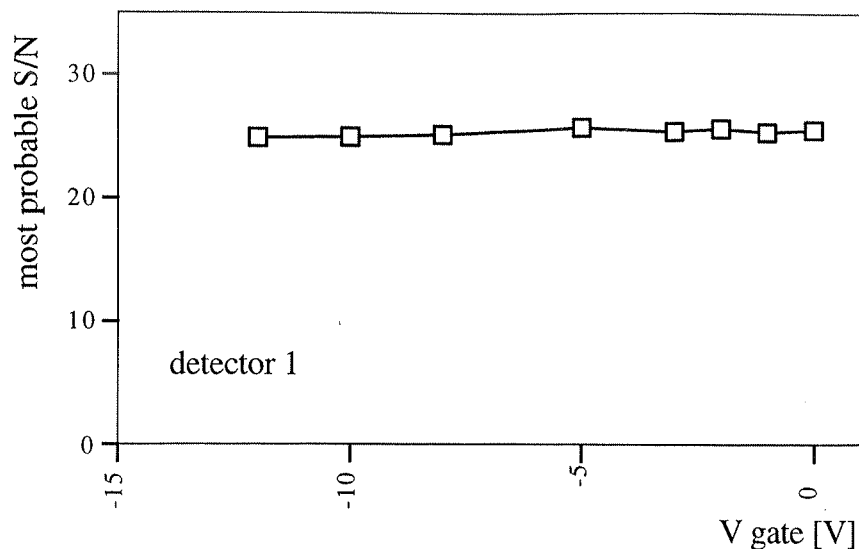


Figure 5.15: Most probable cluster S/N versus gate voltage. The detector is operated at  $V_b = 60V$ .

## 5.5 Stability test of VFT ministrip crowns

As any manipulation of the detector may cause damage to the detectors or to the electronics each VFT ministrip crown is tested after the 6 VFT modules are mounted and measured on the Poli machine. The mounted crown is supported by a frame together with the repeater card, which is connected to the 6 modules. This allows tests at any moment during the detector assembly.

The finished crown is tested by means of calibration signals supplied to the backplane of each individual module via the backplane voltage supply line. Each module has its own backplane voltage supply which allows to monitor the current absorbed by the entire module. The setup used for the tests corresponds exactly to the above described calibration setup. The tests monitor

- the time dependence of the module backplane current
- the number of dead and noisy channels with time
- the average r.m.s noise on the detector.

For the tests the crown is placed in a shielded box, which is light tight and keeps the detector at a nearly constant temperature of 22-25°C. The operation temperature in DELPHI will be around 25°C. The atmosphere in the test box is enhanced with nitrogen to keep the humidity in a range of 30-40% during the tests. The VFT modules are operated at  $V_b = 60V$  and  $V_{gate} = 0V$ .

After the modules on a crown are biased, a calibration run is carried out to obtain the noise level of the detector in the very beginning of the stability test. The test is repeated every 3-4 hours to trace any time dependence after the system stabilised. Figure 5.16 shows the measured current on the backplane supply line versus time after initial biasing.

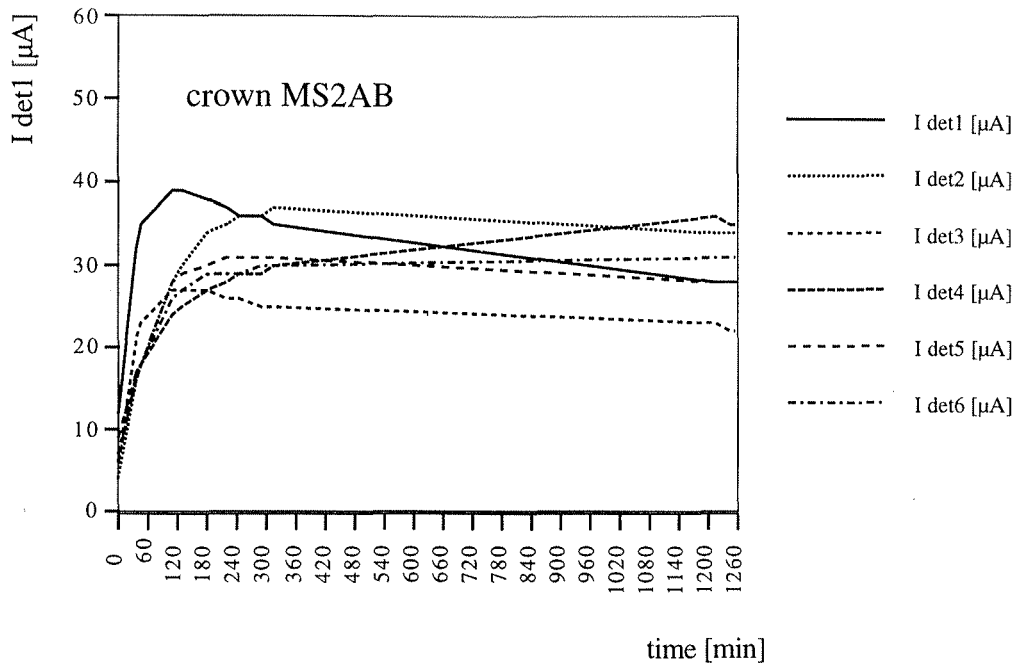


Figure 5.16: Current on the backplane voltage supply line versus time for one VFT ministrip crown.

A relaxation time of about 2 hours is observed after which the currents remain constant. The observed current on each module is higher than the drain leakage current measured on the single silicon detectors, which is primarily the only one influencing the noise. In addition also the guard ring current may also contribute significantly to the measured current. Additional current is likely to be due to surface current on the hybrid where the supply lines for detector ground and backplane are rooted to the silicon detectors. The ground line, which serves as connection to biasline and guard ring, is rooted on the hybrid close to the line supplying the backplane voltage for TOP and BOTTOM detector.

The average r.m.s. noise is measured on each detector module at the time of initial biasing and after relaxation of the system. Figure 5.17 compares the noise levels of the detectors in the beginning and at the end of the tests. The noise level remains approximately constant throughout the test. No significant noise increase is observed between initial biasing and the end of the measurements for the detectors with higher current on the backplane supply line. This suggests other current sources than the drain leakage current. The dead and noisy channels measured on the final VFT crowns correspond exactly to the substandard channel detected in the single module test.

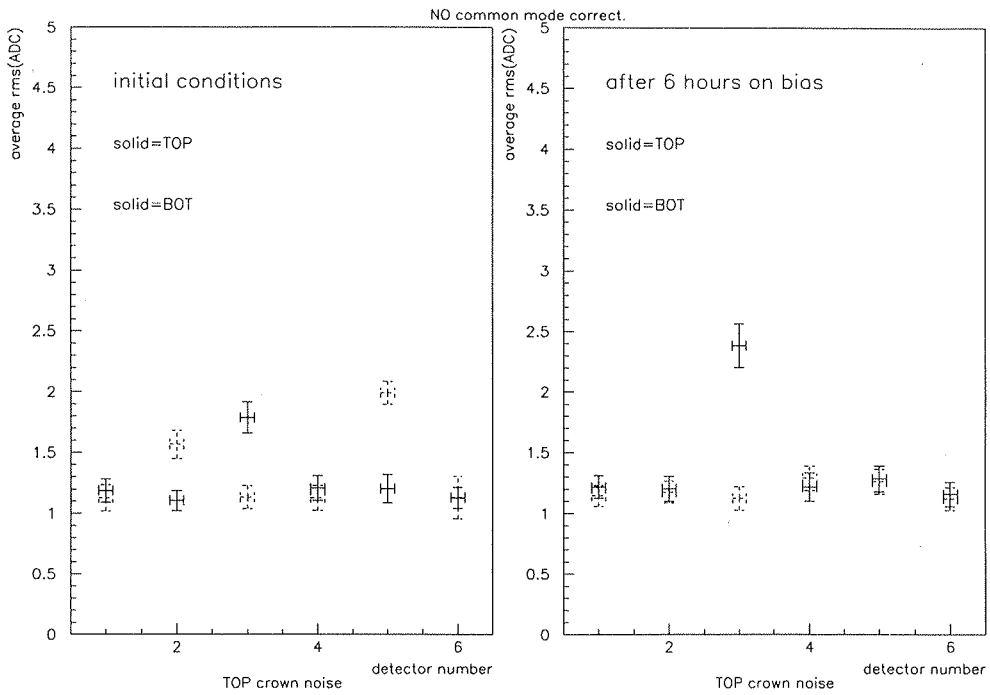


Figure 5.17: Average r.m.s. noise of 6 VFT modules on a crown after initial biasing and after relaxation of the system (typically 2-3 hours). The noise is obtained from the r.m.s. of the ADC spectrum and is hence not corrected for any contributing common mode shifts.

# Chapter 6

## Summary and Prospects

A new silicon tracking detector for the extreme forward region of the DELPHI experiment was designed, tested and constructed.

An unconventional detector design has been developed to cope with the tight space constraints and the complex environment of a tracking detector in the extreme forward region close to the interaction point. Furthermore the requirement of compatibility with the existing microvertex detector and its readout electronics severely restricted the possibilities in the design.

The VFT Ministrip detector consists of four cones of silicon strip detectors surrounding the beam pipe. The detectors are inclined by  $50^\circ$  with respect to the beam axis to maximise the angular coverage and number of measurements per track. Each detector provides a two-dimensional measurement of the particle trajectory. The very limited space in this region required the readout electronics to be mounted directly onto active detector surface. A careful design of the electronics has been worked out in order not to deteriorate the performance of the detector. Considerations about maximum angular coverage, high track reconstruction efficiency and optimal matching with the capabilities of the pattern recognition are taken into account for the design.

As Coulomb scattering in the beam tube and into detector support limits the track extrapolation accuracy moderate intrinsic spatial resolution of the detector modules is demanded. The requirement of low construction costs and low number of electronic channels motivated the choice of large pitch silicon strip detectors. Special emphasis is given to the reliability and high signal to noise performance of the detector.

The performance of the VFT ministrip detector has been studied at different track angles. The precise measurement of the signal response at different track angles allowed a deep inside view of the charge collection properties of large pitch silicon strip detectors. The signal collection could be successfully modelled. A spatial resolution of  $28\mu\text{m}$  for perpendicular tracks was measured. For perpendicular tracks the resolution is dominated by the digital response for hits in the region of the strip implant. The test results for perpendicular tracks approximate the situation present in the detector measuring the  $\phi$  coordinate of the track. Charge sharing due to the track inclination improves the resolution to  $10\mu\text{m}$  at a track inclination of  $20^\circ$ . The test results obtained for  $20^\circ$ - $30^\circ$  reflect the situation for the detector measuring the  $\theta$  coordinate of the track. In the

acceptance tests a signal to noise performance of 30 has been achieved for detectors in the final configuration. This insures high efficiency and a low number of ghost clusters. The completely assembled detector proved to be stable.

The working principle and capabilities of large pitch silicon strip detectors have been tested on a wide spectrum of different, well known and newly developed, detectors. The influence of different layout parameters on signal measurement and spatial resolution was investigated. The results obtained are summarised below:

- For perpendicular tracks the signal response is constant in the region of the implant. Thus the resolution can be approximated by the width of this region divided by  $\sqrt{12}$ . Diffusion of the deposited charge results in the charge sharing and consequently in a substantially better spatial resolution for a particle hit in the interface region in between the implants.
- With increasing number of intermediate strips the spatial resolution improves, as the influence and width of the region with constant response is reduced. A spatial resolution of  $8\mu\text{m}$  has been achieved at a readout pitch of  $200\mu\text{m}$  in a configuration with three intermediate strips.
- For hits on the intermediate strips some fraction of the deposited signal is not measured. The charge loss depends on the ratio of interstrip to backplane capacitance. If the gap between implants is reduced, the interstrip capacitance rises but the backplane capacitance remains constant. As a result the signal collection efficiency is better for detectors with a small gap between the implants. The signal loss for hits on the intermediate strip varies from 17% to 25% depending on the layout of the detector.
- The influence of a coupling metal layer on the strip side on newly developed detectors has been tested. The application of an additional metal layer on the strip side increases the interstrip capacitance and subsequently reduces the loss. With this unconventional layout of the detector, the signal loss can be limited to less than 10%. The metal layer showed no unwanted side effects concerning the spatial resolution. A signal to noise performance of 113 could be achieved on a detector with this enhanced interstrip capacitance.

For the DELPHI VFT only a moderate spatial resolution is required which allowed the use of large strip pitch detectors and subsequently reduces the number of electronics channels. Future experiments at the Large-Hadron-Collider LHC have to cover large areas with silicon strip detectors for precise track reconstruction. With the use of detectors with large strip pitch the enormous number of electronics channels may be reduced.

## Appendix - Charge Amplifier

The charge sensitive amplifier can be seen as a high gain, inverting amplifier with a capacitor in the feedback loop. To analyse a circuit with operational amplifiers some simple rules can be applied

- the inputs draw no current
- the output attempts to set itself so that the voltage difference between the two input nodes is zero
- the output is the sum of inverted and non-inverted input times the gain  $v_o = A(v_+ - v_-)$

Using these rules for a charge amplifier (figure 6.1a) the circuit equations are

$$\begin{aligned}v_o &= -Av_1 & \text{and} & & v_1 - v_o &= \frac{Q}{C_F} \\v_o &= & \frac{-Q}{C_F} & & & \end{aligned} \quad (6.1)$$

This shows that  $C_F$  has to be small to achieve high sensitivity. The amplifier gain and phase shift between input and output are not constant but depend on the frequency as illustrated in figure 6.1b schematically.  $A_0$  denotes the amplifier d.c. gain and  $\omega_h$  the unity gain frequency.

Expressing  $v_1$  in terms of feedback capacitor and amplifier gain  $A = A(\omega)$  in the frequency domain indicates that the charge amplifier appears to the current signal like a resistor in series with a capacitor.

$$V_1(\omega) = \frac{i(\omega)}{j\omega C_f(A(\omega) + 1)} \quad (6.2)$$

The resistor comes from the frequency dependent part of the gain proportional to  $\omega_h/\omega$  and the capacitor from the frequency independent part. Figure 6.1c shows the equivalent circuit where  $C_d$  stands for the detector capacitance and  $R$  and  $C$  for the resistor and capacitor as they appear to the detector. If  $(A_0 + 1)C_F$  is much larger than the signal is mostly transferred to the amplifier feedback capacitance. The rise time of the output signal depends upon the time constant given by  $C_d/R$  and thus on the ratio of  $C_d/C_F$  and inversely on the unity gain frequency.

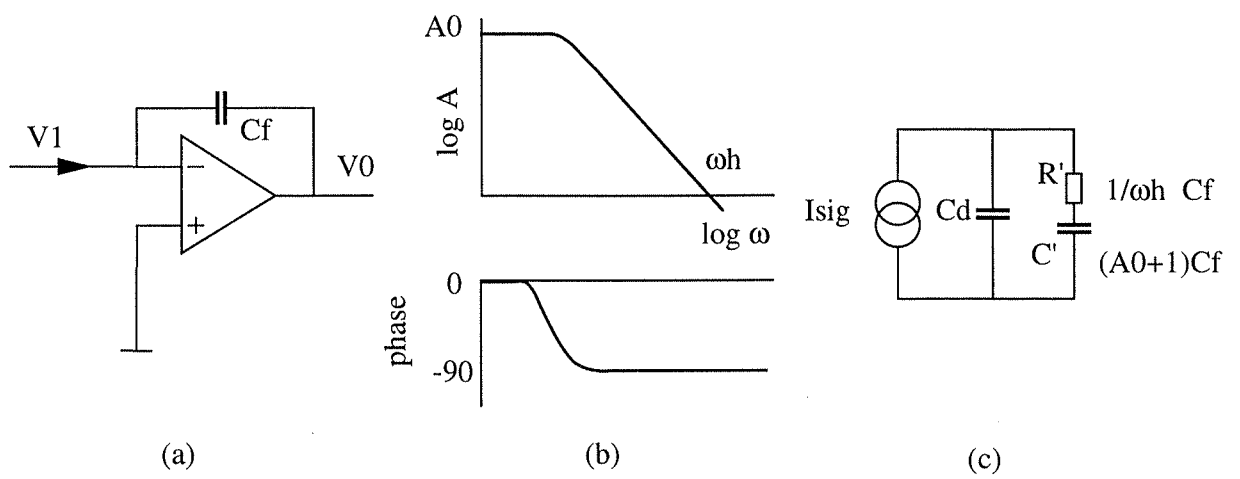


Figure 6.1: Charge sensitive amplifier (a) and gain-frequency dependence (b) Resistance and capacitance as seen by the detector signal (c).

# Bibliography

- [1] LEP collaborations ALEPH, DELPHI, L3, OPAL and LEP electroweak working group, CERN-PPE/95-172
- [2] D. Treille, CERN-PPE/93
- [3] P.J. Bryant, K. Johnsen, Circular Accelerators and Storage Rings, Cambridge University Press, 1993
- [4] DELPHI collaboration, Aarnio et al, Nucl. Instr. and Meths. A 303(1991)233-276
- [5] DELPHI collaboration, Performance of the DELPHI detector, DELPHI 95-112 PHYS 547, submitted to Nucl. Instr. and Meths.
- [6] CERN/LEPS/92-13/P2 Add2
- [7] Proposal for the DELPHI Very Forward Tracker, DELPHI 93-52 GEN 146
- [8] D. Liko, Measurement of the average lifetime of B hadrons, PhD thesis, Technische Universitat Wien, 1994
- [9] V. Chabaud et al., CERN-PPE/95-86, submitted to Nucl. Instr. and Meths. A
- [10] J.C. Stanton, IEEE Trans. Nucl. Sci. Vol. 36, No. 1
- [11] P. Collins, Proc. of the 4<sup>th</sup> Int. Workshop on Vertex Detectors, Ein Gedi, Israel, June 11-16,1995
- [12] P. Collins, Proc. of the 2<sup>nd</sup> Int. Symposium on Developments and Application of Semiconductor Tracking Detectors, Hiroshima, Japan, Oct. 10-13, 1995
- [13] V.Cindro, Y.Dufour,M.Krammer,C.Mariotti,K.Mönig,H.Pernegger,M.Pernicka, Nucl. Phys. B (Proc. Suppl.)44 (1995)292-295
- [14] A.Andreazza et al., Nucl. Instr. and Meths. A 367(1995)198-201
- [15] W.Dabrowski,P.Grybos,M.Krammer,H.Pernegger,D.Rakoczy, Nucl. Instr. and Meths. A 349(1994)424-430
- [16] DELPHI 94-44 Track78
- [17] C. Bosio et al., Nucl. Instr. and Meths. A 360(1995)71-74



- [18] J.E. Bateman, Nucl. Instr. and Meths. 17(1996)256-260
- [19] E.H.M. Heijne et al., Nucl. Instr. and Meths. 178(1980)331-343
- [20] G. Bellini et al., Nucl. Instr. and Meths. 196(1982)351-360
- [21] A. Holmes-Siedle et al., CERN-PPE/93-137
- [22] M.Caccia et al., Nucl. Instr. and Meths. A260(1987)124-131
- [23] P. Collins. DELPHI technical note 95-173 MVX 8
- [24] J.Kemmer, G.Lutz, Nucl. Instr. and Meths. A253(1987)365-377
- [25] P. Allport et al., Nucl. Instr. and Meths. A310(1991)155-159
- [26] O. Toker et al., Nucl. Instr. and Meths. A340(1994)572-579
- [27] E. Nygard et al., Nucl. Instr. and Meths. A301(1991)506-516
- [28] N. Bingefors, M. Burns, SIROCCO-IV Hardare and Software manual, CERN 1986
- [29] P. Allport, private communication
- [30] S. Roe, P. Weilhammer; ATLAS internal note INDET-NO-041
- [31] R. Turchetta, Nucl. Instr. and Meths. A335(1993)44-58
- [32] The CMS collaboration, CMS technical proposal, CERN/LHCC 94-38 p. 24ff
- [33] The ATLAS collaboration, ATLAS technical proposal, CERN/LHCC 94-43 p. 68
- [34] M. Krammer, D. Rakoczy, HEPHY Vienna, private communication
- [35] The telescope is the property of LEPSI, Strasbourg
- [36] Ch. Carli et al., Nucl. Instr. and Meths. A283(1989)723-729
- [37] W.C. Sailor et al., Nucl. Instr. and Meths. A303(1991)283-297
- [38] S. Gadomski et al., Nucl. Instr. and Meths. A326(1993)239-242
- [39] W. Dabrowski, P. Grybos, M. Idzik, Nucl. Instr. and Meths. A356(1995)241-254
- [40] J.B.A. England et al., Nucl. Instr. and Meths. A185(1981)43-47
- [41] U. Körtz et al., Nucl. Instr. and Meths. A235(1985)481-487
- [42] G. Hall et al., Nucl. Instr. and Meths. A326(1993)228-233
- [43] E. Belau et al., Nucl. Instr. and Meths. A214(1983)253-260
- [44] M. Caccia, A. Zalewska, DELPHI internal note DELPHI 91-80 MVX02

- [45] V. Cindro, D. Zontar, private communication
- [46] D. Rakoczy, Diplomarbeit, Universitat Wien, 1996
- [47] P.P. Allport et al., Nucl. Instr. and Meths. A 310(1991)155-159
- [48] P.P. Allport et al., Nucl. Instr. and Meths. A 348(1994)416-420
- [49] J.E. Duboscq, Nucl. Instr. and Meths. A 348(1994)421-423
- [50] M. Laakso et al., Nucl. Instr. and Meths. A 326(1993)214-221
- [51] S.M. Sze, Physics of Semiconductor Devices, edition John Wiley Inc., 1981
- [52] M. Krammer, D. Rakoczy, HEPHY Vienna, private communication
- [53] Phil Allport, University of Liverpool, UK, private communication

# Lebenslauf

**Dipl. Ing. Heinz Pernegger**

Geb. 7. Okt. 1966

Familienstand: ledig

Staatsbürgerschaft: Österr.

## Ausbildung

1977-1985 Bundesrealgymnasium Wien 5, naturwissenschaftlicher Zweig;  
Juni 1985 Matura

1985-1992 Technische Universität Wien, Studienrichtung Techn. Physik;  
Diplomarbeit: "Systematische Untersuchungen zur Funktionsweise einer Matrix aus Driftzellen"

Juni 1992 Sponson "Diplom Ingenieur der technischen Physik"

1993-  
Feb. 1996 Dissertation: "The Silicon Ministrip Detector of the DELPHI Very Forward Tracker"

## Aktivitäten

Aug. 1992-  
Sep. 1992 **Atominsttitut d. österr. Universitäten, Wien**

- Entwicklung und Aufbau für eines Neutron Flugzeit Meßstands bei der ORELA facility Oak Ridge National Lab., Tennessee, USA

seit Okt. 1992

Angestellter des **Institut für Hochenergiephysik** der Österr. Akademie der Wissenschaften mit Dienstort **CERN** (European Laboratory for Particle Physics), Geneva, Schweiz

- Mitarbeit beim Design, Test und der Produktion eines Siliziumstreifendetektors für den *DELPHI Very Forward Tracker* (Design Studien für den VFT Ministrip Detektor  
Test and Meßdaten Analyse des VFT Streifendetektors;  
Selektionstests und Qualitätskontrolle während der Produktion;  
Koordination der Tests und Montage am CERN )
- Entwicklung von strahlungsfesten Silizium Detektoren im Rahmen des *CERN Research & Development project RD20* (bis 12/95) (Vergleichende Studie über die Eigenschaften von Siliziumstreifendetektoren mit großem Streifenabstand)
- Entwicklung eines Diamant Spurdetektors für LHC (Large Hadron Collider) im Rahmen des *CERN Research & Development project RD42* (Studien über die Strahlungsfestigkeit von Diamant für eine mögliche Verwendung als Teilchendetektor;  
Untersuchung von Diamant Spurdetektoren im Teststrahl)